MEASUREMENT AND CFD MODELLING OF DIESEL ENGINE SPRAY DYNAMICS

By

Mohammadmahdi Ghiji

M.Sc. (Mechanical Engineering), B.Sc. (Mechanical Engineering)

National Centre for Maritime Engineering and Hydrodynamics

Australian Maritime College

Submitted in fulfilment of the requirements for the degree of

Doctor of Philosophy

University of Tasmania

November 2016

[Page intentionally left blank]

DECLARATIONS

Declaration of Originality and Authority of Access

This thesis contains no material which has been accepted for a degree or diploma by the University or any other institution, except by way of background information and duly acknowledged in the thesis, and to the best of my knowledge and belief no material previously published or written by another person except where due acknowledgement is made in the text of the thesis, nor does the thesis contain any material that infringes copyright.

This thesis may be made available for loan and limited copying and communication in accordance with the *Copyright Act 1968*.

Signed:
Mohammadmahdi Ghiji

Date: 3/11/2016

[Page intentionally left blank]

Statement of Published Work Contained in Thesis

The publishers of the papers comprising Chapters 2 to 4 hold the copyright for that content, and access to the material should be sought from the respective journals.

Statement of Co-Authorship

Chapters 2, 3 and 4 have been prepared as scientific manuscripts (papers), as identified on the title page for each chapter. In all cases, conceptualisation, research program design, numerical analysis, experimental design, physical testing, interpretation and manuscript preparation were the primary responsibility of the candidate. Accordingly he was first-named author on all papers. However, they were carried out in collaboration with supervisors as co-authors, as outlined below.

The following people and institutions contributed to the publication of work undertaken as part of this thesis:

- Mohammadmahdi Ghiji, University of Tasmania (**PhD Candidate**)
- Dr Laurie Goldsworthy, University of Tasmania (**Author 1**)
- Associate Prof Paul. A Brandner, University of Tasmania (**Author 2**)
- Dr Vikram Garaniya, University of Tasmania (**Author 3**)
- Dr Peter Hield, Defence Science and Technology Group (**Author 4**)

Publication list and proportion of work details:

Chapter 2 (Paper 1)

Numerical and Experimental Investigation of Early Stage Diesel Sprays

Laurie Goldsworthy provided testing facility support, advice on interpretation of results and manuscript preparation assistance. Paul Brandner provided advice on interpretation of results and manuscript preparation assistance, Vikram Garaniya and Peter Hield provided manuscript preparation assistance.
[Candidate: 80%, Author 1: 10%, Author 2: 5%, Author 3: 2.5%, Author 4: 2.5%]

Chapter 3 (Paper 2)

Analysis of Diesel Spray Dynamics Using a Compressible Eulerian/VOF/LES Model and Microscopic Shadowgraphy

Laurie Goldsworthy provided testing facility support, advice on interpretation of results and manuscript preparation assistance. Paul Brandner provided advice on interpretation of results and manuscript preparation assistance, Vikram Garaniya and Peter Hield provided manuscript preparation assistance.
[Candidate: 80%, Author 1: 10%, Author 2: 5%, Author 3: 2.5%, Author 4: 2.5%]

[Page intentionally left blank]

Chapter 4 (Paper 3)

End of Injection Processes in a Single-hole Diesel Injector

Laurie Goldsworthy provided testing facility support, advice on interpretation of results and manuscript preparation assistance. Paul Brandner provided advice on interpretation of results and manuscript preparation assistance, Vikram Garaniya and Peter Hield provided manuscript preparation assistance.
[Candidate: 80%, Author 1: 10%, Author 2: 5%, Author 3: 2.5%, Author 4: 2.5%]

We the undersigned agree with the above stated "proportion of work undertaken" for each of the above published (or submitted) peer-reviewed manuscripts contributing to this thesis

Signed:

Dr Laurie Goldsworthy

Primary Supervisor
National Centre for Maritime
Engineering and Hydrodynamics
University of Tasmania

Date: 3/11/2016

Associate Prof Paul. A Brandner

Co-Supervisor
National Centre for Maritime
Engineering and Hydrodynamics
University of Tasmania

Date: 3/11/2016

Dr Vikram Garaniya

Co-Supervisor
National Centre for Maritime
Engineering and Hydrodynamics
University of Tasmania

Date: 3/11/2016

Dr Peter Hield

Co-Supervisor
Defence Science and
Technology Group,
Victoria, Australia

Date: 3/11/2016

[Page intentionally left blank]

Acknowledgements

It is hard to believe my wonderful journey is coming to an end. However, the completion of this thesis marks the beginning of another great adventure ahead. Thus, it is with great pleasure to thank the many people who made this thesis possible.

First and foremost I wish to sincerely thank my primary supervisor Dr. Laurie Goldsworthy for his full support, expert guidance, understanding, and inspiration throughout the study and research. Without his incredible patience and timely wisdom and counsel, my thesis work would have been a frustrating and overwhelming pursuit. Moreover, I would like to extend my deepest gratitude to my co-supervisors Dr. Vikram Garaniya, Assoc. Prof. Paul.A Brandner, and Dr. Peter Hield. It is difficult to overstate my gratitude to them as they have not only been great supervisors but also great mentors. Throughout my thesis, they have provided encouragement, sound advice, good company, and an invaluable amount of feedback and insight with regard to the technical and editorial components of the research. I hope that I can in turn pass on the research virtues that they have so generously shared. I would like recognise Luciano Mason, Dr. Jalal Rafie Shahraki, Dr. Rouzbeh Abbasi, and Dr. Max Haase. They have been both brilliant colleagues and friends who have created a very memorable environment to work, to research and to celebrate.

Special thanks must go to:

- Dr Michael Newman from the Defence Science and Technology Group (DSTG) for his financial support throughout the project.
- Geli Kourakis, Kym Hill, and Nigel Williams for their dedication and continual work on the High Performance Cluster (HPC). The Computational Fluid Dynamics work presented in this thesis would not have been possible without the HPC.

Lastly and most importantly, I would like to dedicate this thesis to my parents as without their unwavering love and moral support over the years none of this would have been possible.

[Page intentionally left blank]

Abstract

Engine manufacturers are constantly aiming to reduce exhaust gas emissions by optimizing the fuel injection process. Despite the wide use of injectors, the key physics governing the injection process are not yet fully understood. The primary atomisation process of the liquid fuel jet is initiated in the injector nozzle and the region close to the nozzle exit, influences secondary atomisation and ultimately the entire spray dynamics. Computational Fluid Dynamics (CFD) which is used in the design of fuel injectors is subjected to further developments through the inclusion of research findings. The present work focuses on processes in the nozzle and the first several nozzle diameters after the nozzle exit of a sharp edged single-hole solid cone injector. The aim of this research is to gain further insight into the primary atomisation at different stages of the injection process; the Start Of Injection (SOI); the Quasi-Steady stage; and finally the End Of Injection (EOI). Experiments are conducted using back- and side-lit microscopic imaging techniques within a constant volume high pressure spray chamber. The numerical method is based on the Volume Of Fluid (VOF) phase-fraction interface capturing technique, in an Eulerian framework integrated with Large Eddy Simulation (LES) turbulence modelling.

The influences of grid resolution, convection interpolation scheme, temporal integration scheme, compressibility, shock waves, phase changes of the liquid jet, and in-nozzle disturbances on the modelling of jet physics are investigated. The early stage liquid jet leading edge demonstrates an umbrella-shaped structure in the numerical results which is in qualitative agreement with experimental imaging. The existence of vortex before liquid fuel emergence suggests the inclusion of air in the nozzle prior to injection. The development of supercavitation down to the end of the nozzle hole leads to the detachment of the liquid from the nozzle walls, associated with the diminution of boundary layer effects and thus reduced in-nozzle turbulence and increased liquid jet velocity. The numerical and experimental results demonstrate the shock waves occur where the jet velocity at the interface with the surrounding air exceeds the local speed of sound. Analysis of the EOI process shows the mechanism of air ingestion into the nozzle liquid due to the high inertia of liquid jet emerging from the nozzle. Numerical results show not only how a single bubble of chamber gas remaining embedded within the liquid in the nozzle hole, but also show entrainment of air into the sac volume of the injector at the EOI. These results provide further insight into the air ingestion process, an explanation for the presence of gas at the SOP in the experimental images. The existence of large droplets at the EOI is shown, which is potentially a source of unburnt hydrocarbons and detrimental emissions in a real engine.

[Page intentionally left blank]

Table of Contents

List of Figures

List of Tables

Nomenclature

A	Area (m^2)
C_a	Cavitation number (-)= $(p-p_v)/ (0.5 \rho U^2)$
C_c	Contraction coefficient (-) = $\pi/(\pi+2)$
C_D	Discharge coefficient (-) = $\dot{m}/((2\varrho(p-p_{injection}))^{1/2})$
d	Droplet diameter (m)
D	Nozzle hole diameter (m)
g	Gravitational acceleration ($m\ s^{-2}$)
h	Initial diameter of the ligament (m)
$\hat{h}$	Enthalpy ($m^2\ s^{-2}$)
I	Identity tensor (-)
K	Kinetic energy ($kg\ m^2\ s^{-2}$)
K_S	Nozzle nominal geometry (-)
L	Nozzle hole length (m)
m	Mass (kg)
$\dot{m}$	Mass flow rate ($kg\ s^{-1}$)= m/t
Ma	Mach number (-)=1/Sin α
n	Unit vector normal to the liquid surface (-)
Oh	Ohnesorge number (-)=$\mu/(\rho\sigma L)$
P	Pressure (Pa)
q	Thermal energy flux vector (-)
Re	Reynolds number (-) = $\varrho\ UD/\mu$
S	Liquid surface indicator (-)
T, t	Time (s)
T	Temperature (°K)
u, v, w	Linear velocities ($m\ s^{-1}$)
U	Velocity ($m\ s^{-1}$)
$\hat{U}$	Internal energy ($kg\ m^2\ s^{-2}$)
V	Volume of the computational cell (m^3)
We	Weber number (-) =$\varrho\ UD/\sigma$
α	Angle of the shock wave relative to the interface (radian)
γ	Volume fraction of liquid (-)
Δ	Subgrid scale length scale (m)= $V^{1/3}$

ε	Subgrid scale turbulent dissipation rate ($m^2\ s^{-3}$)= $C_\varepsilon k^{3/2}/\Delta$
η	Kolmogorov length scale (m)= $(\upsilon^3/\varepsilon)^{1/4}$
k	Subgrid scale turbulent energy ($kg\ m^2\ s^{-2}$)
$\varkappa$	Interface local curvature (-)
μ	Fluid dynamic viscosity ($kg\ m^{-1}\ s^{-1}$)
μ^{sgs}	Subgrid scale viscosity ($kg\ m^{-1}\ s^{-1}$)
υ	Fluid kinematic viscosity ($m^2\ s^{-1}$) = μ/ϱ
υ^{sgs}	Subgrid scale viscosity ($m^2\ s^{-1}$)= $C_k k^{1/2}/\Delta$
ϱ	Fluid density ($kg\ m^{-3}$)
σ	Surface tension ($N\ m^{-1}$)
τ	Viscous stress (Pa)
τ_{PR}	Capillary timescale (s)= $(\varrho h^3/\sigma)^{1/2}$
τ^{sgs}	Subgrid scale stress (Pa)
Ψ	Compressibility (Pa^{-1})

Abbreviations

3D	3 Dimensional
AMC	Australian Maritime College
ASOP	After Start Of Penetration
BSOP	Before Start Of Penetration
CAT	Computer Aided Tomography
CFD	Computational Fluid Dynamics
CFL	Courant-Friedrichs-Lewy
CICSAM	Compressive Interface Capturing Scheme for Arbitrary Meshes
DNS	Direct Numerical Simulation
DSTG	Defence Science and Technology Group
ECN	Engine Combustion Network
EOI	End Of Injection
HEUI	Hydraulic Electric Unit Injector
HPC	High-Performance Cluster
HPSC	High-Pressure Spray Chamber
K-H	Kelvin-Helmholtz
LES	Large Eddy Simulation
LPT	Lagrangian Particle Tracking
LVF	Liquid Volume Fraction
MATLAB	Matric Laboratory
MPI	Max-Planck Institute
NCMEH	National Centre for Maritime Engineering and Hydrodynamics
NS	Navier-Stokes
NV	Normalised Variable
PISO	Pressure Implicit with Split Operator
RANS	Reynolds-Averaged Navier-Stokes
R-T	Rayleigh-Taylor
SGS	Sub-Grid Scale
SOI	Start Of Injection
SOP	Start Of Penetration
TKE	Turbulent Kinetic Energy
TVD	Total Variation Diminishing
VOF	Volume Of Fluid

Chapter 1 :
Introduction

1.1 Background

Global warming and concerns about atmospheric air quality are leading governments to enact strict emission standards for engine manufacturers to meet. The quality of air-fuel mixing is mainly driven by fuel atomisation which plays a vital role in the combustion process and subsequently the production of air pollutants. Engine manufactures are continuously striving to reduce the exhaust gas emissions by optimizing the fuel injection process. However, a wide range of engine operating conditions makes air-fuel mixing optimization difficult [1-3].

Typically, diesel combustion chambers are fed by high-pressure fuel injected as multiple solid cone sprays. Each spray undergoes a series of instabilities (longitudinal and transverse) which lead to the fragmentation of the liquid bulk into liquid structures that further disintegrate into droplets. This initial atomisation process is known as primary breakup and occurs in the vicinity of the injection point. The formation of the fuel spray also involves droplet transport (produced by the primary breakup) and disintegration into smaller droplets. This is secondary breakup which occurs further away from the bulk liquid. The mechanisms involved in primary breakup initiate the atomisation process, control the extent of the liquid core and provide initial conditions for secondary breakup in the disperse flow region [4-7].

Spatially, diesel spray analysis can be broadly divided into three categories, known as:

- In-nozzle flow investigations dealing with processes such as cavitation and turbulence which develop inside the injector
- Primary atomisation or micro spray analysis
- Secondary atomisation or macro spray analysis

Many micro- and macro-scale physical phenomena, as illustrated in Figure 1-1, are described in the literature. These include: in-nozzle cavitation, turbulence, liquid fuel fragmentation, inter-droplet collision, droplet coalescence, and droplet evaporation. Understanding the micro spray structure provides insight into the spray as it deals with microscopic scale physics such as

cavitation, turbulence, and interfacial phenomena. Investigation of the macro spray structure tackles the spray as a whole by quantifying the shape and size of the spray and provides insight into the effect of different parameters such as pressure, velocity, temperature, viscosity and liquid surface tension on droplet size and spray shape. For instance, raising the ambient pressure can lead to larger cone angle and smaller penetration rate of a spray. This analysis can provide guidelines for engine designers to achieve more efficient combustion chamber design.

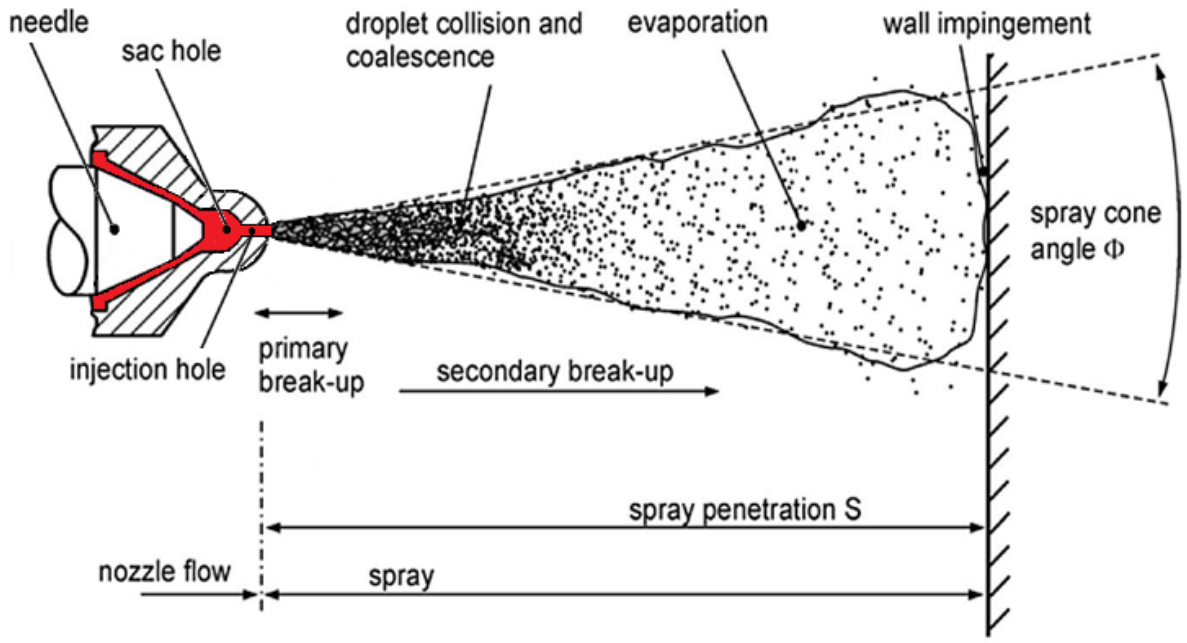

Figure 1-1. Micro- and macro-scale spray structure (adapted from Baumgarten [8]).

Temporally, an injection event can be divided into three stages: (1) Start Of Injection (SOI) corresponding to the needle valve opening transient which is associated with the emergence of the liquid jet from nozzle exit and increases in the injection pressure, (2) Quasi-Steady when the major fuel mass is delivered into the chamber with maximum injection pressure, and (3) End Of Injection (EOI) corresponding to the needle valve closing transient associated with progressive fuel mass flow rate diminution. These stages are illustrated in Figure 1-2 for the injector used in the present study. The needle lift signal is produced by an eddy-current transducer at the end of a relatively long rod used to apply the spring pressure to the injector and so does not necessarily give a precise indication of the needle motion. The spring pressure is set to allow needle lift at a relatively high pressure, which is more characteristic of common rail injectors than of conventional injectors. Injection duration shown in Figure 1-2 is longer than typical values seen in automotive engines but this primarily involves a longer Quasi-Steady stage and does not

significantly impact the SOI and EOI processes nor the behaviour of the Quasi-Steady stage. Larger diesel engines such as those used for marine propulsion have injection durations much greater than automotive engines.

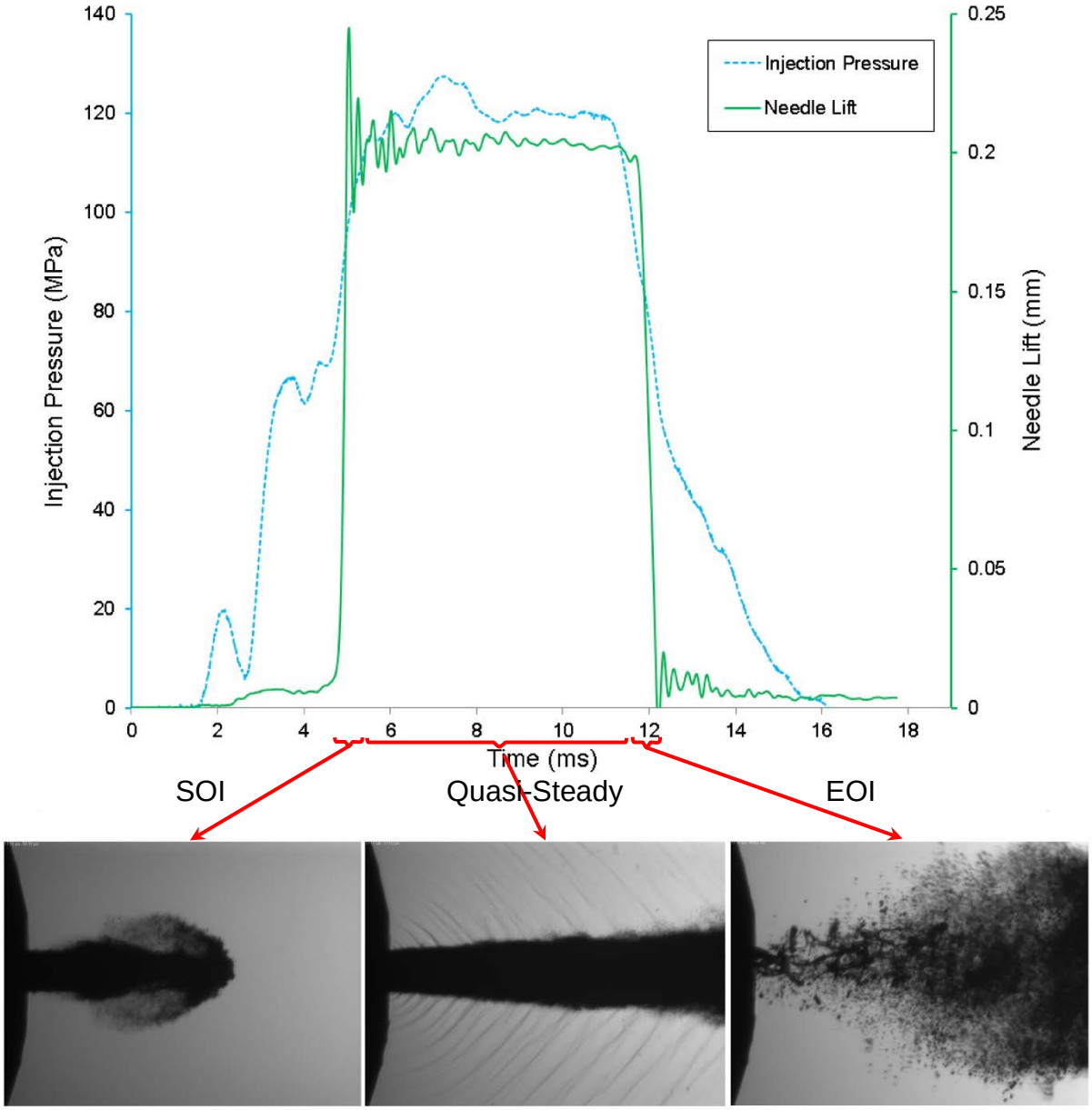

Figure 1-2. Temporal stages of an injection event based on needle and injection pressure profile: Start Of Injection (SOI), Quasi-Steady and End Of Injection (EOI) stages.

The most apparent means of investigating the spray dynamics is the experimental study. Many experimental studies have been performed, e.g. [2, 9-20], using various imaging techniques, to understand the interactive physics of spray dynamics. The recent revolution in high-speed camera technology has facilitated the explanation of the breakup process and spray dynamics [2,

9, 21]. However a clear understanding of the processes controlling atomisation is limited to dilute regions or more global parameters since the observation and measurement of fluid flow properties in the dense region is difficult. The recent developments in X-ray imaging [10, 12, 13, 22-24] are yielding more information on the dense regions and the processes occurring in the nozzle and sac. At present, numerical modelling is the most suitable alternative to characterise spatial and temporal features of multiphase flow involved in atomisation and can provide useful information for engine designers compared with reliance on experimental tests only. Moreover, the combination of numerical modelling with advanced experimental approaches for multiphase flows allows researchers to ensure precise modelling and subsequently allow manufacturers to improve engine efficiency [1, 8, 25, 26]. The approach of using coupled experimental and numerical analysis has attracted a lot of researcher interest recently, more specifically the Engine Combustion Network (ECN) scholars as the leading group in this field [10, 12, 13, 22, 23, 27-32].

Turbulent flows are characterised by eddies with a wide range of length and timescales. The larger eddies are in the size range of the characteristic length of the mean flow while the smallest eddies are characterised the dissipation of turbulent kinetic energy down to the molecular scale. The entire range of eddies can be directly resolved using the Direct Numerical Simulation (DNS) approach; partially resolved using Large Eddy Simulation (LES) which directly resolves large scale eddies and models small eddies; or completely modelled by employing the Reynolds Averaged Navier-Stokes (RANS) approach. Therefore, LES falls between DNS and RANS (regarding the fraction of the resolved scales).

It is impractical to apply DNS for real-world engineering problems dealing with high Reynolds number flow due to its unfeasible computational cost [25]. On the other hand, RANS models cannot capture the full details of the transient spray structures [2, 33]. Thus, the LES approach allows the usage of much coarser meshes and larger time step sizes compared to DNS. While LES needs less computation resource compared to DNS, it still needs high-performance computing machines such as the parallel computing machine [1, 25, 34-36]. The approach of LES can be described as below:

- Mass, momentum, energy, and other passive scalars are carried by large eddies.
- Large eddies are directly affected by the geometries and boundary conditions of the flow.

- Small eddies are less dependent on the geometry, typically isotropic and consequently more universal.

- The availability of feasible turbulence models for small eddies is high.

Different numerical methods are applied in each stage as different physical phenomena with a wide range of length and timescales are involved. There are two main phenomena involved in the flow inside the nozzle, namely cavitation and turbulence. Cavities are created at the nozzle entrance where the pressure within the liquid flow reduces below vapour pressure. The presence of these cavities inside the nozzle [32, 37-45] and their collapse [40-42, 46] influence simultaneous physics such as in-nozzle turbulence and consequently the disintegration of the liquid jet. In-nozzle turbulence also can play a significant role in the breakup process especially at high Reynolds numbers [19, 47-51]. It has been reported as the dominant mechanism [48] in the region close to nozzle exit compared with other mechanisms such as relaxation of the velocity profile [52], drop shedding [47, 53], and fluctuations of injection velocity [25, 52, 54].

1.2 Problem Definition

The overarching problem is that it is difficult to accurately model diesel spray dynamics not only due to the complexity and limited understanding of the various processes and how to model them, but also due to the complexity of numerical modelling techniques and limited computing resources.

Semi-empirical atomisation models such as blob (Reitz-Diwakar) [55], Huh and Gosman [56], Max-Planck Institute (MPI) [57], Arcoumanis [58], Nishimura [59], V. Berg [60], Baumgarten [61] simplify the droplet generation in the dense region which makes the simulation inaccurate and unrealistic. The use of these conventional atomisation models in conjunction with Lagrangian Particle Tracking (LPT), limit the grid fineness [2, 33] near the nozzle and thus does not allow LES to capture the features of the spray and background fluid flow near the nozzle. These limitations motivate the employment of the Eulerian/LES approach to model the primary atomisation.

The early study of two-phase flows was carried out by Anderson et al. [62] and Ishii [63] by deriving the governing equations and applying them in the fluid-fluid formulation. At first, each phase was averaged over a fixed volume, defined separately in the Eulerian framework, and later closure terms were implemented to model the liquid-gas interaction. Therefore, studying the

spray dynamics and breakup processes in an Eulerian framework requires tremendous computational resources due to the small size of individual droplets compared to the averaging volume. Recently, by increasing computer power, this computationally expensive technique can be feasibly utilised to overcome the modelling constraints involved in this subject.

To model the primary atomisation of the liquid bulk in the dense region, air-fuel interface capturing approaches like the level-set or Volume of Fluid (VOF) can be used [1, 4, 27, 34-36, 47, 48, 64]. These methods are typically resolving cases with isothermal immiscible fluids and represent the governing physics to a high degree. However, having a high spatial resolution is a requisite to capture the temporal shape variations of spray structures with such methods. Consequently, this approach is computationally too expensive to be employed for two-phase flows in the dilute spray region with a large number of small droplets. It has been demonstrated that the spray dynamics are strongly governed by primary atomisation [2, 8, 25, 65]. Therefore, implementing an accurate method to predict primary atomisation is critical.

Previously, RANS simulations utilizing the VOF method have been implemented by Vallet et al. [66], but this approach solves the droplet and turbulent scales separately which is inappropriate for spray applications. In recent times, DNS has been employed [47, 64, 67, 68] to characterise temporal phenomena of two-phase flow. As mentioned before, since the DNS is too computationally expensive and as such is limited to low Reynolds number flows, LES remains the best alternative to characterise transient mechanisms at high Reynolds numbers in a reasonable time. However, the lower limit of the size of a droplet that can be captured is governed in the Eulerian/VOF by the minimum cell size.

Modelling spray dynamics accurately and consistently in a reasonable computational time during all stages has been a challenging subject for more than a decade. In the present work, the Eulerian/VOF/LES method is employed to capture diesel injector in- and near-nozzle flow physics.

1.3 Objectives

The objective of all research on diesel sprays is to facilitate optimization of fuel injection for increased efficiency and reduced emissions. Thus, specific objectives include the development of more accurate predictive tools and the development of greater understanding of the many processes involved and their interactions. The specific aims of the present project are to investigate the in- and near-nozzle multi-phase flow dynamics at the different stages of injection

by conducting both quantitative and qualitative examination of spray characteristics through CFD and experimental work. The motivation behind the study is to gain insight into the significance of each conjugate phenomenon on spray features of a sharp edged single-hole high-pressure diesel injector and to demonstrate the accuracy of the applied modelling techniques.

Due to the previously described challenges associated with CFD, experimental tests were carried out in conjunction to validate the CFD models and supplement the investigation. Based on the work, the influence of the simultaneous interactive physics on fluids dynamics at in- and near-nozzle regions, and guiding principles with regard to CFD modelling of the problem are presented. More specifically, the aims of this study can be listed as:

1. Implement an Eulerian/VOF/LES primary atomisation model for the in- and near-nozzle region.

2. Gain insight into the physics involved in an injection event at the SOI, Quasi-Steady, and EOI stages.

3. Investigate the effect of grid size on the prediction of the turbulence spectrum and fragmentation process of liquid jet and resulting droplet size spectrum.

4. Investigate the effect of temporal and spatial numerical discretization schemes on the prediction of in-nozzle turbulence and interfacial phenomena.

5. Investigate the influence of cavitation on in-nozzle flow and spray dynamics.

6. Investigate the significance of fluid compressibility at different stages of injection.

7. Achieve a clearer understanding of the air ingestion mechanism during the EOI process for different scenarios such as incompressible non-cavitating and compressible cavitating models.

8. Set up and conduct experimental tests using back-light imaging techniques which provide requisite data for evaluation of CFD results.

9. Validate the numerical results by comparison with experimental measurements.

1.4 Description of nozzle geometry

The X-ray Computer-Aided Tomography (CAT) analysis of the Australian Maritime College (AMC)'s injector was conducted commercially by the Centre for Materials and Surface Science and the Centre of Excellence for Coherent X-ray Science at La Trobe University to reveal the details of the internal geometry of the nozzle. CAT analyses small physical structures by making use of the different absorption of X-rays for different materials ("absorption contrast"). Using reconstruction algorithms, a 3D view of the sample was computed as shown in Figure 1-3, which allows the interior geometry of the material to be quantified non-destructively. The detailed results of the CAT analyses are provided in Appendix 1.

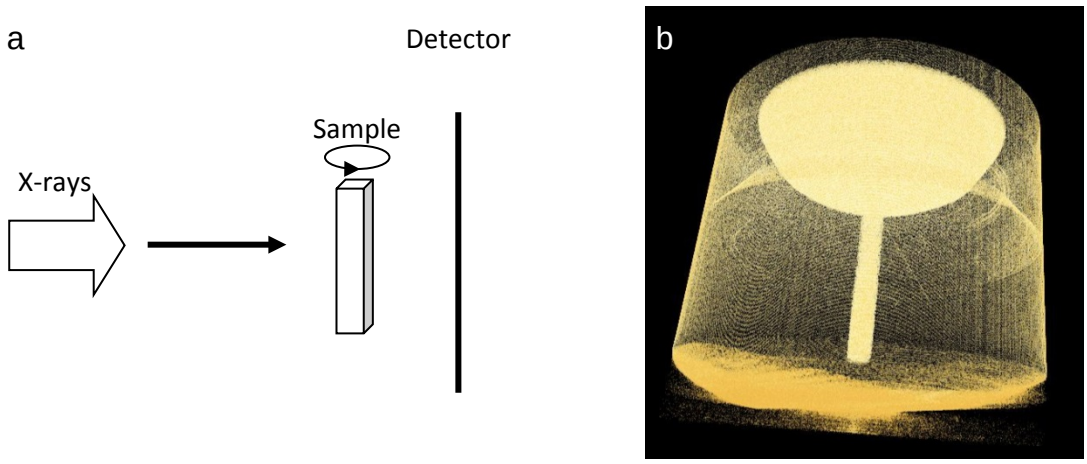

Figure 1-3. (a): experimental X-ray Computer-Aided Tomography setup; (b): a reconstructed 3D view of the nozzle.

Based on the X-Ray Tomography images, realistic geometry of the nozzle was created in AutoCAD software and then exported to grid generation software.

1.5 Methodology

This research includes both experimental and numerical studies. Experimental studies were performed in order to provide important data about the general spray characteristics such as spray cone angle and penetration velocity which are unavailable in the literature, and to also validate the numerical method and set up.

1.5.1 Experimental setup

AMC's constant volume High-Pressure Spray Chamber (HPSC) allows experimental analysis of diesel sprays. The typical setup of the HPSC with rail platforms, translation stages, and attached measuring equipment is shown in Figure 1-4.

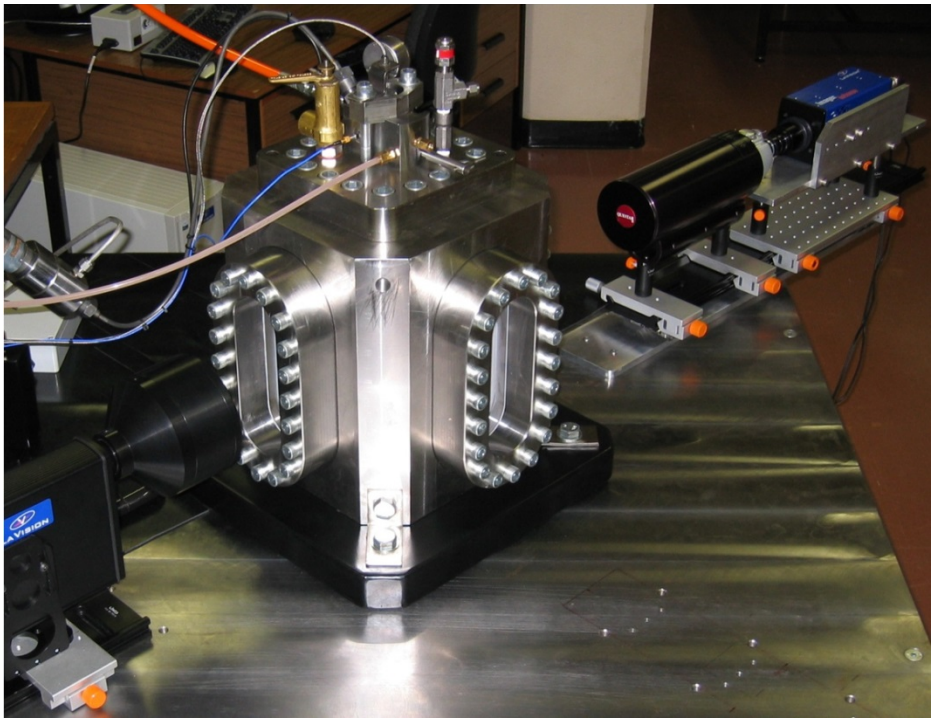

Figure 1-4. AMC's HPSC facility for shadowgraphy measurements.

Micro spray structure and physics of the spray were studied by backlit (shadowgraphy) and sidelit imaging techniques which employ a microscope for imaging the primary atomisation zone. Measured data help to understand flow behaviour in the dense region such as: the general morphology of the emerging jet and the jet at the EOI; jet propagation rate and the onset and nature of shock waves; and the early spray cone angle. These measures enhance understanding of the spray dynamics and are important for validating the numerical results.

1.5.2 Numerical modelling

To capture the in- and near-nozzle flow dynamics, the VOF phase-fraction based interface capturing technique integrated with LES turbulence modelling in an Eulerian framework is used through an open source CFD code, OpenFOAM.

Numerical models replicate the experimental test conditions including the pressure of diesel fuel at nozzle inlet; the pressure of the spray chamber (ambient zone); and temperature and viscosity of air and diesel fuel. Considering the boundary layer, the atomisation zone and the no-slip condition at the walls, a 3D hexahedral structured mesh was generated using GridPro software. Different mesh resolutions were produced in order to perform a mesh dependency study with very coarse (600×10^3 cells), coarse (4×10^6 cells), medium (8×10^6 cells), and fine (20×10^6) mesh resolutions. This research covers all three temporal stages of injection: the SOI, the Quasi-Steady, and the EOI though the experimental test and numerical analysis. Numerical models tackle the fluid physics using a time-saving incompressible model and a more realistic compressible model. The compressible model requires around 10 times the computational time of the incompressible model.

An implicit finite-volume method which uses second order spatial and temporal discretization schemes is used to solve the mathematical models. The solution procedure employs the Pressure Implicit with Split Operator (PISO) algorithm [69]. The efficiency and effects of different numerical schemes have been investigated.

1.6 Scope and limitations

The focus of the present study is on the characterization of the in- and near-nozzle flow dynamics using an Eulerian/VOF/LES approach and experimentation. The numerical investigations are conducted through a non-cavitating incompressible model and a cavitating compressible model where predicted data are evaluated and validated using experimental results. The simple time-efficient incompressible model provides a benchmark for best model setup considering various numerical schemes, and grid resolutions while the more complicated compressible model delivers clearer understanding of conjunct phenomenon occurring during an injection event. These analyses cover the full cycle of an injection event including the SOI, Quasi-Steady, and EOI stages. The scope of this study is: firstly, to describe structures of an emerging jet versus time; secondly, to investigate the robustness of the models in capturing the most realistic physics; lastly, to quantify impacts of physics associated with the in- and near-nozzle flow features on primary atomisation of a high pressure diesel spray.

This study is limited to the in- and near nozzle flow dynamics of a single-hole high pressure diesel spray. The nozzle is of constant radius and the entrance is sharp–edged. Needle lift dynamics and flow between the needle and seat are not modelled. The numerical models replicate the needle valve opening and closing feature through a linear first order temporal

pressure profile at nozzle sac inlet. Cavitation is modelled by allowing fuel to vapourise at its vapour pressure. The vapour is given the properties of air and condensation is not modelled. The thermodynamic properties of dodecane are used for diesel fuel.

1.7 Outline of Thesis

This thesis follows a "chaptered thesis" structure, where Chapters 2 to 4 are comprised of scientific papers. The structure of the thesis is outlined below.

Chapter 1: The introductory chapter, which clarifies the research question, objectives, and methodology of the project, including a brief description of the issues and past work on the fluid physics within the high-pressure nozzle and the spray breakup. It also outlines the structure of the thesis, linking together the subsequent chapters consisting of the scientific papers.

Chapter 2: This chapter focuses on the analysis of the spray structure at the SOI and Quasi-Steady stages of injection, considering each fluid as an incompressible continuum with constant density and viscosity in the absence of a cavitation model. Qualitative and quantitative experimental data from backlit imaging was used to validate the numerical results. This enables the validated CFD models to be used for further analysis of the spray dynamics and to clarify the impact of simultaneous physics on the fragmentation processes of the emerging liquid jet. The ability of Eulerian/VOF/LES-based CFD to reproduce the experimentally captured jet structure and penetration velocity and spray angle is demonstrated, showing that the selection of the boundary conditions, turbulence models and the quality of the mesh model can have a significant effect on the results. The influence of first and second order temporal discretization schemes and convection schemes on the computed morphology of the spray is been discussed and compared to experimental data. These results show that with a sufficiently fine mesh, and simulation conditions matching the experiments; the second order time derivative scheme and the Normalised Variable advection scheme give favourable comparisons with experimental measurements. The CFD methodology and key findings from Chapter 2 are used to provide the basis and support for the more comprehensive, complex and time-consuming simulations of in- and near-nozzle flow phenomena, as described in the subsequent chapters.

Chapter 3: Investigates the interacting effects of cavitation and in-nozzle turbulence on the disintegration process of the emerging liquid jet. The analysis is conducted at both SOI and Quasi-Steady stages through a compressible cavitating model. The experimental images captured a toroidal vortex just before and after the start of the jet emergence providing evidence that the

nozzle is only partially full of liquid at the SOI. The simulations were carried out by implementing the partially filled nozzle where the accuracy of these estimations have been compared with the experimental data. The impact of cavitation inception and development of in-nozzle turbulence and consequently on the spray structure has been investigated at the SOI. An edge detection technique is adopted for defining the experimentally measured shock waves to allow the prediction of jet interface velocity at various ranges of axial distance from the nozzle exit. Computed interface velocity is compared with experimentally measured values.

These findings provide further insight into the interactive physics of the processes associated with high-pressure diesel fuel injection and how the spray dynamics may be affected.

Chapter 4: Presents analysis of the mechanisms occurring during the EOI transient both experimentally and numerically. A time efficient incompressible model sheds light on the air ingestion mechanism after needle valve closure while a more advanced compressible cavitating model provides a clearer understanding of the effect of cavitation on the processes involved during the EOI. The models demonstrate how inertia dominates the fluid dynamics leading to the enhancement of interfacial instability and ultimately the ingestion of air inside the nozzle liquid. The compressible model shows how cavitation can alter the process and lead to the penetration of chamber gas into the sac liquid. The presence of air inside the nozzle liquid can not only highlight the significance of the EOI on next spray dynamics but also an explanation for the source of deviation between measurement and computation. Various chamber pressures and ramp pressure profiles at the sac inlet were investigated. Last but not least, the fragmentation process, breakup regime of low-speed ligaments, and formation of numerous large droplets at the final stage of the EOI are discussed. The presence of these droplets with various diameter ranges provides additional evidence as to the importance of the EOI process on the formation of unburnt hydrocarbons.

Chapter 5: The concluding chapter provides an overall summary of the project, bringing together the findings of the individual chapters. The implications of the findings, the limitations, and recommendations for future work are discussed.

Appendices: Appendix I outlines the nozzle geometry based on X-ray micro computed Tomography. **Appendix II** contains a peer reviewed conference paper presented by the author. **Appendix III** contains a peer reviewed conference paper which will be presented by the author. **Appendix IV** compares the CFD results using LimitedLinear and Gamma schemes.

Chapter 2 :

Numerical and Experimental Investigation of Early Stage Diesel Sprays

This chapter has been published in "Fuel". The citation for the research article is:

M. Ghiji, L. Goldsworthy, P.A. Brandner, V. Garaniya, and P. Hield, Numerical and experimental investigation of early stage diesel sprays, *Fuel*, Volume 75, Pages 274-286 (http://dx.doi.org/10.1016/j.fuel.2016.02.040).

Abstract

Experimental and numerical investigations of primary atomisation in a high-pressure diesel jet are presented. Information on flow processes and structures inside and near nozzle exit are described at early and Quasi-Steady stages of injection. The numerical method is based on the Volume Of Fluid (VOF) phase-fraction interface capturing technique, in an Eulerian framework. The influence of grid resolution, convection interpolation scheme and temporal integration scheme on the modelling of jet physics are investigated. The present flow setup includes in-nozzle disturbances with the no-slip condition at the walls. All experimental operating conditions are replicated in the numerical models. The early stage liquid jet leading edge demonstrates an umbrella-shaped structure in the numerical results which is in qualitative agreement with experimental imaging. Data obtained provide insight into the flow behaviour in the dense region including commencement of fragmentation and early spray angle formation. Experimental images show a cloud of air-fuel mixture at the early stage of injection. The existence of ingested air inside the injector after needle closure could be the source of the observed deviation between experimental and numerical results. The results show that the jet break-up rate and liquid core length increase in cases with higher grid resolutions. The early spray angle from the numerical results at the Quasi-Steady stage, shows good agreement with experimental data.

2.1 Introduction

Steady and unsteady liquid jet flows and their breakup remain an ongoing field of investigation [1, 4, 10, 13, 25, 33, 70, 71]. Jets are of broad interest for the study of many basic phenomena and in a range of physical processes. They occur at length scales ranging from the order of atomic to that of the universe. In many applications, they may be multi-phase and involve multiple phase changes, chemical reactions and complex flow phenomena.

Human impacts on the environment and more specifically global warming are increasing government concerns on strict emission standards for engine manufacturers. The quality of air-fuel mixing is mainly driven by atomisation of the injected liquid jet, which plays an important role in the combustion process, ultimately controlling production of pollutants. Engine manufacturers are constantly aiming to reduce exhaust gas emissions by optimizing the fuel injection process. A wide range of engine operating conditions makes the optimization of air-fuel mixing difficult [2, 7, 25, 72]. The motivation, on one hand, is practical applications such as manufacturing of diesel engine injectors and, on the other hand, understanding the origin of key phenomena of atomisation and its influence on jet breakup processes.

In diesel engines, combustion chambers are fed by high-pressure fuel injected as a solid cone spray. This spray undergoes a series of instabilities (longitudinal and transverse) which lead to the fragmentation of the liquid bulk into structures that further disintegrate into droplets. This initial process of atomisation is called primary breakup and occurs in the vicinity of the injection point. Primary breakup mechanisms initiate the atomisation process, control the extent of the liquid core and provide initial conditions for secondary breakup in the disperse flow region [4-7].

Despite the fact that atomisation is widely utilised and significantly affects engine combustion processes, heat release rate and exhaust emissions [47, 49, 70, 73, 74], the characteristics of the spray produced (for example size and velocity distributions of droplets) are still not well predicted due to the small length and time scales and high liquid fractions involved, especially inside the jet.

So far, many theories have been proposed to describe the primary atomisation mechanism, including: aerodynamic shear forces which act through stripping and Kelvin-Helmholtz (K-H) instabilities [8, 25, 75]. Turbulence-induced disintegration has a significant effect on jet breakup at higher Reynolds numbers $Re_l = \varrho_l U D / \mu_l$, where ϱ_l is the liquid density, U is the liquid velocity, D is the orifice diameter, and μ_l is the dynamic viscosity [19, 47-51]. Relaxation of the

velocity profile, creates a bursting effect especially in non-cavitating jets and large velocity differentials [52]. Cavitation-induces disintegration of the jet due to the reduction of cross-sectional area at the nozzle inlet [40-42, 46]; and liquid bulk oscillation provoking toroidal surface perturbations [25, 54].

Less of a consensus has been achieved in determining the dominant mechanisms of early breakup when a high-speed liquid jet is injected into a pressurised dense gas. Many interdependent phenomena can provoke severe velocity fluctuations leading to a nonlinear instability of the flow inside the nozzle. These phenomena include turbulence [19, 48-51] generated by the nozzle geometry and by the collapse of cavitating bubbles [40-42, 46]. In addition to turbulence, fluctuations of the injection velocity [52] and drop shedding [47, 53] contribute to the primary breakup. Experimentally separating and investigating these different effects is very difficult. For the development of diesel engines with both optimal fuel economy and minimum pollutant emissions, it is necessary to comprehend the spray processes and then characterise the effects of different parameters and engine operating condition on fuel flow structures. This is a challenging subject to study, both experimentally and numerically [15, 36, 71, 73, 75]. In this study, the flow inside the nozzle and the liquid bulk near the nozzle exit and its fragmentation (primary atomisation) are investigated.

This paper concentrates on the effect of in-nozzle turbulence. The effects of cavitation will be studied in future work. Turbulent flows are represented by eddies with an entire range of length and time scales. Large eddy simulation (LES) directly resolves large scale eddies and models small eddies. Simulating only small eddies and solving the large eddies allows the use of much coarser meshes and longer time steps in LES compared to Direct Numerical Simulation (DNS). Despite this, LES still needs principally finer meshes compared to the ones used for Reynolds Averaged Navier Stokes (RANS) computations. Since RANS models cannot capture the transient spray structure [2, 4, 25, 33] including droplet clustering and shot to shot variability, LES is applied to overcome these limitations.

Literature reviews of the existing atomisation models, demonstrated that all these models (blob, Huh/Gosman, MPI, Arcoumanis, Nishimura, V.Berg, Baumgarten, ReitzWave model, Taylor Analogy Breakup model) [2, 36, 76] simplify droplet generation in the dense region (primary atomisation) which might make the simulation inaccurate and unrealistic [33, 75]. For example, the blob model as the most employed model not only simply generates parcels with the size of the nozzle diameter but also does not take into account the physics of in-nozzle turbulence and in-nozzle cavitation. In addition, these conventional atomisation models with

Lagrangian Particle Tracking (LPT), limit the grid fineness near the nozzle and do not allow LES to capture the features of the spray and background fluid flow near the nozzle. Furthermore, refining the grid with the blob method results in problems with high liquid fraction in the LPT approach (too much liquid in each cell) [2, 4, 33, 68]. These limitations motivate the use of the Eulerian approach to model the primary atomisation, instead of using conventional atomisation models. With ever increasing computational power, there is an incentive to use more complex models for primary atomisation. This is a key aim of the present work.

To date, considerable progress has been made in the development of rigorous numerical methods for performing highly resolved simulations of multiphase flow [25, 77]. The accuracy of different numerical techniques for modelling the primary atomisation of a liquid diesel jet was investigated in detail for low Re (Re < 5000) by Herrmann [48] and Desjardins & Pitsch [78]. Herrmann [48], demonstrated the importance of the grid resolution on capturing the accurate phase interface geometry of diesel liquid with an injection velocity of 100 m / s and Re = 5000. Turbulence was reported as the dominant driving mechanism of atomisation within the first 20 nozzle diameters downstream.

Due to the lack of detailed studies of the primary atomisation of diesel liquid jets under real diesel engine operating conditions, the present study focuses on the structure of primary atomisation with an accelerating injection pressure up to 1200 bar, background pressure of 30 bar, liquid Reynolds number within the range $7000 \leq Re_l \leq 37000$, and liquid Weber number of $We_l \approx 933843$ at the Quasi-Steady stage. The liquid Weber number $We_l = \varrho_l U_p D / \sigma$, where U_p is the droplet relative velocity, D is the nozzle hole diameter and σ is the surface tension. The Reynolds number is calculated based on average liquid velocity at the nozzle hole exit. The large range of Re is due to rising pressure at the sac inlet, changing from 30 bar at the beginning of injection up to 1200 bar at the Quasi-Steady stage of injection. In-nozzle cavitation is not considered in this work however this constraint will be eliminated in further studies. The present work focuses on the very early stages of injection as it is likely that instabilities generated in the early stages have significant effect on the development of the whole spray. Non-evaporating conditions are employed to simplify the physical complexities.

2.2 Methodology

2.2.1 Experimental apparatus

Non-evaporating diesel fuel spray measurements were conducted with a laser based imaging system in a constant volume High-Pressure Spray Chamber (HPSC). The HPSC operating volume is a square-section prism with rounded corners and the axis vertically oriented. Optical access to the injection test chamber is via three windows in the test chamber walls 80 mm thick, UV quality, optically polished quartz, and viewing area of 200 × 70 mm. The light source is a 120 milliJoule dual-cavity Nd:YAG laser capable of light pulses around 5 ns duration.

The chamber is pressurised to 30 bar with temperature and density of 298 K and 35 kg/m^3, respectively, to give air density in the range of a heavy duty diesel engine. Diesel fuel is axially injected through a single solid cone fuel nozzle with an injection pressure of around 1200 bar from the top of the HPSC as shown in Figure 2-1.

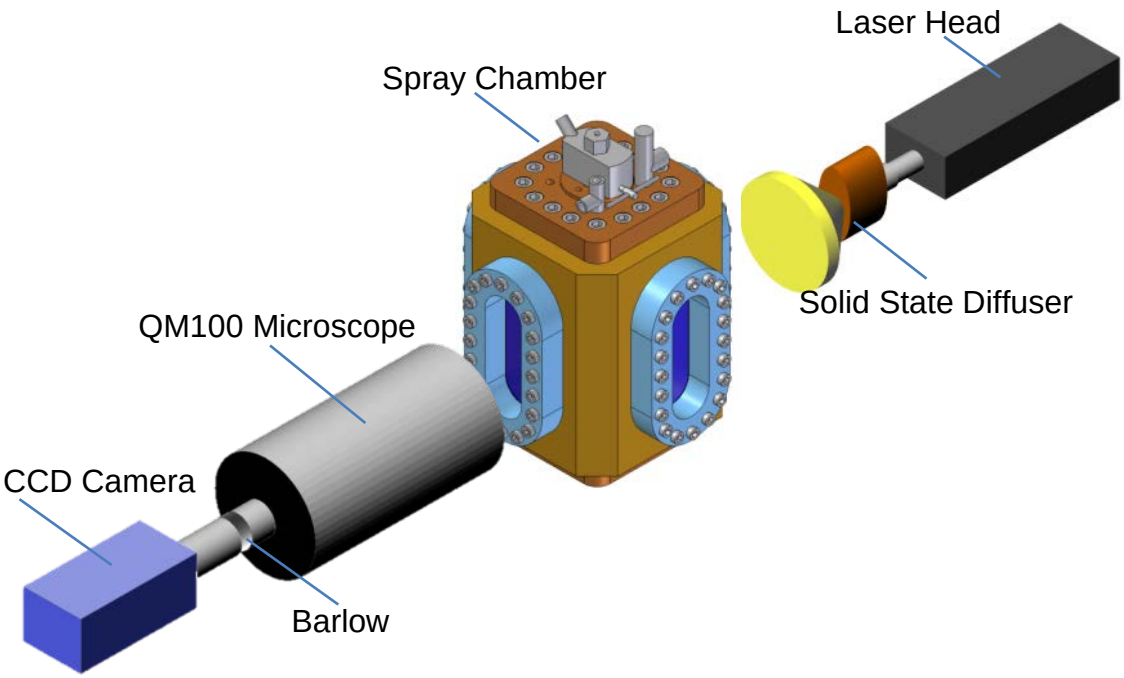

Figure 2-1. Schematic view of the High-Pressure Spray Chamber showing laser and camera setup for shadowgraphy measurements.

The injection pressure profile which is highly repeatable from shot to shot is replicated based on the previous study of Bong et al [2]. The injector needle valve snaps open when the

injector pressure achieves a given value, as determined by the tension of the needle valve spring. Needle lift is monitored using an eddy current proximity probe. It takes about 0.2 ms for the needle valve to lift completely.

The acquisition sequence is triggered by a pulse from the injector driver and the delay to the start of image acquisition is measured separately. The needle lift signal and the pulse generated by the laser were recorded using a digital oscilloscope to record the time at which the laser light pulse is activated, as indicated by the Q-switch pulse. Using shots obtained at the point where the spray is just starting to emerge from the nozzle, it is established that there is a delay of 100 ± 5 μs between start of injection and a significant response from the needle lift transducer. This information enables timing of subsequent shots.

A laser-based backlit imaging method (shadowgraphy) is used to investigate the micro-spray structure. As depicted in Figure 2-1, a Questar QM100 long distance microscope is attached to a LaVision Imager Intense dual-frame, 12 bit CCD camera with 1376×1040 pixels. The camera and laser allow only two images to be taken for each shot of the injector. The delay between the two images can be as low as 0.5 μs. The use of closely spaced images allows estimation of the propagation velocity of the leading edge of the injected fuel. An interval of about 30 s is allowed between injector shots to allow the chamber to settle.

The spray is backlit with laser light through a standard solid-state diffuser supplied by LaVision. The diffuser employs laser-induced fluorescent from an opaque plate impregnated with a fluorescent dye. The camera is focused, aligned, and calibrated on a graduated scale on the spray axis.

Two sets of microscopic data are achieved with and without using a Barlow lens. With the 2x Barlow lens, mounted between CCD Camera and Microscope, a magnification of 7.7:1, a field of view of 1157×860 μm and a spatial resolution of 0.84 μm/pixel are achieved. These sets of data are used as a benchmark to validate the numerical results close to the nozzle exit.

2.2.2 Simulation setup

2.2.2.1 Mathematical method

In this study, the VOF phase-fraction based interface capturing technique similar to de Villiers et al [72] is employed in the open source numerical code OpenFOAM v2.3. The code

considers the two-phase flow field as a single incompressible continuum with constant density ϱ and viscosity μ, including surface tension. The compressibility effect will be included in future studies. The basic form of the governing mass and momentum conservation are:

$$\nabla.\mathrm{V} = 0 \tag{2-1}$$

$$\frac{\partial \rho \mathrm{V}}{\partial \mathrm{t}} + \nabla.(\rho \mathrm{V}\mathrm{V}) = -\nabla \mathrm{p} + \nabla.\tau + \int_{\mathrm{S(t)}} \sigma \mathrm{k}' \mathrm{n}' \delta(\mathrm{x} - \mathrm{x}') \mathrm{dS} \tag{2-2}$$

where V is the velocity, p is the pressure, t is the time, τ is the stress tensor, $\varkappa$ is the local curvature of the liquid surface and, n denotes a unit vector normal to the liquid surface S. The operators $\nabla(\,)$ and $\nabla.(\,)$ represent the gradient and the divergence operations, respectively. The integral term in equation (2-2) represents the momentum source due to surface tension force on the interface $S(t)$. This force only acts on S, as ensured by the indicator function $\delta(\ldots)$. The time-varying phases interface $S(t)$ is located accordingly using a VOF surface-capturing approach which utilises the volume fraction γ of diesel fuel as an indicator function, defined as:

$$\gamma = \begin{cases} 1 & \text{for a point inside the liquid} \\ 0 < \gamma < 1 & \text{for a point in the transitional region} \\ 0 & \text{for a point inside the air} \end{cases} \tag{2-3}$$

The 'transitional region', where the interface is located, utilised as an artefact of the numerical solution process. Fluid in a transition region is considered as a mixture of the two fluids on each side of the interface, which cannot completely resolve a discontinuous step. The transport equation for the indicator function is:

$$\frac{\partial \gamma}{\partial t} + \nabla.(V\gamma) = 0 \tag{2-4}$$

According to the definitions of γ, the local thermo-physical properties are given by:

$$\rho = \gamma \rho_l + (1 - \gamma)\rho_g \tag{2-5}$$

$$\mu = \gamma \mu_l + (1 - \gamma)\mu_g \tag{2-6}$$

where the subscripts l and g represents the liquid and gas, phases respectively.

The LES/VOF equations are derived from equations (2-1), (2-2) and (2-4) using localised volume averaging of the phase-weighted hydrodynamics variables. This process known as

filtering, includes decomposition of the relevant variables into resolvable and sub-grid scales of turbulent fluctuations. As the results of the filtering process, the sub-grid scale fluctuations will be eliminated from direct simulation. This filtering together with the non-linear convection terms in equation (2-2) introduce an additional quantity, comprising correlation of the variable fluctuations at sub-grid scales that entail closure through mathematical models, known as the subgrid scale (SGS) stresses $\boldsymbol{\tau^{sgs}}$ as they signify the influence of the unresolved small scales of turbulence, given by:

$$\tau^{sgs} = \overline{\boldsymbol{V}\boldsymbol{V}} - \bar{\boldsymbol{V}}\,\bar{\boldsymbol{V}} \tag{2-7}$$

and estimated by a single subgrid scale model of the eddy-viscosity type:

$$\tau^{sgs} - \frac{2}{3}\,k\,\boldsymbol{I} = -\,\frac{\mu^{sgs}}{\rho}\,(\nabla\,\bar{\boldsymbol{V}} + \nabla\bar{\boldsymbol{V}}^{T}) \tag{2-8}$$

where $\boldsymbol{k}$ is the subgrid scale turbulent energy and $\boldsymbol{\mu^{sgs}}$ is the subgrid scale viscosity, both are determined from the one-equation SGS turbulent energy transport model accredited to Yoshizawa [79].

$$\frac{\partial k}{\partial t} + \nabla.(k\bar{V}) = \nabla.[(\upsilon + \upsilon^{sgs})\nabla k + \tau^{sgs}\cdot\bar{V}] - \varepsilon - \frac{1}{2}\tau^{sgs} : (\nabla\bar{V} + \nabla\bar{V}^{T}) \tag{2-9}$$

where $\boldsymbol{\varepsilon} = C_{\varepsilon}k^{3/2}/\Delta$ is the SGS turbulent dissipation rate, $\boldsymbol{\upsilon^{sgs}} = C_{k}k^{1/2}/\Delta$ and $\Delta = \sqrt[3]{\boldsymbol{V}}$ is the SGS length scale where $\boldsymbol{V}$ is volume of the computational cell. The coefficients, found from statistical considerations, are C_k = 0.05 and C_ε = 1 [33].

2.2.2.2 Numerical solution method

Mathematical models for this simulation are solved using an implicit finite-volume method, which employs spatial and temporal discretization schemes. This method preserves a sharp interface resolution by including a compression velocity term [80] in the phase transport equation, acting to compress the VOF interface. The solution procedure utilises the Pressure Implicit with Split Operator (PISO) algorithm [69], together with conjugate gradient methods for coupled solution of mass and momentum conservation equations which is specifically suited to transient flows [81].

In order to preserve the proper physical limits on the fluid-dynamics variables, different integration schemes are tried from highly dissipative up to highly conservative. In this study, the

advection terms are solved by the Normalised Variable (NV) Gamma differencing scheme [82]. A conservative, bounded, second-order scheme is used for Laplacian derivative terms and a second-order, implicit discretization scheme is used for time derivative terms. The numerical integration time-step is adjusted by various stability criteria, and is of the order 1×10^{-9} s for the fine case.

2.2.2.3 Boundary conditions and initial setup

Atomisation is affected by the design of the sac and nozzle orifice inlet which consequently influence primary breakup [25, 47, 75]. The computational domain has therefore been modelled using the geometry of the experimental nozzle determined using X-ray Computer Aided Tomography (CAT) analysis as shown in Figure 2-2. This analysis reconstructs the images with pixel numbers of 1016 × 1024 × 1024, and effective voxel size of 2.318 μm.

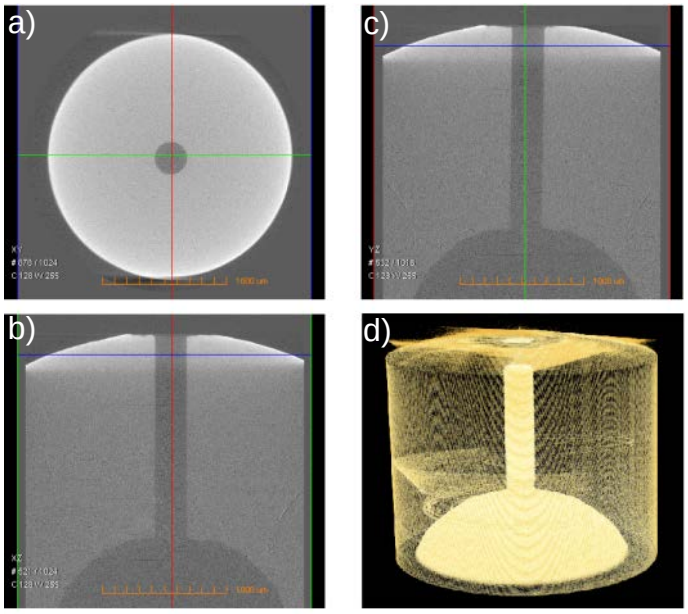

Figure 2-2. X-Ray Tomography measurement of sac and nozzle geometry and dimensions. a) X-Y view; b) X-Z view; c) Y-Z view and d) 3D view of nozzle. Images provided by The Centre for Materials and Surface Science and the Centre of Excellence for Coherent X-ray Science at La Trobe University, employing an Xradia MicroXCT instrument.

All the experimental conditions were replicated in numerical models including the sac volume inlet, spray chamber pressure and air and diesel fuel temperature and viscosity. Fuel properties and set up conditions are listed in Table 2-1. The sac inlet pressure is ramped from 30 bar initially to 850 bar after 50 μs then to 1200 bar after a further 25 μs then constant at 1200 bar to the end of simulation. This is to some extent arbitrary but is premised on published data

implying that the sac pressure rises rapidly during needle opening [10, 28, 29, 83]. For instance, Moon et al. [10] found that the Quasi-Steady stage jet velocity was reached when the needle lift was only 17% of the maximum needle lift. The ramp was chosen to give an approximate match of modelled and experimental penetration rates. The lower pressure rise rate in the second 25 μs was adopted to avoid numerical instabilities.

In the present study, it was found that the duration of the needle lift is about 200 μs and that the signal from the eddy current needle lift transducer signal has a delay of around 100±5 μs compared to actual needle lift. This is determined by observing the timing of the laser Q-switch signal relative to the needle lift signal for shots where the captured image shows the spray just starting to emerge from the nozzle. Thus, the needle lift signal could not be used to determine instantaneous needle position. The maximum needle lift is about 200 μm.

Table 2-1. Fuel properties and operating conditions based on experimental setup [84]. * Injection velocity, Weber and Mach numbers are for the Quasi-Steady stage of spray [84]. The nozzle diameter is used as the length scale.

Parameter	Value
Injection pressure	120 MPa average
Nozzle diameter	0.25 mm
Nozzle length	1.6 mm
Nozzle nominal geometry	$K_S = 0$
Fuel	Diesel
Diesel fuel density	832 kg/m^3
Gas	Compressed air
Density ratio	42
Fuel Kinematic viscosity	2.52×10^{-6} m^2/s
Surface tension	0.03 N/m
Temperature	25°C
Fuel Re_l	$7000 \leq Re \leq 37000$
*Indicative injection velocity	367
*Fuel Mach number	367 / 1250 = 0.3
*We_l	933843
*Ohnesorge number	0.077
Chamber pressure	30 bar

The nozzle orifice at the start of each injection in the experimental injections is not necessarily full of fuel due to needle bounce and dribble phenomena at closure nor empty of fuel due to cohesive and adhesive forces. Hence for a good comparison of modelled and measured

injection, a method for determining the position of the liquid-gas interface in the nozzle orifice at the start of injection was implemented. Firstly, the sac and three quarters of the nozzle were filled with diesel fuel at a pressure of 30 bar and then the sac inlet pressure raised as described above. Later on, at the end of the injection cycle when the needle closes, the boundary condition is changed from inlet to wall to prevent any further fuel entering the sac, emulating the needle valve closure process. The result of this simulation is that the nozzle fills with liquid to 5.2 D (81% of the nozzle length) from the nozzle entrance. This is due to the equilibrium between adhesive forces, surface tension of the liquid phase and hydrodynamic forces amongst liquid and pressurised air in the spray chamber. The position of the liquid-gas interface inside the nozzle orifice resulting from this simulation (at 5.2 D) is used to initialise the main simulation. This starting point is somewhat arbitrary but goes some way to accounting for air ingestion as described in [12, 28, 29, 83].

Considering the boundary layer, atomisation zone and no-slip condition at the walls (sac and orifice), a hexahedral structured mesh was generated as shown in Figure 2-3. It has been reported that the spray structure is not axisymmetric [2, 4, 47, 68, 84], therefore the full computational domain (360°) of the atomisation zone is meshed.

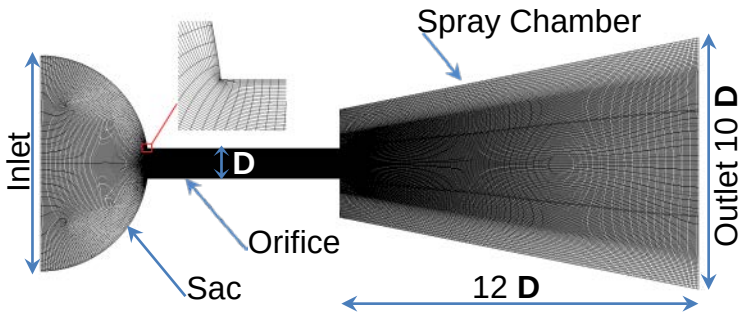

Figure 2-3. Computational domain and boundary conditions (coarse case, with refined mesh in the orifice and atomisation regions).

In order to conduct a mesh sensitivity study, three different mesh resolutions are generated with coarse (4 million cells), medium (8 million cells), and fine grids (20 million cells). Cell size is refined down to 0.1 μm in the orifice and 1.7 μm in the primary atomisation zone in the finest resolution case. This cell size can capture droplets down to the 10 μm range based the optimistic premise that 5 cells can give reasonable representation of a single droplet [48]. The resolution of these cases, time-step range, number of CPUs, and computational cost (wall clock time) for each case are summarised in Table 2-2.

Table 2-2. Summary of mesh parameters for numerical models

Case	Average Resolution (μm and cells/D)			Cell count	Time Step ($\times 10^{-9}$ S)	CPU (core count)	Wall clock time (hours)
	Sac	Orifice	Spray Chamber				
Coarse	13 (40/**D**)	2 (130/**D**)	6.5 (40/**D**)	4×10^6	$1.6 \leq \Delta T \leq 80$	128	151.4
Medium	7.5 (55/**D**)	1.2 (210/**D**)	5 (50/**D**)	8×10^6	$1.2 \leq \Delta T \leq 60$	256	225.8
Fine	4 (85/**D**)	0.5 (500/**D**)	3.5 (75/**D**)	20×10^6	$0.9 \leq \Delta T \leq 30$	384	565.3

Being aware of the importance of in-nozzle generated turbulence on primary atomisation [48, 75], in the fine case, special consideration was given to generating the mesh inside the nozzle orifice. The size of cells in the orifice were decreased to the order of the Kolmogorov length scale for the liquid phase, η_l, to assure that the smallest generated eddies, as a result of boundary layer and change in cross sectional area, are well resolved. The smallest length scales associated with the flow field for the Quasi-Steady stage of spray are reported in Table 2-3. It can be seen in this table that η_l is much larger than mesh size in the nozzle for the finest grid. To resolve a given length scale it is necessary that $\eta_l \geq 2\Delta x$, where Δx is the grid size [82]. This mesh resolution leads to the proper prediction of small eddies of the liquid phase inside the nozzle orifice in the fine resolution case. A sub-grid scale model is needed for the turbulence in the gas phase.

Table 2-3. Kolmogorov length scales for the liquid and gas phases of the Quasi-Steady stage of spray where the turbulence intensities used are 4.4 % and 10 %, respectively.

Parameter	Value
Liquid phase Kolmogorov length scale, η_{liq}	0.7 μm
Minimum mesh size in nozzle hole for fine case, Δx_{min}	0.1 μm
Gas phase Kolmogorov length scale, η_{gas}	0.1 μm
Minimum mesh size in spray chamber for fine case, Δx_{min}	1.7 μm

2.2.2.4 Mesh sensitivities

In this research structured grids are used to achieve higher quality and control which may be sacrificed in unstructured and hybrid meshes. In addition, the efficiency of the differencing scheme for bounding the convection term of the transport equations in a structured mesh is much higher in comparison to an unstructured mesh [85].

It is possible that the present conically stretched grid leads to greater spray angle than a purely Cartesian/orthogonal grid, for example. The core of the mesh is purely Cartesian/orthogonal, and the divergence immediately adjacent to the core region is less than near the outer boundaries. Using a structured mesh as in the present study reduces the effects of divergence from orthogonality. A non-orthogonality corrector is employed in the numerical solution to minimise any possible grid orientation influences.

2.3 Results and discussions

Due to the unavailability of a transparent orifice, only images of the spray in the chamber are presented. The comparisons between simulations and experiments are qualitative and focus on the overall spray shape, surface irregularities, spray penetration and generated droplets. The numerical data presented in the next two sections are obtained by means of the second-order time derivatives method and the NV Gamma scheme for solving the convection terms.

2.3.1 In-nozzle turbulence

Figure 2-4 illustrates the influence of mesh resolution on turbulent eddies, generated and developed within the orifice boundary layer leading to small/large-scale irregularities. These irregularities are the origin of jet surface instabilities. This Figure shows a zoomed view of the jet turbulent structures inside the nozzle orifice demonstrating the small-scale eddies in each case at the Quasi-Steady stage (sac inlet pressure of 1200 bar and Re of 37000 at the orifice exit). In the left column (images *a*, *c*, and *e*), in-nozzle flow is coloured by velocity magnitude. In the right column at corresponding times (images *b*, *d*, and *f*), the turbulent eddies are depicted using a Q-criterion isosurface of 5×10^{9}, coloured by static pressure. Negative static pressures after the nozzle entrance are due to the absence of a cavitation model. In the high-resolution case, smaller eddies have been resolved demonstrating the importance of mesh resolution on predicting upstream flow conditions.

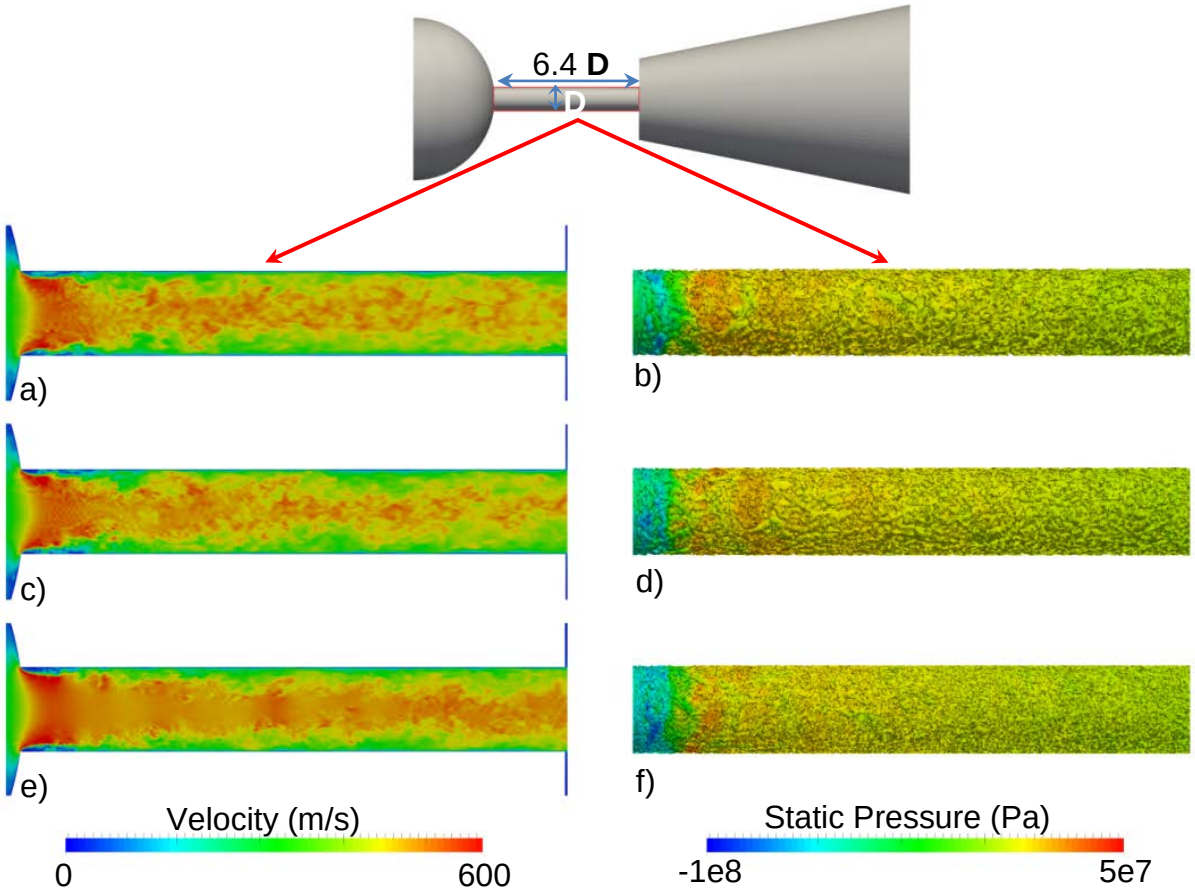

Figure 2-4. Jet liquid turbulent structures at the Quasi-Steady stage (P_{inlet} = 1200 bar and Re = 37000 at the orifice exit for coarse (a and b), medium (c and d) and fine (e and f) mesh cases. In the left column (images a, c, and e), in-nozzle flow is coloured by velocity magnitude. In the right column at corresponding times (images b, d, and f), the turbulent eddies are illustrated using a Q-criterion isosurface of 5×10^9, coloured by static pressure. Negative static pressures after the nozzle entrance are due to the absence of a cavitation model. Greater resolution of jet core and boundary layer turbulence are apparent with increasing mesh density.

2.3.2 Morphology of the penetrating jet

Some instantaneous features such as flow structures and the evolution of spray transients are presented in Figure 2-5 for three different mesh resolutions at 15 μs after start of penetration (ASOP) showing the influence of mesh size on capturing surface instabilities. The umbrella-shaped leading edge of the jet for coarse, medium, and fine cases shows a smooth surface with penetration velocity of 123 m/s in agreement with DNS results [47, 68] for similar velocity ranges.

The irregularities on the trailing edge of the umbrella play a significant role in the disintegration process of the penetrating jet. As can be seen in Figure 2-5, finer grids lead to capturing more waves resulting in higher fragmentation rates.

Mesh resolution affects prediction of instabilities on the liquid jet behind the umbrella. In-nozzle-generated turbulence in combination with relaxation of the velocity profile at the nozzle exit initiate the perturbations leading to wave growth on the jet surface. As can be seen in Figure 2-5, surface instabilities are triggered close to the nozzle orifice exit (further than one diameter for the fine grid) as a result of the K-H mechanism (wave generation on jet surface based on aerodynamic interaction, creating ligaments which then either disintegrate to produce droplets or just roll up and continue to develop).

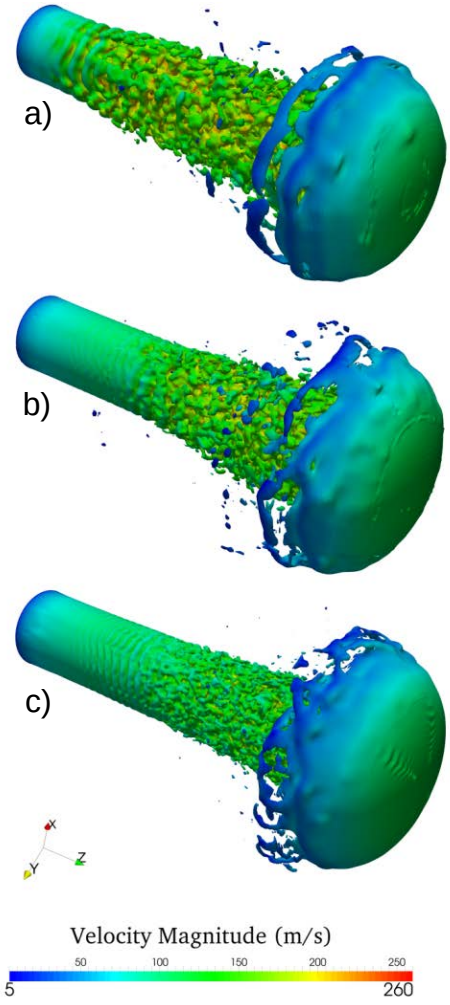

Figure 2-5. Structure of the jet coloured by velocity magnitude at 15 μs ASOP, indicated by liquid interface of γ = 0.5, for coarse (a), medium (b) and fine (c) mesh cases showing over-prediction of breakup for the coarse case and the resolution of smaller scale surface instabilities and breakup for the finer case.

Inaccurate prediction of the velocity relaxation at the liquid-gas interface due to insufficient grid resolution intensifies the K-H mechanism, exaggerating the liquid jet disintegration process. Furthermore, the thickness of ligaments is a matter of the cell size where the pinching-off occurs as the thickness drops below the cell size, followed by the generation of several droplets of varying sizes [25, 86, 87]. It can be concluded that the mesh density at the air-fuel interface considerably influences the development of ligaments and the breakup process. Figure 2-6 shows a comparison of experimental images with the numerical results with the fine mesh case at different times ASOP. Adding a 2× Barlow lens to the microscope to give a total magnification of 7.7:1 enables greater details of the early spray to be captured. The use of a dual frame CCD camera with a time interval of one microsecond between subsequent images allows validation of the velocity of advance of the leading edge and tracking of the transient changes in the morphology of the penetrating diesel jet.

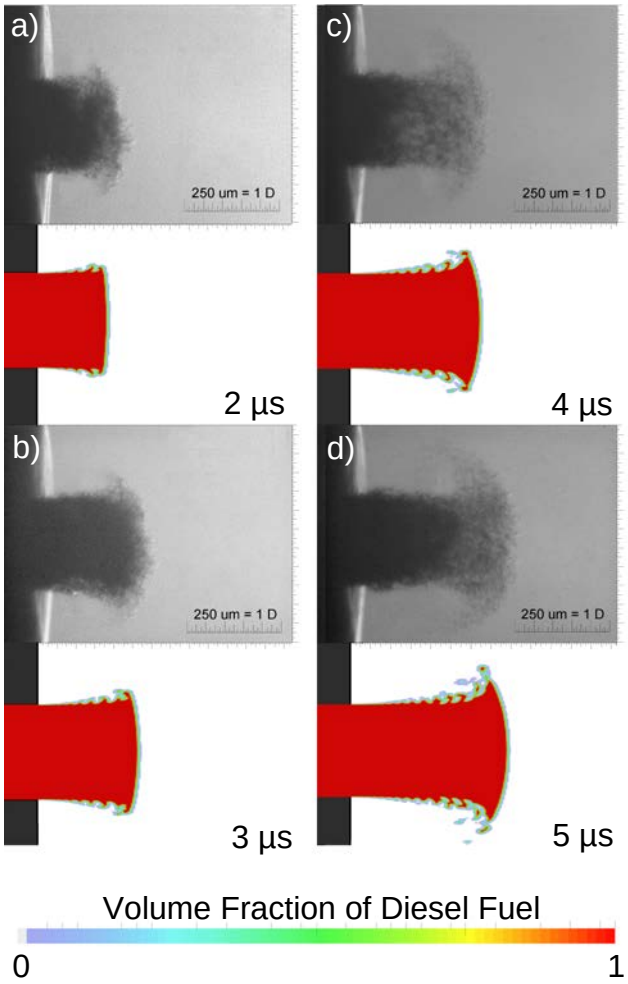

Figure 2-6. Comparison of experimental images with numerical results for the fine mesh case with the highest magnification. Each experimental image is from a different injection event, apart from the first two (a and b) which are captured from two consecutive frames with 1 µs inter frame time.

Some transparency can be clearly seen in the shadowgraphy images. This is due to air inclusion within the liquid inside the orifice, left from the previous injection. The existence of ingested air inside the injector was reported by Swantek et al. [12] at the end of injection (EOI) process. Air inclusion inside the injector influences the spray structure and could be a source of observed deviation between experimental and numerical results.

Shadowgraphy images are compared with the numerical results in Figure 2-7 with a larger field of view, presenting the general structure of the diesel spray. In this Figure, images *a* and *b*, *d* and *e*, *g* and *h*, *i* and *j* are paired, each pair is captured from the same injection event with one microsecond delay between consecutive frames.

The experimental images illustrate a more structured surface even very close to the nozzle exit compared with the numerical results. The leading edge of the emerging jet is disintegrating unlike the numerical results where the leading edge umbrella-shaped structure of the emerging jet is continuous liquid with breakup occurring more rapidly around the periphery. Air inclusion prior to start of injection could explain the rougher surface, and earlier disintegration of the leading edge in the experimental images resulting in the more oblique angle of the umbrella.

The necking of the jet length behind the umbrella can be obviously seen in the experimental images in Figure 2-7, while it is not as marked in the simulations. The difference is possibly related to the presence of air in the experimental jet, as indicated by partial transparency of the experimental images, and thus more rapid disintegration. The outer recirculating gas flow removes the generated droplets and advects them toward the outer flow which can be seen in images *i* and *j* of Figure 2-7.

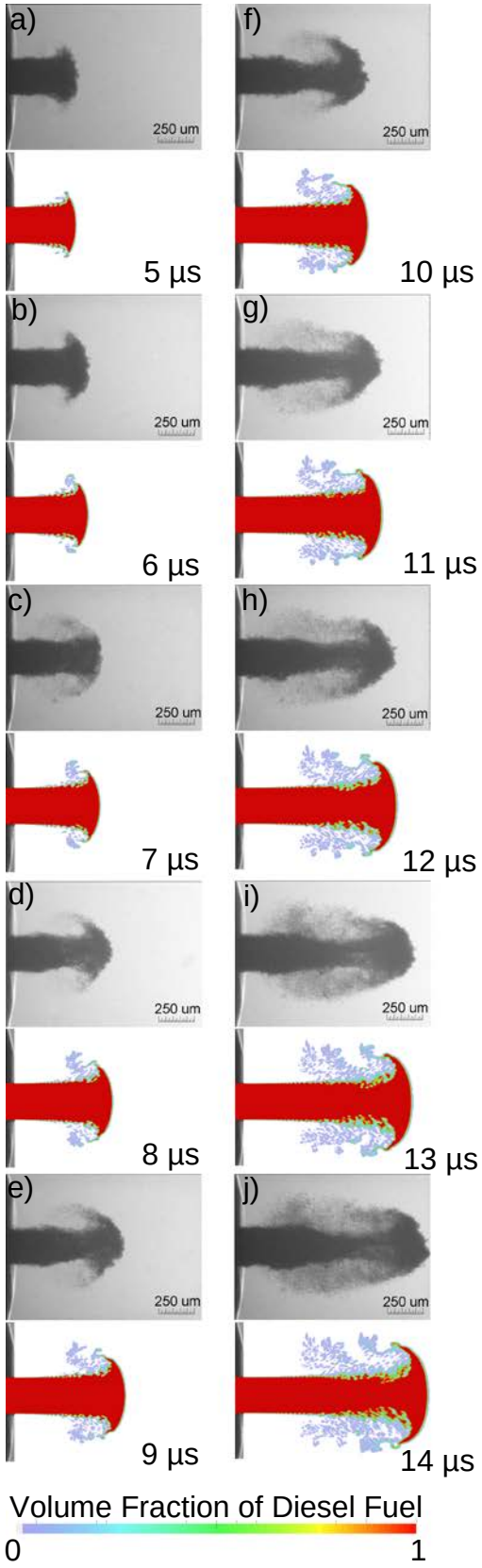

Figure 2-7. Comparison of experimental (with no magnification) and numerical results. Numerical results shown are for the fine mesh, coloured by the volume fraction of diesel fuel. Images a and b, d and e, g and h, i and j are paired, captured from the same injection event from two consecutive frames with 1 µs inter frame time.

Further differences between the experimental and numerical results are in the production of small droplets in the experimental images but not in the numerical results. This is due to the constraint in computational resources where the grid resolution in the computational domain is insufficient to resolve the small eddies in the air phase which influences the breakup processes of the ligaments and droplets.

Capturing two subsequent images enables velocity measurement of the jet leading edge. Experimental values for 100 double frame shots, with inter-frame times varying between 1 to 15 μs are shown in Figure 2-8. The error bars are based on the accuracy of the detection of the leading edge of the jet and this is a function of the inter-frame time. The jet penetration velocity at various axial distances from nozzle exit with corresponding time ASOP, demonstrated in Figure 2-8, show good agreement between numerical and experimental results. The Re is based on the average axial velocity at the nozzle exit.

Instantaneous mass flow rate was not measured. The Quasi-Steady mass flow rate was measured at 0.0139 kg/s and numerically predicted at 0.0168 kg/s. The difference is assumed to be due primarily to the absence of cavitation in the simulations.

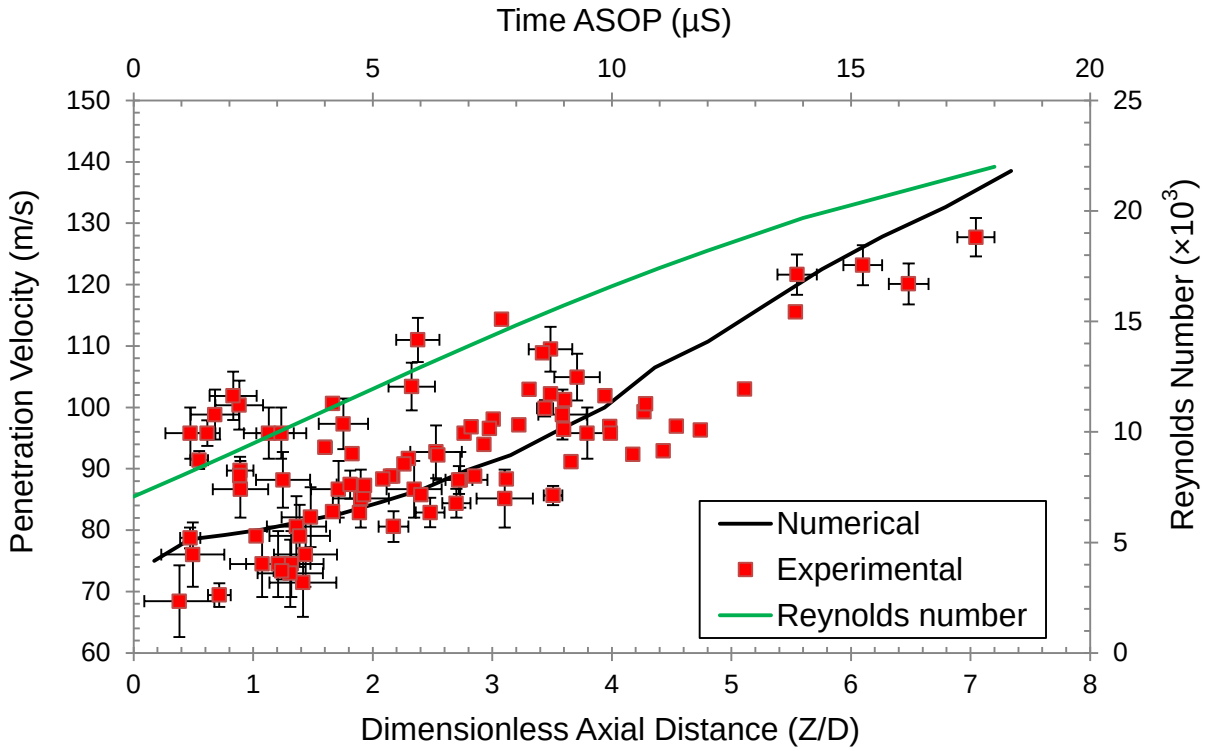

Figure 2-8. Comparison of measured and predicted jet penetration velocity at various axial distances from nozzle exit with corresponding times ASOP. Re values, from computation, are calculated using the average velocity of liquid at the nozzle exit.

2.3.3 Numerical schemes

The behaviour of different interpolation schemes is presented in Figure 2-9, Figure 2-10, and Figure 2-11. The order of the temporal integration schemes for phase-fraction and governing conservation equations plays a significant role in prediction of small-scale eddies inside the nozzle orifice. As depicted in Figure 2-9, at the Quasi-Steady stage, employing the second-order scheme named *Backward* results in smaller scale eddies in comparison to the first-order, *Euler*, approach due to higher dissipation in the first-order scheme. This influences irregularities which are mainly generated by the reduction of the cross-sectional area at the nozzle inlet where there is strong change in flow direction, and vena contracta phenomena [88].

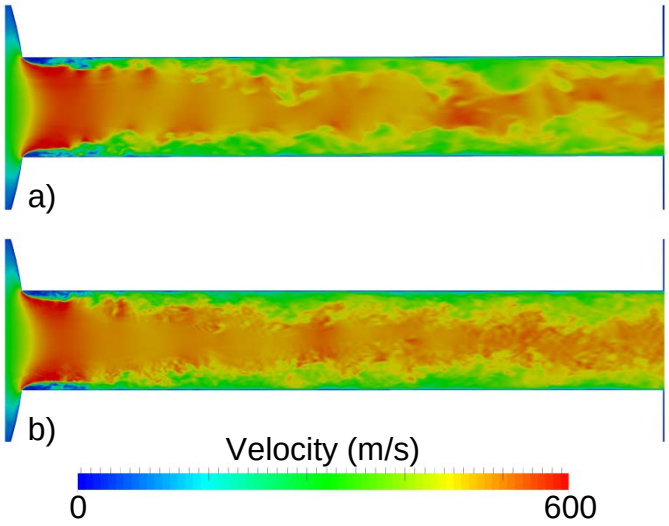

Figure 2-9. Influence of the time derivative order on the prediction of turbulent structures within the nozzle orifice at the Quasi-Steady stage (P_{inlet} = 1200 bar), coloured by velocity magnitude, for the fine grid case with; a) Euler, first-order and b) Backward, second-order.

The first-order discrete equations are more diffusive than the second-order discrete equations [82].The impact of the time interpolation method is also seen in Figure 2-10, at 14 μs ASOP. The disintegration of droplets from the liquid jet surface behind the leading edge diminishes with the first-order scheme compared with the second-order scheme. The second-order accurate interpolation scheme enables modelling of smaller fluctuations of velocity in the liquid-gas interface. Therefore, the K-H waves intensify behind the umbrella-shaped leading edge resulting in higher rates of separation. This separation narrows the liquid jet, demonstrating the necking phenomena of the spray. This necking process is weakened in the first-order interpolation scheme due to higher dissipation (in-efficiency in resolving smaller eddies) in this

method. This is why the second-order scheme for time derivatives has been employed for the present study.

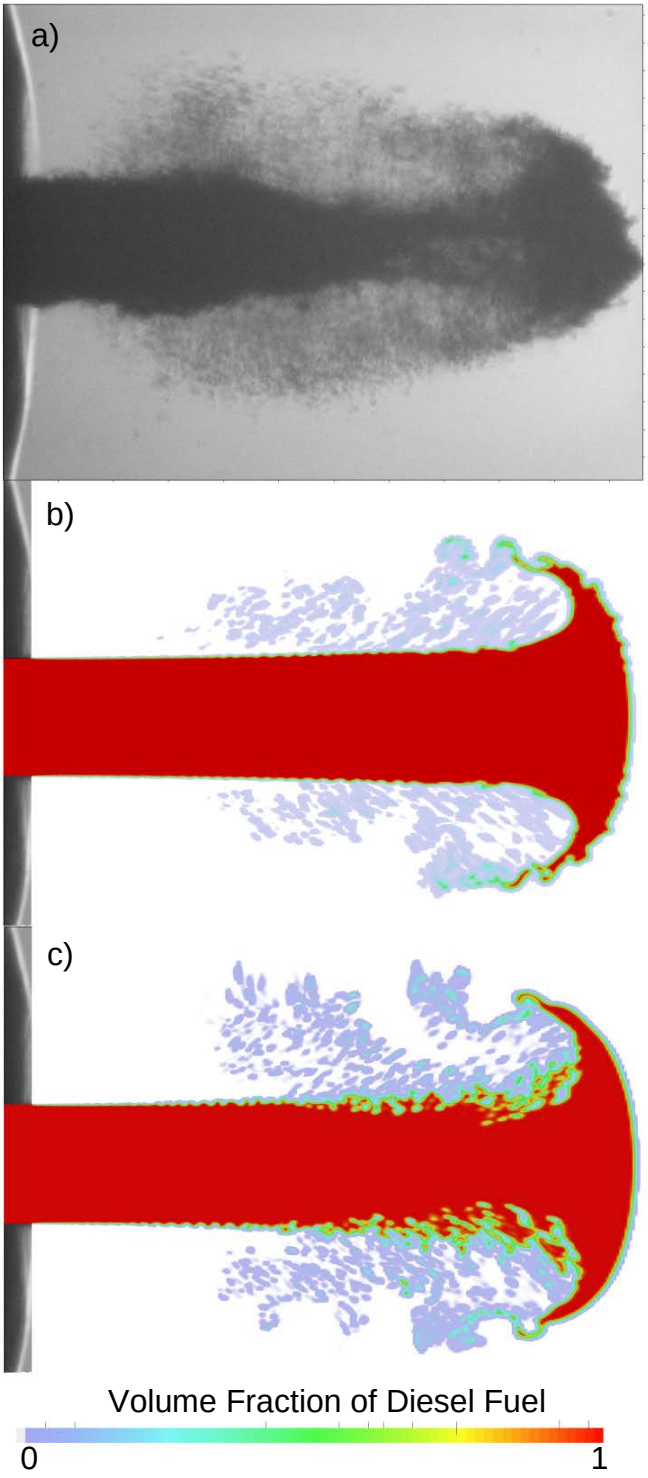

Figure 2-10. Comparison of an experimental image with numerical results showing the effect of the order of temporal integration scheme on the jet disintegration process at t = 14 μs ASOP, coloured by volume fraction of diesel fuel, for the fine resolution case; a) Experiment, b) First-order, and c) Second-order.

The influence of the convection-specific interpolation scheme on capturing the liquid-gas interface is illustrated qualitatively in Figure 2-11 for medium grid resolution. Different ranges of first/second order bounded numerical schemes have been investigated from the more dissipative, Total Variation Diminishing (TVD), up to the more conservative NV schemes. The NV Gamma scheme showed a smooth leading edge surface which is in agreement with DNS results of [47, 68] at a similar penetration velocity. Thus, the NV Gamma scheme has been selected for solving the convection terms. The presence of air in the liquid could play a role in the generation of surface roughness on the leading edge of the experimental jet which is not seen in the simulations.

Secondary interfacial instabilities known as Rayleigh-Taylor (R-T) instabilities may develop when the propagation velocity is sufficient to exceed a critical value. If R-T instability develops, it presents as a rapid crosswise modulation on the leading edge followed by shedding of drops [72]. These interfacial instabilities grow as the jet proceeds downstream and increase gas penetration into the core liquid. The latter forms 'blobs' joined by thin core ligaments. These blobs finally snap and complete the core breakup process. The simulations capture an umbrella-shaped leading edge which qualitatively is in agreement with the experimental results as shown in Figure 2-6 and Figure 2-7, although no spanwise instabilities due to the R-T mechanism are apparent with the NV Gamma scheme. Figure 2-11 demonstrates that certain convection interpolation schemes may give apparent or R-T like instabilities which are not necessarily physical.

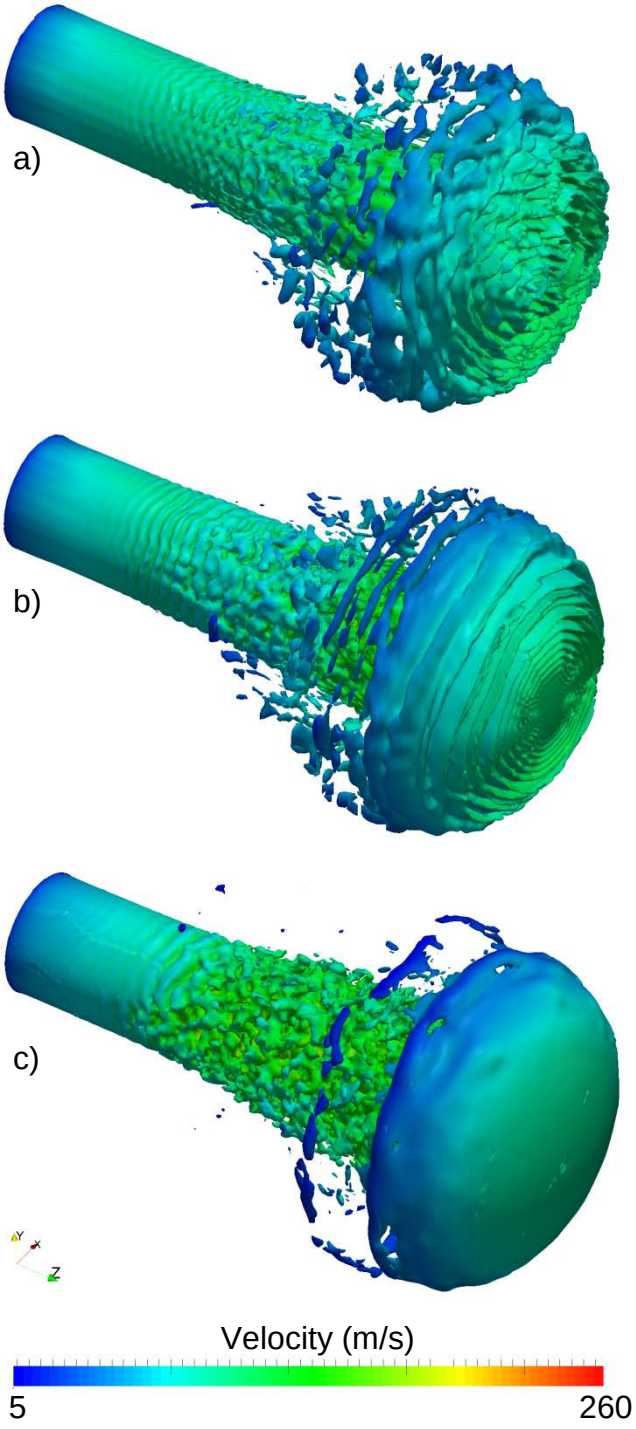

Figure 2-11. The effect of convection-specific interpolation schemes on capturing surface instabilities of the jet beyond the nozzle exit for the medium resolution grid at t = 14 μs ASOP, indicated by volume fraction of γ = 0.5, and coloured by velocity magnitude; a) TVD, FilteredLinear, b) TVD, LimitedLinear, and c) NV, Gamma

2.3.4 Spray structure at the Quasi-Steady stage

The atomised liquid fraction on the spray surface for the three mesh resolutions is illustrated in Figure 2-12 by $\gamma = 0.1$ isosurface, coloured by the velocity magnitude at the Quasi-Steady stage where diesel fuel pressure at sac inlet is 1200 bar. The onset of primary atomisation can be seen close to the nozzle exit for the three mesh resolutions. Very fine droplets are captured near the nozzle exit noticeably in the finest case (20 million cells) which agrees with the experimental images. The surface velocity decelerates rapidly close to the orifice exit due to relaxation of the velocity profile. The number of discrete droplets captured for the coarse, medium and fine meshes at the Quasi-Steady stage are 4830, 9494, and 22076 respectively. The increase in apparent atomisation from finer meshes is due to better prediction of the smaller-scale in-nozzle turbulent structures as presented in Figure 2-12, resulting in smaller-scale surface eddies which intensify the breakup process. Consequently, the breakup rate increases in cases with higher mesh resolution. The atomisation rate at the Quasi-Steady stage is 0.0139, 0.0148, and 0.0158 kg/s for coarse, medium and fine mesh, respectively. The finer the mesh, the finer the resolved droplets. Mesh independence is not demonstrated due to limited computer resources and unfeasible computation time.

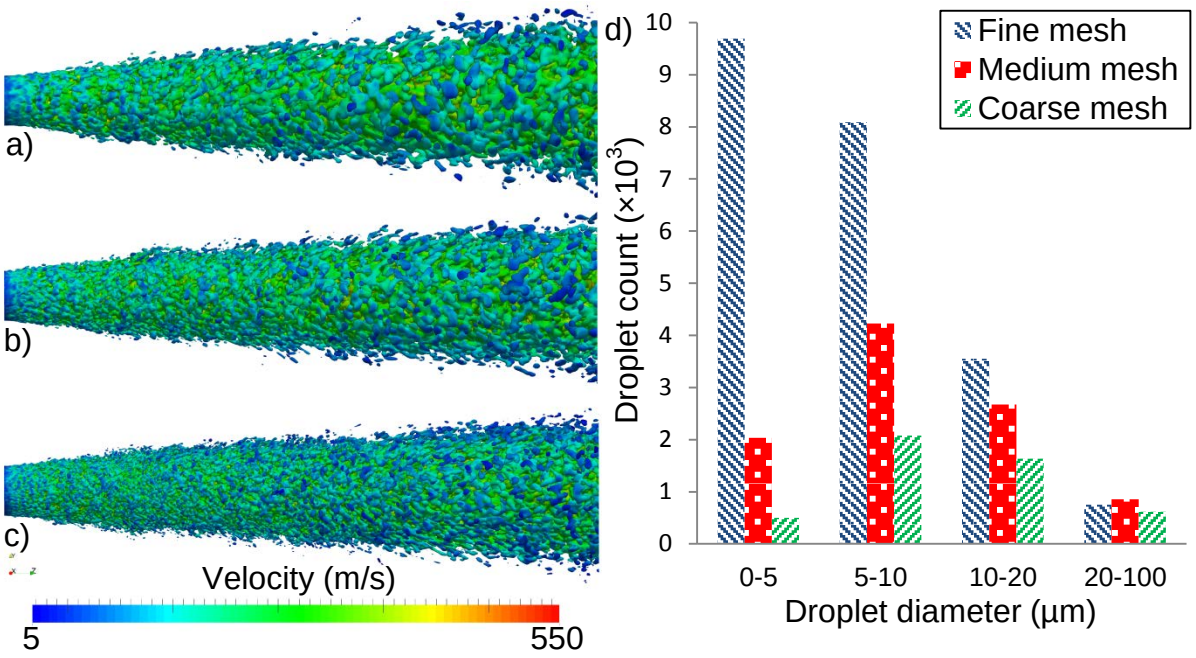

Figure 2-12. Spray morphology within 12 nozzle diameters of the nozzle exit, indicated by isosurface of volume fraction $\gamma = 0.1$, coloured by velocity magnitude at the Quasi-Steady stage (P_{inlet} = 1200 bar); a) Coarse, b) Medium and c) Fine case showing decreasing scale of surface features with increasing mesh resolution. Panel d) shows quantitatively the greater number of fine droplets generated with finer meshes.

The mass distribution of droplets at various axial distances at the Quasi-Steady stage for all three cases is depicted in Figure 2-13. The cumulative mass of droplets follows expected trend as this value is very small in the first nozzle diameter from the nozzle exit, then increases smoothly up to almost 7 nozzle diameter due the slow rate of droplets generation stripping from the liquid core surface. The atomised mass increases rapidly further downstream mainly due the completion of liquid core fragmentation, droplets shedding, and the disintegration of ligaments generated at the trail of the jet leading edge. The trend of spatial mass distribution of droplets for all mesh cases shows same behaviour, giving some degree of confidence in the applied methodology.

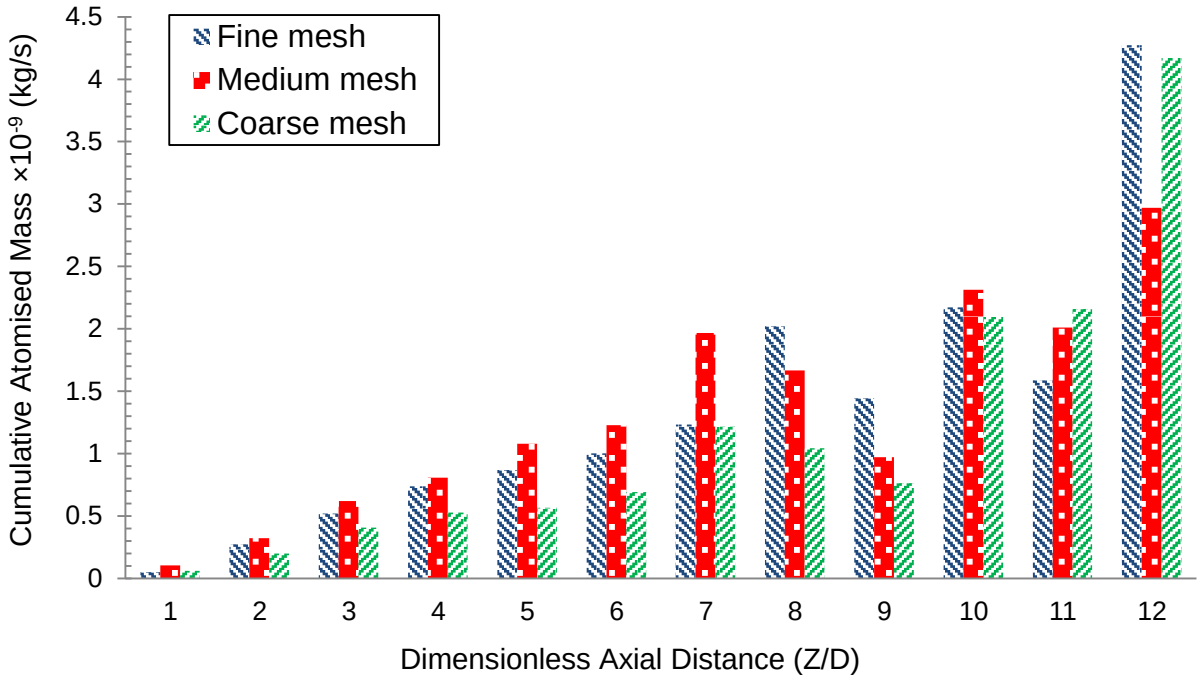

Figure 2-13. Cumulative mass distribution of droplets along the axial distance from the nozzle exit for three mesh resolutions at the Quasi-Steady stage of injection. The value of total atomised mass is very small at the close region to the nozzle exit, accelerates slowly up to 7**D** and then increases more rapidly further downstream.

Figure 2-14 illustrates a close-up view of the jet disintegration, visualised using the isosurface of $\gamma = 0.5$ for the fine mesh case, at the Quasi-Steady stage. This picture represents the jet surface detachment and droplet generation, occurring even at one nozzle diameter downstream.

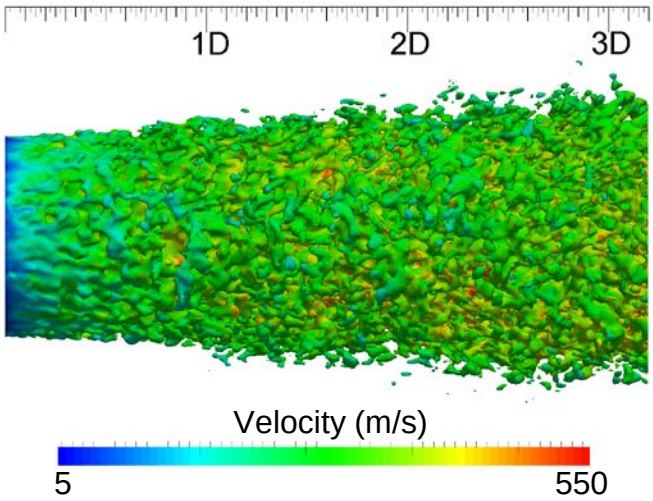

Figure 2-14. Close-up view showing the onset of surface breakup visualised by isosurface of $\gamma = 0.5$ coloured by velocity for the fine mesh case at the Quasi-Steady stage (P_{inlet} = 1200 bar).

The growth of non-axisymmetric disintegration at different cross-sections from the nozzle exit is presented in Figure 2-15. The formation of small longitudinal waves can be seen at one nozzle diameter downstream of the nozzle exit. At one diameter downstream primary breakup is triggered and intensifies farther downstream. Up to 5 diameters from nozzle exit, the core breakup process is fully developed since the liquid core is narrowing to tapered ligaments. The liquid core is totally disintegrated at 8 diameters downstream, resulting in higher numbers of droplets than at the positions upstream.

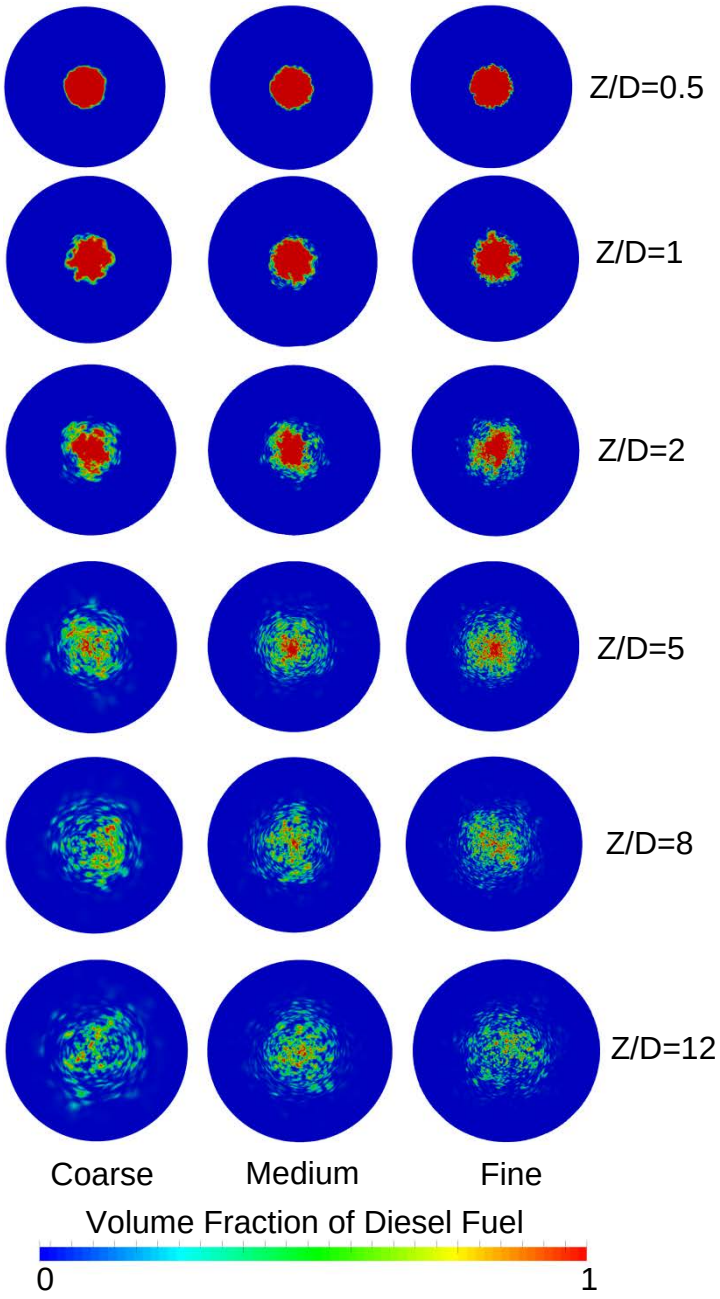

Figure 2-15. Liquid distribution in cross-sectional planes at different streamwise positions downstream of the nozzle exit for the coarse (left column), medium (middle column) and fine (right column) cases at the Quasi-Steady stage (P_{inlet} = 1200 bar).). The value of z/D indicates the number of nozzle diameters downstream of the nozzle exit.

Figure 2-16 illustrates the liquid core visualised using the $\gamma = 0.95$ isosurface at the Quasi-Steady stage (P_{inlet} = 1200 bar) for different meshes. It can be seen that longitudinal surface perturbations develop near the nozzle exit. The liquid core tapers progressively before disintegrating into large clusters which is in accordance with the limited available data by [89]. The fine mesh case shows an extended liquid core compared to the coarser cases. This is due to

pinching-off of smaller droplets from thinner ligaments detached from the liquid jet surface which slows down the liquid core disintegration process [25, 86, 87].

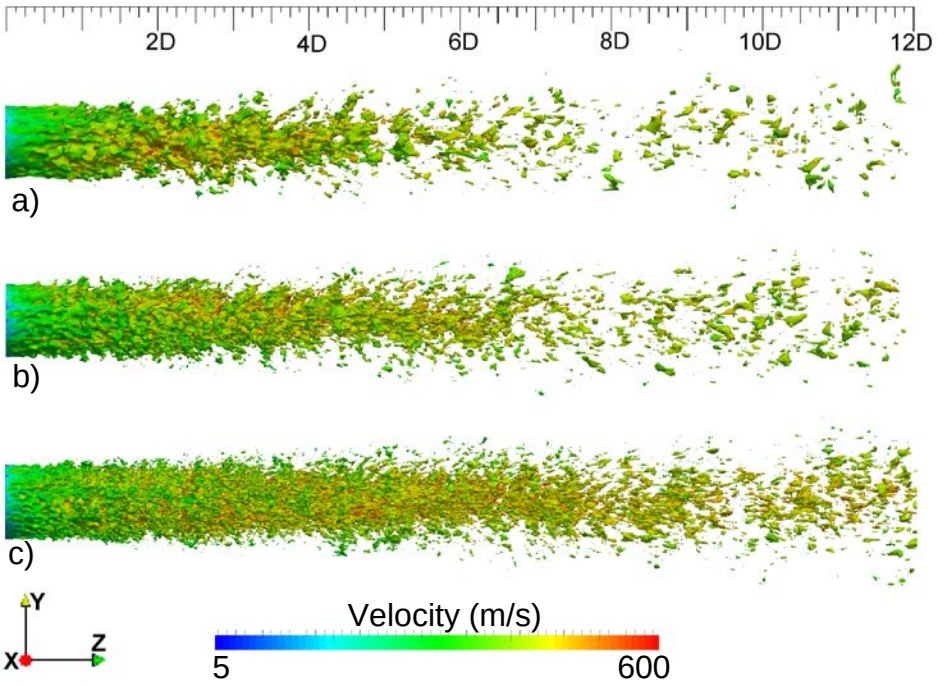

Figure 2-16. Effect of mesh resolution on jet liquid core length depicted by γ= 0.95 isosurface for a) Coarse, b) Medium and c) Fine mesh cases at the Quasi-Steady stage (P_{inlet} = 1200 bar).

Figure 2-17 depicts the early spray angle (ϕ) at the Quasi-Steady stage, measured on a spray image using edge detection based on a threshold filter. The formation and development of shear layer instabilities can be clearly seen. The nozzle tip is apparent on the left side of the image.

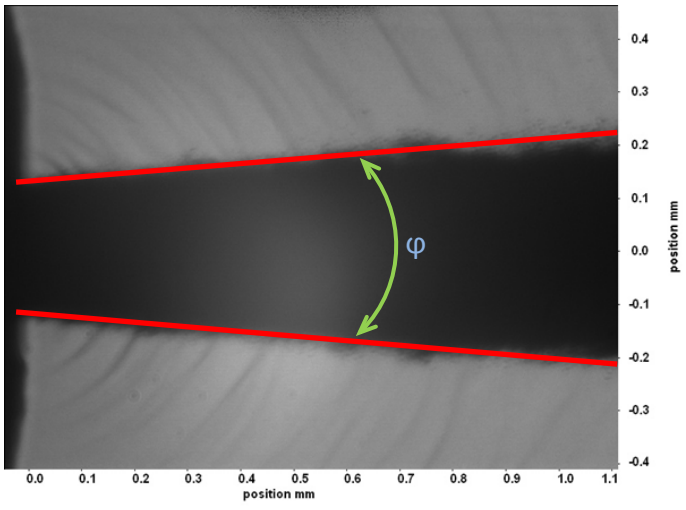

Figure 2-17. Shadowgraphy of the diesel nozzle spray at the Quasi-Steady stage (P_{inlet} = 1200 bar), using long distance microscope[84].

To compare the predicted numerical early spray angle with experiment, Leboissetier & Zaleski [90] core analysis was conducted. Based on this method, three different zones in the numerical data were distinguished at every time step during the Quasi-Steady stage. The results of this analysis for three different cases are depicted in Figure 2-18, showing the time-averaged structure of the atomisation region. The red zone contains only liquid (never contains gas), thus representing the liquid core; the blue region is gas only while the green region contains sporadic liquid and gas volumes depicting the atomisation zone. The early spray angle was extracted using the outer boundary of the two phase mixture (green) zone.

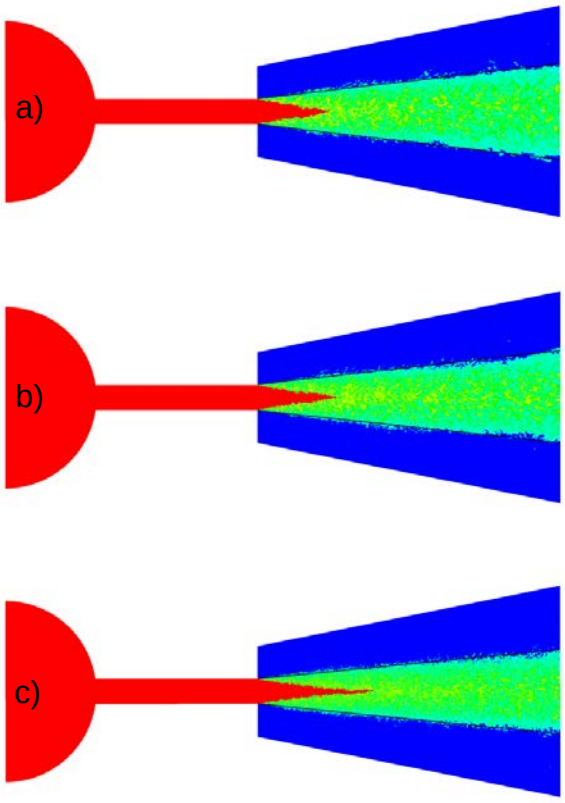

Figure 2-18. A Leboissetier & Zaleski [90] core analysis for, a) Corase, b) Medium, and c) Fine at the Quasi-Steady stage, P_{inlet}=1200 bar; red and blue region experienced only liquid and gas, respectively. The green zone is the atomisation region.

A summary of this investigation, gathered using these plots (Figure 2-18) is tabulated in Table 2-4, showing the reduction in spray angle and increase in liquid core length for the higher mesh resolution cases. For comparison, the core length predicted by Hiroyasu and Arai's correlation [74] is also shown. The predicted core length appears to be too small and this may be partly due to the methods used to determine core length and partly due to the absence of a cavitation model, and thus overly high jet turbulence.

Table 2-4. Comparison of spray angle and liquid core length

Case	Early Spray Angle	Core Length (mm)	Core Length (D)
Experiment	8.7 ± 0.4°	-	-
Coarse	13.22 ± 1°	0.71 ± 0.05	2.84 **D**
Medium	12.52 ± 0.8°	0.73 ± 0.05	2.92 **D**
Fine	11.26 ± 0.5°	1.151 ± 0.02	4.6 **D**
Hiroyasu & Arai [74]	-	9.13	36.5 **D**

2.4 Conclusions

The general structure of primary atomisation of diesel sprays was successfully characterised numerically employing an Eulerian/LES/VOF approach to capture free surfaces. The umbrella-shaped leading edge of the emerging jet was captured successfully near the nozzle exit. The experimental shadowgraphy images showed a rougher surface, greater transparency, more oblique angle and earlier disintegration of the leading edge in comparison with the numerical prediction. This is presumed due to in-nozzle air inclusions left from the previous injection event. The necking of the liquid jet behind the umbrella-shaped leading edge is captured in both experimental and numerical results. The temporal variation of jet penetration velocity and Reynolds number show favourable agreement between numerical and experimental results. The second-order temporal integration scheme and NV Gamma convection-specific interpolation scheme resulted in a better prediction of small scale eddies and jet surface structures compared with the first-order integration scheme and TVD convection-specific interpolation schemes.

A mesh resolution study for the two stages of the spray, initial penetration and Quasi-Steady, revealed that:

- fragmentation of the jet commenced close to nozzle exit (within about one diameter from exit) for the finest mesh
- modelling of the primary breakup process is enhanced with higher mesh resolution
- droplet sizes decrease with increasing mesh resolution
- smaller eddies were captured with decreasing cell size inside the nozzle
- increasing mesh resolution leads to decrease in the early spray angle and increase in the liquid core length, leading to better agreement between experiment and numerical predictions.

2.5 Acknowledgments

This work was supported by the Australian Maritime College and the Defence Science and Technology Group. The authors express their gratitude to colleagues Luciano Mason, Jalal Rafie Shahraki for their support and suggestions. The authors also express gratitude to Hongjiang Yu for his assistance with the analysis of drop sizes.

Chapter 3 :

Analysis of Diesel Spray Dynamics Using a Compressible Eulerian/VOF/LES Model and Microscopic Shadowgraphy

This chapter has been submitted to the journal "Fuel" and at the time of writing is under review. This chapter has been modified to eliminate the repetition. The citation for the research article is:

M. Ghiji, L. Goldsworthy, V. Garaniya, P.A. Brandner, and P. Hield. Analysis of Diesel Spray Dynamics Using a Compressible Eulerian/VOF/LES Model and Microscopic Shadowgraphy, *Fuel*, Volume 188, 15 Jan 2017, Pages 352-366 (http://dx.doi.org/10.1016/j.fuel.2016.10.041).

Abstract

This paper presents numerical and experimental analysis of diesel engine spray dynamics in the region very close to the nozzle exit. Diesel fuel is injected through a single solid cone injector with sharp-edged nozzle inlet. Numerical investigations are conducted in an Eulerian framework by applying a Volume of Fluid interface capturing technique integrated with Large-Eddy Simulation turbulence modelling. Cavitation is modelled, by allowing liquid fuel to flash to gas at the fuel vapour pressure. The computational domain and settings mimic the experimental injector internal geometry and experimental operating conditions. In-nozzle disturbances are qualitatively well modelled by implementing the no-slip condition at the injector walls as well as cavitation and compressibility effects for each phase. A mesh dependency study is conducted with four different grid resolutions. Data are presented around the start of penetration (SOP) and up to the time when shock waves at the gas-liquid interface are well developed, the quasi-steady stage of injection. At SOP, an umbrella-shaped leading edge is captured in both the numerical and experimental studies however only the experimental images demonstrated a semi-transparent cloud of air-fuel mixture at the leading edge. A previously undescribed toroidal starting vortex near the nozzle exit is captured experimentally and numerically. Development of cavitation, down to the end of nozzle hole leads to the detachment of liquid from the nozzle hole walls and subsequently the diminution of boundary layer effects and thus reduced in-nozzle turbulence, and increased liquid jet velocity.

3.1 Introduction

Engine emissions are produced during the combustion process which is fundamentally controlled by the dynamics of the fuel injection [24, 36, 74, 91-93]. There is a wide range of fuel injectors based on their shapes and flow characteristics but the purpose of most injectors is still the same, to induce atomisation, penetration, turbulence generation and gas-fuel mixing. Undoubtedly, a clear understanding of these processes would assist engineers to design an injector which not only meets strict pollution requirements but also improve engine performance in one of the most extreme environments for multiphase flow. In this harsh environment, shock waves [11] and turbulent eddies [67] are expected, which makes understanding of the spray dynamics a challenge for designers and scientists.

The atomisation process which initiates very close to the nozzle hole exit, is called primary atomisation and controls the extension of the liquid core and subsequently the secondary atomisation in the disperse flow region [7, 33]. To date, many theories have been proposed to describe the primary atomisation mechanism, including: Aerodynamic shear forces which act through stripping and Kelvin-Helmholtz (K-H) instabilities [8, 25, 75]; Turbulence-induced disintegration which has a significant effect on jet breakup in higher Reynolds number $Re_l = \varrho_l V D / \mu_l$, where ϱ_l is the liquid density, V is the liquid velocity, D is the orifice diameter, and μ_l is the liquid dynamic viscosity [19, 48, 49, 51]; Relaxation of the velocity profile, creating a "bursting" effect especially in non-cavitating jets and large velocity differentials [52]; Cavitation-induced disintegration of the jet due to the reduction of cross-section area at nozzle inlet [40-42, 46]; and liquid bulk oscillation provoking the toroidal surface perturbation [25, 54].

For nozzles with small length-to-diameter ratios super-cavitation and hydraulic flip can occur [39]. In these cases, the liquid fuel which has detached at the nozzle inlet remains detached from the walls throughout the entire nozzle passage, and the liquid core is contracted at the nozzle exit compared to the nozzle size, so the mass flow rate is reduced. If the length of the nozzle passage is long enough, or if the injection pressure is not high, the liquid flow can re-attach to the walls downstream of the nozzle hole inlet [45, 70]. In this case, the discharge coefficient is higher compared to that of the super-cavitation case.

Based on the Reynolds and Ohnesorge numbers of the flow, the breakup of liquid jets is categorised into four regimes; Rayleigh breakup, first wind-induced breakup, second wind-induced breakup, and atomisation [94]. These parameters also change with different fuels. Detailed studies comparing different fuels and the influence on spray structure and formation

have been made by Payri et.al [95, 96], Desantes et.al [97], Battistoni et.al [98], and Goldsworthy et.al [84]. For diesel propulsion systems, the liquid propellants fall well within the atomisation regime. In such regime, average drop diameters are much less than the jet diameter, thus indicating that the scale in which flow instabilities arise is much smaller than the jet diameter. Furthermore, liquid jets within this regime experience stronger axial velocity gradients in the near exit region than the jets in other regimes due to faster relaxation of the liquid surface as it transitions from a no-slip boundary (except in the case of "super-cavitation") to a free surface boundary condition as it exits the injector nozzle.

The existence of shock waves in high pressure diesel spray was first reported by Nakahira et al. [99] and most recently by Huang et al. [11] using the schlieren image technique. Hillamo et al [100] demonstrated the imaging of shock waves from a diesel spray using the backlit imaging technique. An increase of 15% in the gaseous phase density near the shock front was quantitatively demonstrated by MacPhee et al. [18] using the X-ray radiograph image technique.

In experimentations, isolating and quantifying the various interactive mechanisms involved in primary atomisation of a high-pressure liquid jet are very difficult [15, 21, 71, 73, 75, 101]. Hence, numerical analysis can be employed to get a clearer insight into the effect of each parameter at different stages of the injection process [92, 102].

Generated turbulent flows can be represented by eddies with a range of length and time scales. Large eddy simulation (LES) directly resolves large scale eddies and models small eddies, allowing the use of much coarser meshes and longer time steps in LES compared to Direct Numerical Simulation (DNS). LES needs principally finer meshes compared to the ones used for Reynolds Averaged Navier-Stokes (RANS) computations. Since RANS models cannot capture features of the transient spray structure [2, 4, 25, 33] such as droplet clustering and shot to shot variability, LES is applied to overcome these limitations. In addition, the conventional atomisation models with Lagrangian Particle Tracking (LPT) limit the grid fineness near the nozzle and do not allow LES to capture the features of the spray and background fluid flow near the nozzle. Refining the grid with the blob atomisation method can result in problems with a high liquid fraction in the LPT approach (too much liquid in each cell) [2, 4, 33, 68]. These limitations motivate the use of the Eulerian approach to model the primary atomisation, instead of using LPT atomisation models. With ever increasing computational power there is an incentive to use more complex models for primary atomisation.

The accuracy of different numerical techniques for modelling the primary atomisation of a liquid diesel jet was investigated in detail for low Re ($Re < 5000$) by Herrmann [48] and Desjardins & Pitsch [78]. Herrman [48] demonstrated the importance of the grid resolution on capturing the accurate phase interface geometry of diesel liquid with an injection velocity of 100 m/s and $Re = 5000$. Turbulence was reported as the dominant driving mechanism of atomisation within the first 20 nozzle diameters downstream.

The present study focuses on experimental and numerical investigation of the primary atomisation in the early stages of injection with increasing injection pressure up to 1200 bar, background pressure of 30 bar, liquid Re of $7\times10^3 \leq Re_l \leq 46\times10^3$, and liquid Weber number of $4\times10^4 \leq We_l \leq 2\times10^6$. The liquid Weber number (We_l) is defined as $\rho_l V D / \sigma$, where σ is the surface tension at the liquid-gas interface. Recent work using X-ray imaging [10, 12, 13], especially from the Argonne Laboratory has greatly enhanced our understanding of diesel spray dynamics. The experimental techniques presented here, while less sophisticated are more accessible and give useful data on the spray morphology for comparison with numerical analysis.

A key aim of the present work is to achieve a valid (high-fidelity) Computational Fluid Dynamics (CFD) modelling of diesel spray primary atomisation which can be applied by engine developers for improved design of diesel engines. A further aim is to apply the numerical and experimental analysis to enhance understanding of in- and near-nozzle processes.

3.2 Methodology

Experimental measurements are used to validate the numerical results at various stages of the injection event. The experiments employed a microscopic laser-based backlight imaging (shadowgraphy) technique using a constant volume spray chamber.

Numerical investigations are conducted by applying the VOF phase-fraction interface capturing technique in an Eulerian LES framework where cavitation of the fuel is allowed at a predefined vapour pressure. Enhanced cavitation inception due to nuclei is not modelled. The effects of compressibility of each phase have been included in the numerical model, enabling the investigation of more complex physics associated with a diesel spray process such as viscosity and temperature changes, generation and development of cavitation and gaseous shock waves.

3.2.1 Experimental Set-up

The experimental apparatus consists of a constant volume High-Pressure Spray Chamber (HPSC). The HPSC operating volume is a square-section prism with rounded corners, with the chamber and spray axes vertically oriented. Optical access to the chamber is via three windows of UV quality, optically polished quartz, with viewing area of 200 × 70 mm. The chamber pressure can be varied to emulate the air density occurring in a diesel engine at the start of injection. Diesel fuel is injected axially through a single solid cone fuel spray with an adjustable injection pressure up to 1200 bar from the top of HPSC as shown in Figure 2-1. A continuous flow of air through the chamber removes droplets from previous shots. Tests were made to ensure that any turbulence induced by the flushing air did not impact on the spray dynamics, by closing off the flushing air flow and observing if this impacted on the spray morphology.

The injection pressure profile is highly repeatable from shot to shot. The injector needle valve snaps open when the injector pressure achieves a certain value, as determined by the adjustable tension on the needle valve spring. The needle lift is monitored using an eddy current proximity probe. The needle lift transducer indicates that it takes about 200 μs for the needle valve to lift completely. The maximum needle lift is nominally 200 μm. The needle lift commences around 100 μs after the start of injection. However, the response of this transducer may not exactly indicate the motion of the needle as the needle lift detector is mounted on the spring actuating rod rather than the needle itself, so compression of the actuating rod could mask the actual needle motion, and there is potentially some lag in the electronics.

A Kistler piezoelectric pressure transducer with a sample rate of 10 MHz monitors the pressure of the fuel supplied to the injector. The high-pressure fuel pulse is generated in a modified Hydraulic Electric Unit Injector (HEUI) as described in Goldsworthy et al. [84, 103]. The ability to independently adjust the needle lift pressure allows relatively high pressures at the point of needle lift, which is more characteristic of common rail injectors than of conventional injectors.

The spray is illuminated with laser light through a standard solid state diffuser supplied by LaVision. The diffuser employs laser-induced fluorescent from an opaque plate impregnated with a fluorescent dye. A 120 mJ dual-cavity Nd:YAG laser is used and in combination with the solid state diffuser, light pulses of duration around 10 ns are achieved. A Questar QM100 long distance microscope is attached to a LaVision Imager Intense dual-frame, 12 bit CCD camera with 1376 × 1040 pixel resolution. The camera is focused, aligned, and calibrated on a graduated

scale on the spray axis. With a 2x Barlow lens, mounted between CCD Camera and Microscope, a magnification of 7.7:1, a field of view of 1157×860 μm and a spatial resolution of 0.84 μm/pixel are achieved.

Data acquisition is initiated at a pre-set threshold of fuel pressure, with an adjustable delay to the acquisition of the images. The camera and laser allow two images with variable time gap as low as 1 μs to be taken for each shot of the injector. The Qswitch signal from the laser indicating that the laser has been fired is acquired in LabVIEW along with the injection pressure and needle lift signal. This indicates the timing of the data acquisition relative to the needle lift and pressure development. The start of penetration is found to be 100 ± 5 μs before the needle lift signal reached 2% of its maximum value. This delay is assumed to be due to compression/buckling of the rod which transmits the spring force to the needle, and electronic delay in the needle lift transducer. The timing jitter of ± 5 μs means that meaningful comparison of numerical and experimental penetration against time could not be made with sufficient precision, so instead the consecutive imaging technique is employed. In this technique, to determine the time from SOP to the taking of the second image, shots are repeated until the first image acquired corresponds to the SOP and thus the pre-set delay to the second image represents the time After Start Of Penetration (ASOP). An interval of about 30 seconds between injector shots allows the gas in the chamber settle.

3.2.2 Numerical Approach

3.2.2.1 Mathematical Method

In this study, the compressible VOF phase-fraction based interface capturing technique is employed in the open source numerical code OpenFOAM v2.3. The governing equations of the solver which is based on *compressibleInterFoam,* consist of the balances of mass (3-1), momentum (2-2) and total energy (3-3) and enthalpy (3-4) for two immiscible, compressible fluids with the inclusion of the surface tension between two phases and the equation of state (3-9). These equations establish a closed system for the variables density ρ, velocity $\boldsymbol{V}$, pressure p, internal energy $\widehat{U}$, and enthalpy $\hat{h}$,

$$\frac{\partial \rho}{\partial t} + \nabla.(\rho \boldsymbol{V}) = 0 \tag{3-1}$$

$$\frac{\partial \rho \boldsymbol{V}}{\partial t} + \nabla.\left(\rho \boldsymbol{V} \otimes \boldsymbol{V}\right) = -\nabla p + \nabla.\tau + \rho \boldsymbol{g} + \int_{S(t)} \sigma \boldsymbol{\kappa} \boldsymbol{n} \delta(x - x') dS \tag{3-2}$$

$$\frac{\partial \rho \widehat{\boldsymbol{U}}}{\partial t} + \nabla.\left(\rho \widehat{\boldsymbol{U}} \boldsymbol{V}\right) + \frac{\partial \rho \boldsymbol{K}}{\partial t} + \nabla.(pK\boldsymbol{V}) + \nabla.(p\boldsymbol{V}) = -\nabla.\mathrm{q} - \nabla.(\tau.\boldsymbol{V}) + \rho \boldsymbol{g}.\boldsymbol{V} \tag{3-3}$$

$$\frac{\partial \rho \hat{h}}{\partial t} + \nabla.\left(\rho \widehat{\boldsymbol{h}} \boldsymbol{V}\right) + \frac{\partial \rho \boldsymbol{K}}{\partial t} + \nabla.(pK\boldsymbol{V}) - \frac{\partial p}{\partial t} = -\nabla.\mathrm{q} - \nabla.(\tau.\boldsymbol{V}) + \rho \boldsymbol{g}.\boldsymbol{V} \tag{3-4}$$

where, μ is the dynamic viscosity, t is the time, $\boldsymbol{g}$ is the gravitational acceleration, σ is the surface tension, K is the kinetic energy, q is the thermal energy flux vector, τ is the viscous stress tensor, κ is the local curvature of the liquid surface and, n denotes a unit vector normal to the liquid surface S. The operators $\nabla(\ )$ and $\nabla.(\ )$ represent the gradient and the divergence operations, respectively.

The momentum source due to surface tension force on the interface $S(t)$, the integral term in equation (3-2), only acts on S and produces a non-zero value when $x = x'$ which is an indication of the existence of an interface. The estimation of this integral term is obtained following De Villier [72] through the continuum surface force model of Brackbill et al. [104] as:

$$\int_{S(t)} \sigma \boldsymbol{\kappa} \boldsymbol{n} \delta(x - x') dS \approx \sigma \boldsymbol{\kappa} \nabla.\gamma \tag{3-5}$$

where γ is the volume fraction of the liquid phase defined as:

$$\gamma = \begin{cases} 1 & \text{for a point inside the liquid} \\ 0 < \gamma < 1 & \text{for a point in the transitional region} \\ 0 & \text{for a point inside the gas} \end{cases} \tag{3-6}$$

The 'transitional region' is where the interface is located, realised as an artefact of the numerical solution process. Fluid in the transition region is considered as a mixture of the two fluids on each side of the interface, which cannot completely resolve a discontinuous step. The volume fraction is obtained from the solution of a transport equation:

$$\frac{\partial \rho \gamma}{\partial t} + \nabla.(\rho \boldsymbol{V} \gamma) = 0 \tag{3-7}$$

The interface curvature, κ, calculated from the solution of liquid phase volume fraction γ is

$$\boldsymbol{\kappa} = \nabla . \left(\frac{\nabla \gamma}{|\nabla \gamma|} \right) \tag{3-8}$$

The system of equations are closed by an equation of state

$$\begin{cases} \rho_l = p\, \psi_l \\ \rho_g = p\, \psi_g \end{cases} \tag{3-9}$$

where $\boldsymbol{\psi}$ is the compressibility and the subscripts l and *g* represent the liquid and gas phases respectively.

The local thermo-physical properties are given by:

$$\rho = \gamma \rho_l + (1 - \gamma) \rho_g \tag{3-10}$$

$$\mu = \gamma \mu_l + (1 - \gamma) \mu_g \tag{3-11}$$

The time-varying phase interface *S(t)* is located using a VOF surface capturing/tracking approach [105] which utilises a "compression velocity" term [80] in equation (3-7) to preserve sharp interfaces.

The LES/VOF equations are derived from equations (3-1), (3-2) and (3-7) using localised volume averaging of the phase-weighted hydrodynamics variables. This process, known as filtering, includes decomposition of the relevant variables into resolvable and sub-grid scales of turbulent fluctuations. As a result of the filtering process, the sub-grid scale fluctuations will be eliminated from the direct simulation. This filtering together with the non-linear convection terms in equation (3-2) introduce an additional quantity which is known as the sub-grid scale (SGS) stresses τ^{sgs}. The SGS stresses comprise correlation of the variable fluctuations at sub-grid scales that entail closure through mathematical models, given by:

$$\tau^{sgs} = \overline{\boldsymbol{V}\boldsymbol{V}} - \overline{\boldsymbol{V}}\,\overline{\boldsymbol{V}} \tag{3-12}$$

and estimated by a single sub-grid scale model of the eddy-viscosity type:

$$\tau^{sgs} - \frac{2}{3}\, k\, \boldsymbol{I} = - \frac{\mu^{sgs}}{\rho} \left(\nabla \overline{\boldsymbol{V}} + \nabla \overline{\boldsymbol{V}}^T \right) \tag{3-13}$$

where I is the identity tensor, k is the sub-grid scale turbulent energy and μ^{sgs} is the sub-grid scale viscosity. Both are determined from the one-equation SGS turbulent energy transport model accredited to Yoshizawa [79]:

$$\frac{\partial k}{\partial t} + \nabla.(k\bar{V}) = \nabla.[(\vartheta + \vartheta^{sgs})\nabla k + \tau^{sgs} \cdot \bar{\boldsymbol{V}}] - \varepsilon - \frac{1}{2}\tau^{sgs} : (\nabla\bar{\boldsymbol{V}} + \nabla\bar{\boldsymbol{V}}^{T}) \qquad (3\text{-}14)$$

where $\varepsilon = C_{\varepsilon}\, \varrho\, k^{(3/2)}/\, \Delta$ is the SGS turbulent dissipation $\vartheta^{sgs} = C_{k}\, \varrho\, k^{(1/2)}/\, \Delta$ is the SGS kinematic viscosity and $\Delta = V^{(1/3)}$ is the SGS length scale where V is the volume of the computational cell. The coefficients, found from statistical considerations, are $C_{\varepsilon} = 1$ and $C_{k} = 0.05$ [33].

The gaseous phase is represented by air. Any fuel vapour produced by low-pressure evaporation is given the properties of air. Fuel is allowed to vapourise when its pressure falls to the vapour pressure of diesel fuel at ambient temperature 1 kPa [45]. This flash boiling model can be considered as a basic cavitation model. Specific heat capacity, dynamic viscosity and Prandtl number are constant for each phase.

3.2.2.2 Numerical Solution Method

Mathematical models are solved by an implicit finite-volume method, which utilises second order spatial and temporal discretization schemes. The solution procedure employs Pressure Implicit with Split Operator (PISO) algorithm [69], together with conjugate gradient methods for coupled solution of mass and momentum conservation equations which is specifically suited to transient flows [81]. The advection terms are solved by a bounded Normalised Variable (NV) Gamma differencing scheme [82] with a blending factor of 0.2 and the interface compression scheme (CICSAM) by Ubbink [105] for capturing sharp immiscible interfaces. A conservative, bounded, second order scheme, Gauss linear, is used for Laplacian derivative terms with an additional explicit corrector for mesh non-orthogonality [82]. A second order, implicit discretization scheme (backward) is used for the time derivative terms. The numerical integration time-step is adjusted by velocity-based Courant–Friedrichs–Lewy (CFL), and a speed of sound based CFL set to below 0.15 and 2.0 respectively.

3.2.2.3 Boundary Conditions and Initial Set-up

The geometry of the experimental nozzle is determined using X-ray Computer-Aided Tomography (CAT) analysis as shown in Figure 3-1. This analysis reconstructs the images with the pixel number of 1016 × 1024 × 1024, and an effective voxel size of 2.318 μm.

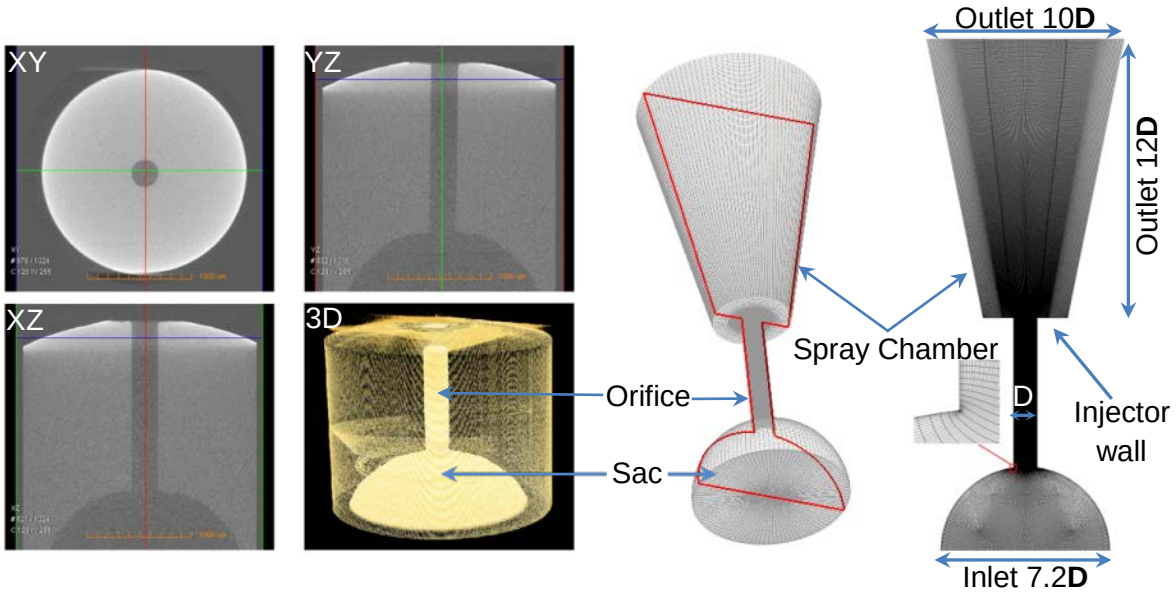

Figure 3-1. Left: X-Ray Tomography measurements of sac and orifice geometry. Middle: the structured hexahedral mesh based on CAT measurements. Right: cross-section of the computational domain presents the mesh resolution, dimension and condition of the boundaries for coarse case with 4 million cells. The nozzle inlet is sharp edged.

All the experimental conditions are replicated in numerical models including the sac volume inlet, spray chamber pressure and air and diesel fuel temperature and viscosity. Fuel properties and set up conditions are listed in Table 3-1. In the absence of direct measurement, sac pressure is assumed to increase from chamber pressure (30 bar) to 850 bar after 50 μs then to 1200 bar after a further 25 μs then constant at 1200 bar to the end of simulation at 100 μs. This is to some extent arbitrary but is premised on published data implying that the sac pressure rises rapidly during needle opening [10, 28, 29, 83]. For instance, Moon et al. [10] found that the quasi-steady stage jet velocity was reached when the needle lift was only 17% of the maximum needle lift. The ramp is chosen to give an approximate match of modelled and experimental penetration rates. The lower pressure rise rate in the second 25 μs is adopted to avoid numerical instabilities.

Fluid flow through the passage between the needle and seat is not modelled. In a real injector turbulence would develop in the needle/seat passage prior to the sac. This additional

turbulence could contribute to more significant and earlier jet breakup. A pre-simulation approach could involve modelling the flow through the needle/seat passage in some fixed configuration, perhaps with the needle partially open and thus quantifying the turbulent flow field, which would then be used as an the initial condition at sac inlet. While this approach has merit, it is beyond the scope of the current work. A uniform pressure boundary with a turbulent intensity of 4.4% is applied over the sac entry plane. Thus, any effects due to turbulence or flow asymmetry generated in the passage between the needle and seat [29, 37, 106-108] are not modelled. A non-reflective boundary with the constant pressure of 30 bar is employed at the spray chamber domain. The nozzle and sac walls are adiabatic.

Table 3-1. Fuel properties and operating conditions based on experimental setup.

Parameter	Value
Injection pressure	120 Mpa average
Chamber pressure	30 bar
Nozzle diameter	0.25 mm
Nozzle length	1.6 mm
Nozzle nominal geometry	$K_S = 0$ (cylindrical)
Nozzle inlet radius	Sharp edged
Sac volume	0.19371 mm^3
Walls temperature	25°C
Fuel	Diesel
Fuel temperature	25°C
Fuel density	832 kg/m^3
Fuel Kinematic viscosity	2.52×10^{-6} m^2/s
Fuel Re	$7\times10^3 \leq Re_l \leq 46\times10^3$
Fuel We	$4\times10^4 \leq We_l \leq 2\times10^6$
Gas	Compressed air
Gas temperature	25°C
Density ratio	42
Surface tension	0.03 N/m
*Indicative Injection velocity	367
*Fuel Mach number	367 / 1250 = 0.3
*Ohnesorge number	0.077

* Injection velocity, Mach and Ohnesorge numbers are for the developed spray, calculated based on experimental measurements [84]. The nozzle diameter is used as the length scale.

At the start of each injection in the experimentation, the nozzle is neither necessarily full nor empty of fuel due to the transient physics associated with the End of Injection (EOI) process from the previous injection event [12, 28, 29, 83]. The initial model conditions have the sac and 5.2D of the 6.4D long orifice (81% of the nozzle length) filled by diesel fuel at a pressure of

30 bar and the remainder of the nozzle filled with air. This initial stage is somewhat arbitrary and the rationale is described in Ghiji et al. [109].

A 3D hexahedral structured mesh with the non-slip boundary condition on the walls of the sac and nozzle is implemented to capture the non-axisymmetric nature of the injector flow and disintegrating jet [2, 4, 47, 68, 84], as shown in Figure 3-1. By generating a high grid resolution at the boundary layer of the nozzle walls, the utilization of a wall function has been obviated. Structured grids are used to achieve higher quality and control which may be sacrificed in unstructured and hybrid meshes. In addition, the efficiency of the differencing scheme for bounding the convection term of the transport equations in a structured mesh is much higher in comparison with an unstructured mesh [85].

A mesh sensitivity study is carried out using four mesh resolutions, very coarse (0.6 million cells), coarse (4 million cells), medium (8 million cells), and fine grid (20 million cells). The cell size is refined down to average 0.5 μm in the nozzle and 3 μm in the primary atomisation zone for the fine mesh case. This cell size can capture droplets down to the 3 μm range based the optimistic premise that 5 cells can give a reasonable representation of a single droplet [48]. The resolution of these cases, time-step range, the number of CPUs, and computational cost (wall clock time) for each case are summarised in Table 3-2.

Table 3-2. Summary of meshes and computation parameters for numerical models. Total simulation time is 100 μs.

Case	Average Spatial Resolution (μm and cells/D)			Cell count	Time Step ($\times 10^{-9}$ S)	CPU (core count)	Wall clock time (hours)
	Sac	Orifice	Chamber				
Very Coarse	25 (20/**D**)	4 (65/**D**)	14 (20/**D**)	0.6×10^6	$1.5 \leq \Delta T \leq 30$	32	208
Coarse	13 (40/**D**)	2 (130/**D**)	6.5 (40/**D**)	4×10^6	$0.7 \leq \Delta T \leq 10$	128	501
Medium	7.5 (55/**D**)	1.2 (210/**D**)	5 (50/**D**)	8×10^6	$0.5 \leq \Delta T \leq 8$	256	739
Fine	4 (85/**D**)	0.5 (500/**D**)	3 (75/**D**)	20×10^6	$0.4 \leq \Delta T \leq 4$	512	965

3.3 Results and Discussions

3.3.1 Mesh Dependency and LES Quality

In order to take into account the significance of in-nozzle generated turbulence on primary atomisation [48, 75], the size of the cells in the nozzle for the fine resolution case was decreased to the order of the Kolmogorov length scale $\eta = (\upsilon^3/\varepsilon)^{1/4}$ where ε is the average rate of dissipation of turbulence kinetic energy per unit mass. To resolve a given length scale η, the grid scale must be less than half of the length scale [82]. The smallest length scales associated with the flow field for the fully developed spray are reported in Table 3-3. It can be seen in this table that η_l in the nozzle is much larger than the mesh size for the finest mesh. This mesh resolution enables good prediction of small eddies of the liquid phase inside the nozzle. It was not possible to achieve mesh scales below the Kolmogorov length scale for the gas phase demonstrating the necessity for employing a sub-grid scale model to include turbulence effects in the gas phase.

Table 3-3. Kolmogorov length scales for the liquid and gas phases of the developed spray where the turbulence intensities used are 4.4% and 10%, respectively. The indicative injection velocity 367 m/s is used for these calculations.

Parameter	Value (μm)
Liquid phase Kolmogorov length scale, η_l	0.7
Minimum mesh size in nozzle hole for fine case, Δx_{min}	0.1
Gas phase Kolmogorov length scale, η_g	0.1
Minimum mesh size in spray chamber for fine case, Δx_{min}	1.7

The ratio of resolved turbulent kinetic energy (k_{res}) to total turbulent kinetic energy (TKE = k_{sgs}+ k_{res}) indicates the quality of the LES model and consequently the adequacy of the overall grid fineness [33, 110]. For satisfactory LES modelling this ratio should be more than 80% [110]. The resolved turbulent kinetic energy is calculated over 10 μs at a probe point located at 4D (1 mm) from the nozzle exit. The overall ratio of k_{sgs} to TKE predicted by the sub-grid scale turbulent model at the quasi-steady stage with the fine mesh resolution is equal to 2.4%. In addition, the numerical turbulent diffusion due to the discretization error is the same magnitude as the turbulent diffusion computed by the sub-grid scale model [33, 110]. Thus, at the quasi-steady stage with the finest grid, the resolved turbulent kinetic energy is calculated at 95.2 % of TKE indicating a satisfactory LES model.

Total pressure and mean velocity at nozzle exit were calculated for all meshes at the quasi-steady stage ($P_{injection}$ = 1200 bar) and the result is shown in Figure 3-2. The difference between the medium and the coarse mesh was in the order of 6.6%, while for the fine and the medium it was 1.1%.

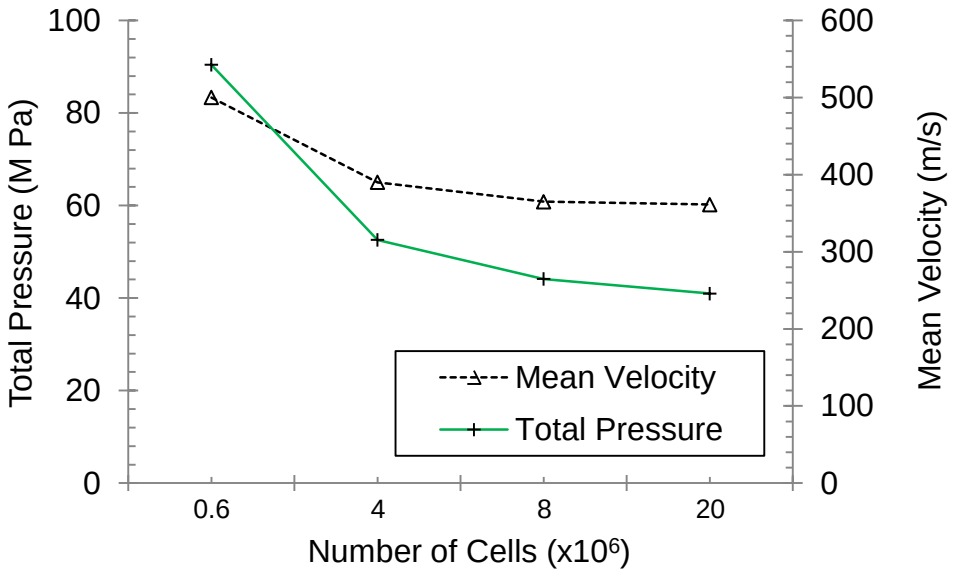

Figure 3-2. Comparison of total pressure and mean velocity for different mesh resolutions calculated on a cross-sectional plane at the nozzle hole exit (z/d=0), and the sac inlet pressure of 1200 bar.

Average radial profiles of absolute velocity magnitude and mass fraction of liquid at various distances from the nozzle hole inlet (1D, 2D, 4D, and 6.4D the end of the nozzle hole) for three meshes at the quasi-steady stage ($P_{injection}$ = 1200 bar) are shown in Figure 3-3. Maximum velocity of 480 m/s is captured at the centre of the nozzle (r/D=0) as expected. The average velocity and mass fraction at different locations inside the nozzle hole show tendency toward grid convergence for the finest mesh. The velocity on the nozzle wall (r/D=0.5) is zero as a result of the no-slip condition applied to the injector walls. The velocity of the layer of gas near the walls remains near zero until near the nozzle exit where inflow of gas from the chamber results in increased velocity magnitude. The gas layer thickness grows with distance from the nozzle inlet reaching at the nozzle exit around 70% of the cross-sectional area occupied by the liquid phase.

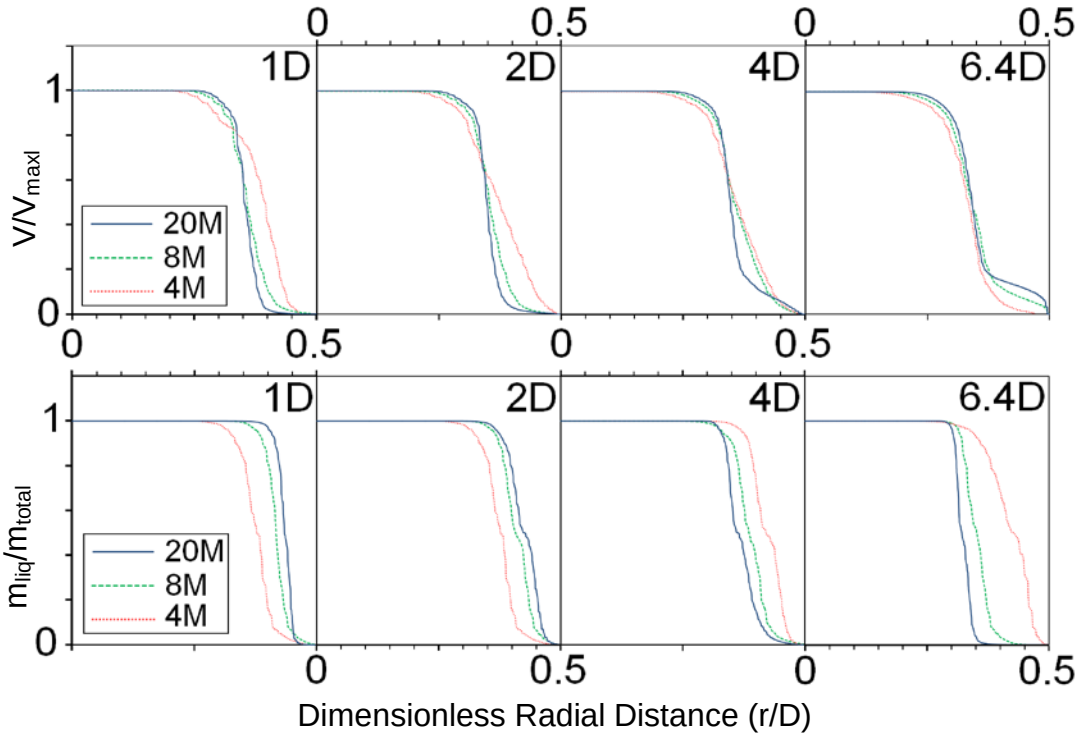

Figure 3-3. Averaged radial profiles of absolute velocity magnitude and liquid mass fraction on cross-sectional planes at 1D, 2D, 4D, 6.4D (end of the nozzle hole) from the nozzle hole inlet, at the quasi-steady stage. Maximum velocity is 480 m/s. The results show tendency to grid convergence for the finest mesh.

Probability density functions of droplet size for the entire domain outside the nozzle for each mesh density are shown in Figure 3-4. Both the droplet size range and the dominant size reduce with increasing mesh resolution. It can be seen however that both of these quantities show tendency to converge for the finest mesh. The probability density function for the fine mesh case demonstrates that the dominant droplet diameter captured is around 2.5 µm.

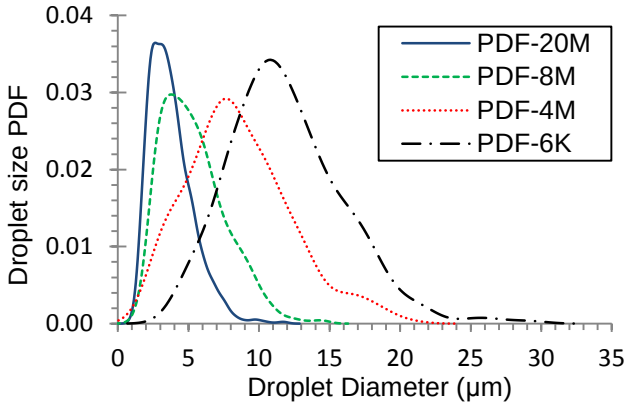

Figure 3-4. Probability density functions of droplet size for four mesh resolutions at the quasi-steady stage, demonstrating near convergence of dominant size and size range for the finest mesh.

The impact of mesh density on atomisation is shown with an instantaneous mass distribution of all droplets at various axial distances from the nozzle exit for three mesh resolutions at the quasi-steady stage of injection, presented in Figure 3-5. The value of total atomised mass is very small close to the nozzle exit, increases slowly up to 10D and then increases rapidly further downstream. Increasing the mesh density reduces the size of captured droplets, as shown in Figure 3-4, which consequently reduces the total mass of disintegrated liquid. Grid dependence of atomised mass increases with distance from the nozzle exit, due primarily to increasing grid size. The rest of the simulations presented in this paper are performed with the finest mesh. A still finer mesh was not considered practical due to limitations of the available computational power.

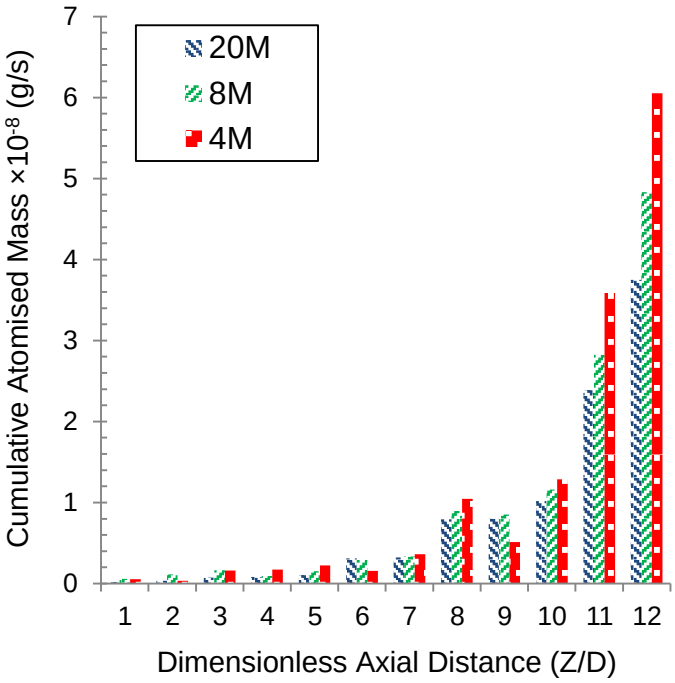

Figure 3-5. A snapshot of cumulative mass distribution of droplets along the axial distance from the nozzle exit for three mesh resolutions at the quasi-steady stage of injection. The value of total atomised mass is very small close to the nozzle exit, accelerates slowly up to 10D and then increases rapidly further downstream.

3.3.2 Mass Flow Rate

Mass flow rate and discharge coefficient at the nozzle exit predicted with the fine grid are shown in Figure 3-6. SOP is 12 μs after start of simulation and sac pressure reaches its maximum value of 120 MPa at 75 μs after start of simulation, so maximum sac pressure is reached at 63 μs ASOP. It can be seen in Figure 3-6 that modelled mass flow rate begins to level out at around

45 μs ASOP. The measured steady state flow rate and discharge coefficient for this injector are 0.0139 kg/s, and 0.6219 respectively [84] and the modelled values of 0.013 kg/s and 0.64 at the quasi-steady state are close to the measured values. The measured mass flow rate was found by repeatedly firing the injector for long opening times of 17 ms for more than 100 injection events, dividing the fuel consumed by the total time for which the injector needle was open. By this method, the time at which the injector needle is partially open is only a very small fraction of the total measurement time. There is an estimated ±10% uncertainty in measured mass flow rate so the modelled values agree within experimental error, giving confidence in the accuracy of applied numerical methods.

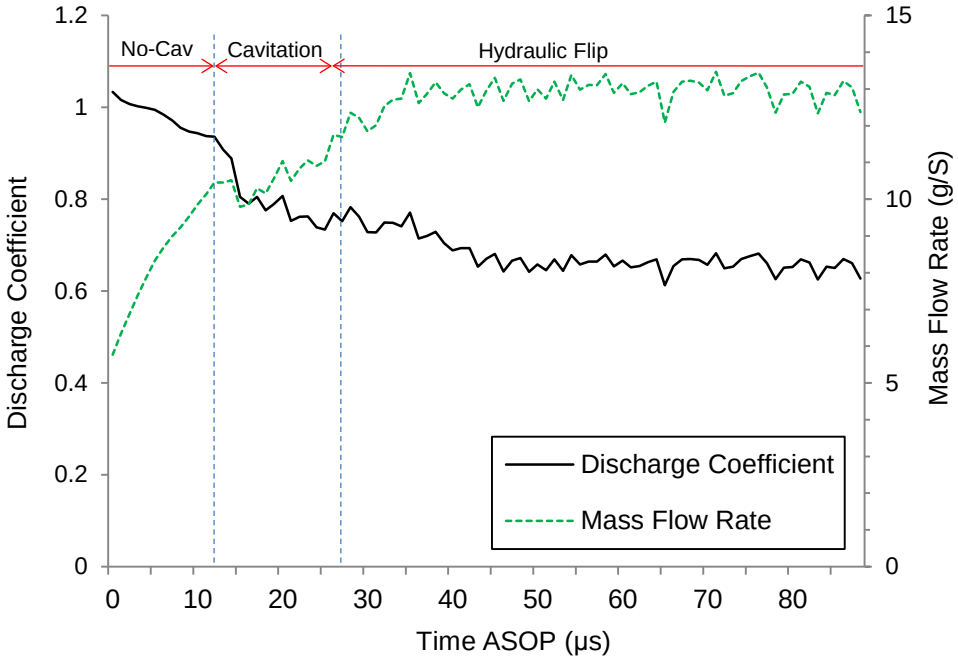

Figure 3-6. Discharge Coefficient (Cd) and total mass flow rate at the nozzle exit against time ASOP. The onset of cavitation occurs at 11 μs ASOP. The mass flow rate begins to level out at around 45 μs ASOP and reaches an average value of 0.013 kg/s in the quasi-steady stage.

The numerically predicted contraction coefficient is slightly higher than the theoretical limit for an ideal sharp entrance orifice ($C_c = \pi/(\pi+2) = 0.611$), with a value of $C_c = 0.619$.

3.3.3 Penetration Velocity

The Reynolds number and mean velocity of the flow at the nozzle exit for different times ASOP, predicted by the fine grid are presented in Figure 3-7. The mean velocity and Reynolds number increase up to around 100 MPa pressure difference then steady out at mean values of 480 m/s, and 46000 respectively.

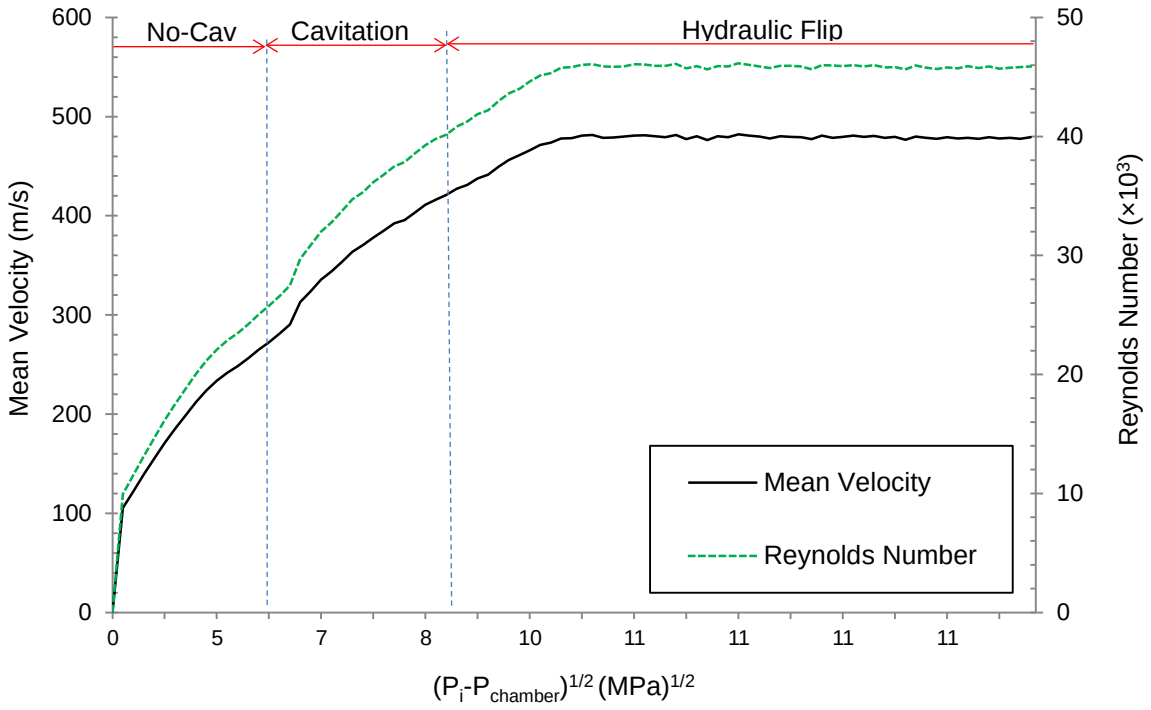

Figure 3-7. Mean velocity and Reynolds number of the the mixed-phase jet at the nozzle exit, against the square root of the difference between the sac pressure and the chamber pressure.

The displacement of the leading edge and time interval between shots are used to calculate penetration velocity, similar to the previous experimental studies [111-113], depicted in Figure 3-8. The jet leading edge is detected and distinguished from the image background using an intensity threshold criterion. A number of shots over a range of inter-frame times varying between 1 and 15 μs are analysed. The error bars are based on the accuracy of the detection of the leading edge of the jet and this is a function of the inter-frame time. The scatter in the experimental results demonstrates shot to shot variability in spray development. The jet penetration velocity at various axial distances from nozzle exit with corresponding time ASOP, demonstrated in Figure 3-8, show good agreement between numerical and experimental results.

Uncertainties arise in these measurements from two dominant sources: variability in the measurement of spray image timing relative to SOP; and shot-to-shot variations in the spray dynamics. Due to uncertainties in acquiring an exact time of the start of injection, the penetration velocity of the jet was plotted against the location of the jet leading edge instead of the time after start of injection.

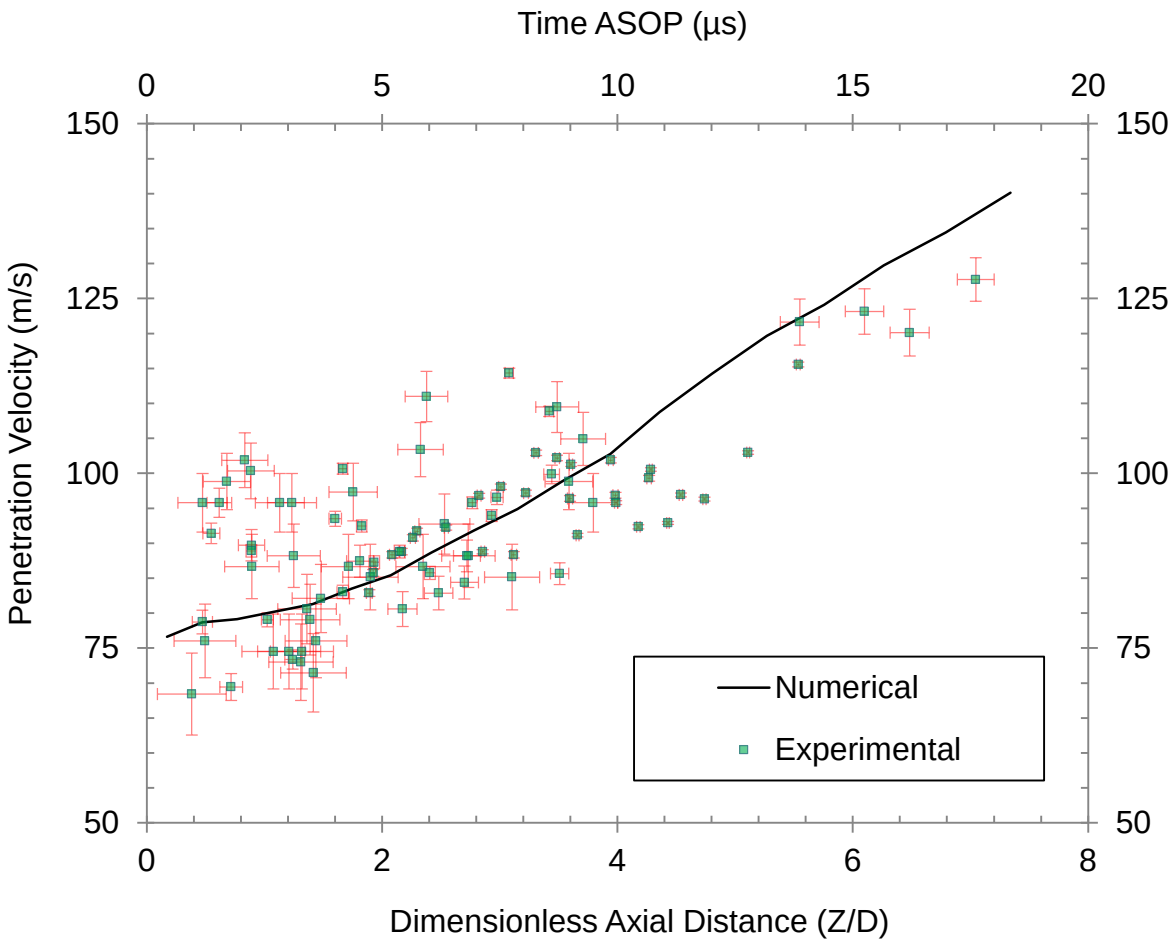

Figure 3-8. Experimental and numerical values of penetration velocity of the leading edge at various axial distances from the nozzle exit and time ASOP. The location of the leading edge at different times ASOP is correlated.

3.3.4 Evolution of Spray Structure

3.3.4.1 Morphology of Penetrating Jet during the early opening transient

Figure 3-9 shows a comparison of experimental images with the numerical results for the fine mesh case at different times ASOP using the 2× Barlow lens to give a total magnification of 7.7:1. Some transparency can be seen in the shadowgraphy images at the leading edge. This is thought to be due to air inclusion inside the nozzle, from the previous injection. The existence of ingested air inside the injector was reported by Swantek et al. [12]. The air inclusion inside the injector influences the spray structure and could be a source of the observed deviation between experimental and numerical results.

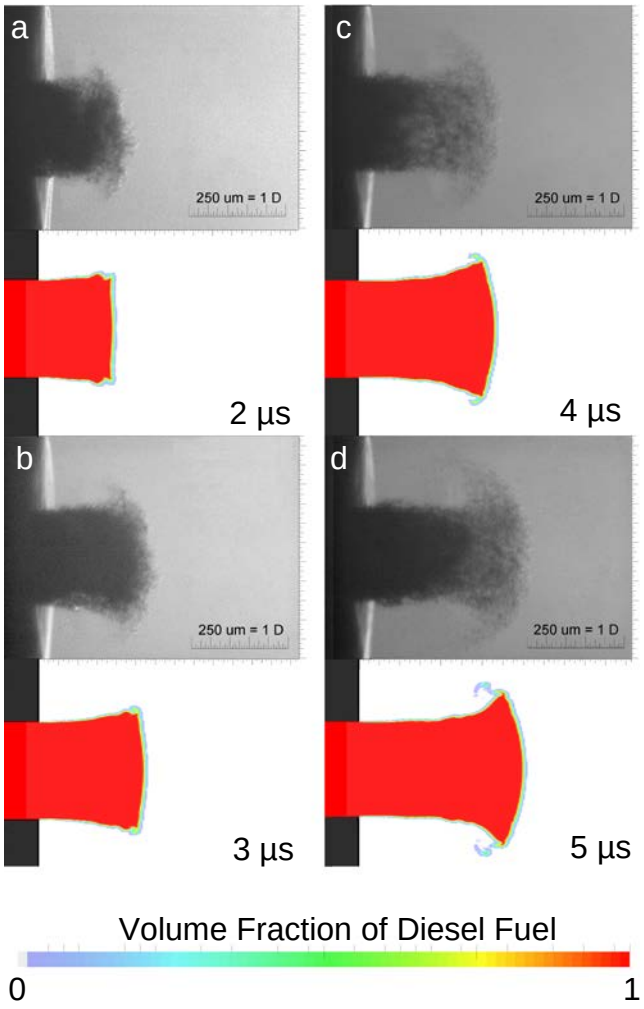

Figure 3-9. Comparison of experimental images with numerical results for the fine mesh case with the highest magnification. Each column of the experimental image is from a different injection event captured from two consecutive frames with 1 µs inter-frame time.

Consecutive images in (a) and (b) are from a single shot of the injector, while successive images in (c) and (d) are from another shot of the injector, each pair with 1 µs time interval. It is apparent in (c) and (d) that a liquid core is advancing into the dispersed leading edge. Numerical results show the structure of the jet coloured by the volume fraction of diesel fuel (γ) at different times ASOP. Cells containing air only are shown in white.

The numerical and experimental results show the early development of the umbrella-shaped leading edge and the early stages of shedding of droplets from the rim of the leading edge. Shadowgraphy images with a larger field of view are compared with numerical results in Figure 3-10, presenting the general structure of the diesel spray. In this Figure, images (a) and (b), (d) and (e), (g) and (h), (i) and (j) are paired, each pair captured from a single injection

event with 1 μs delay between two consecutive frames. The necking of the jet behind the umbrella can be seen in the experimental images in Figure 3-10, while it is not marked in the simulations. The difference is possibly due to the presence of air in the experimental jet, as indicated by the partial transparency of the experimental images, and thus more rapid disintegration. The outer recirculating gas flow removes the generated droplets and advects them toward the outer flow. Another difference between the numerical and experimental results is in the production of very small droplets in the experimental images unlike them that in the simulations. This is due to the constraint in computational resources where the grid resolution in the computational domain is insufficient to resolve the small eddies in the gas phase which influences the breakup process of the ligaments and droplets.

The overall morphology of the early spray as modelled here taking into account compressibility is not significantly different from simulations assuming incompressible fluid as reported in Ghiji et al. [109]. This is because the Mach number of the liquid at this stage of the injection is less than 0.3 and thus compressibility effects are negligible. Further, cavitation is only just beginning. Cavitation is apparent with the formation of cavities on the walls just downstream of the nozzle entrance and the associated formation of cavitation bubbles.

The onset of cavitation occurs at 11 μs ASOP where the pressure of diesel fuel drops to the diesel fuel vapour pressure, 1 kPa, just after the sharp edged nozzle hole inlet, as depicted in Figure 3-11. The development of cavities further downstream can be seen in images b, and c with their corresponding static pressure distribution illustrated in images f, and g respectively. At image d 27 μs ASOP, cavities extend to the end of nozzle hole while high-pressure spray chamber air penetrates into the gap between the nozzle wall and liquid jet interfaces.

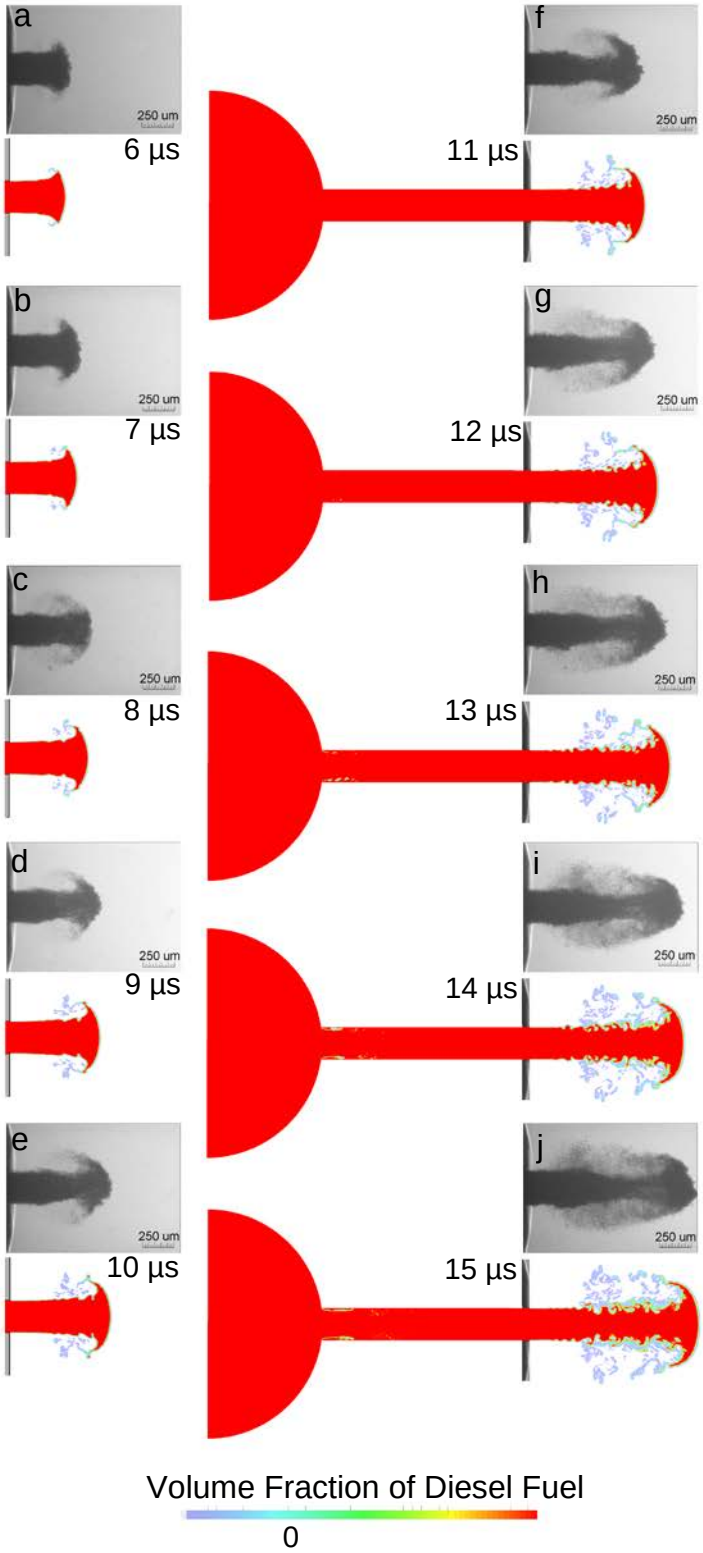

Figure 3-10. Comparison of experimental images with numerical results extracted from the fine case for the SOP process. Images a and b, d and e, g and h, i and j are paired, each pair captured from the same injection event with 1 µs inter-frame time. Numerical results show the structure of the liquid jet coloured by γ at corresponding times ASOP. The onset of cavitation downstream of the nozzle entrance is apparent. Cavitation bubbles can be seen arising near the nozzle entrance which are then transported down the nozzle.

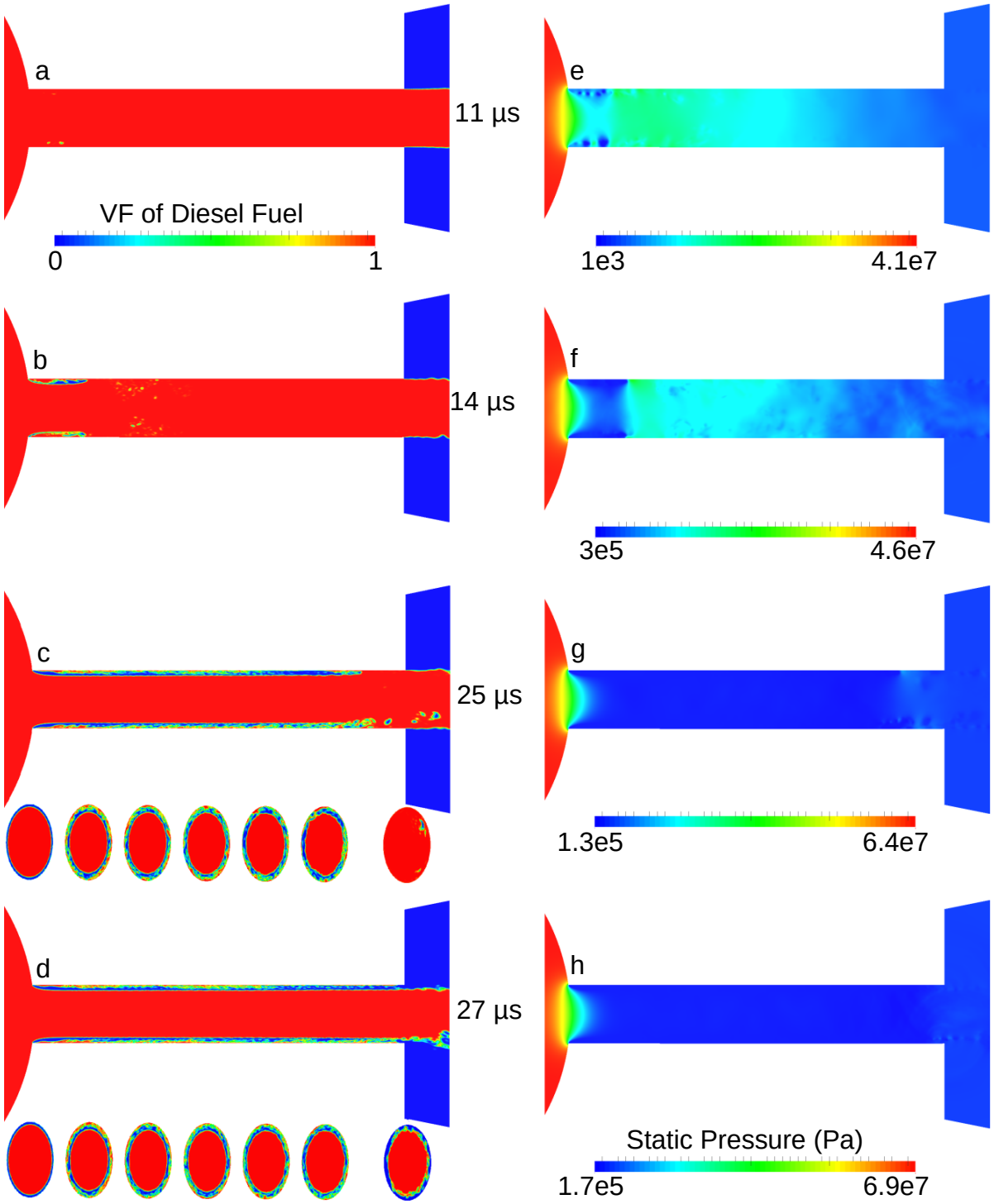

Figure 3-11. A zoomed-in view of the nozzle hole shows the onset and enhancement of cavitation at various times ASOP coloured by the volume fraction of diesel fuel (images a-d), and static pressure (images e-h). The onset of cavitation can be seen in the image a where the static pressure of liquid drops to the liquid vapour pressure, 1000 Pa, in image e. Hydraulic flip, a detachment of liquid from the entire nozzle wall is depicted in images d, and h.

3.3.4.2 Evolution of in-nozzle and jet liquid-gas turbulent structures

3.3.4.2.1 Starting vortex

The experimental images show a toroidal vortex just behind the leading edge of the emerging spray within the first few microseconds of penetration. This structure is apparent due the density gradients in the chamber air inherent in the toroidal flow. Further, numerous experimental images show the vortex very close to the nozzle exit, prior to the emergence of liquid. This is thought to be due to the presence of air in the nozzle, with the air being ejected before the fuel and thus creating the shear-induced vortex, as seen in Figure 3-12 which illustrates the initial vortex formation in the gas phase experimentally (12-a) and numerically (12-b and c). The numerical result is shown at 2 μs Before Start Of Penetration (BSOP). A positive Q-criterion showing the small-scale turbulent structures where mixing is important is shown in Figure 3-12-c. The colour in the Q-isosurface indicates the vorticity in the z-direction, red indicates clockwise rotation and blue counter clockwise rotation. The shots showing the vortex before the fuel appears are generally for earlier timing meaning that there is always air ejected first but this is only seen for the earliest timing of the images. The initial air slug seen experimentally is taken as further evidence of the existence of air in the nozzle prior to injection. In section 3.2.2.3 the inclusion of air as the initial condition is discussed. Modelled air density is also plotted in Figure 3-12 showing the density gradient associated with the starting vortex induced by the initial slug of air prior to liquid. It is likely that the amount of air in the nozzle and the configuration of the air-fuel interface vary from shot to shot.

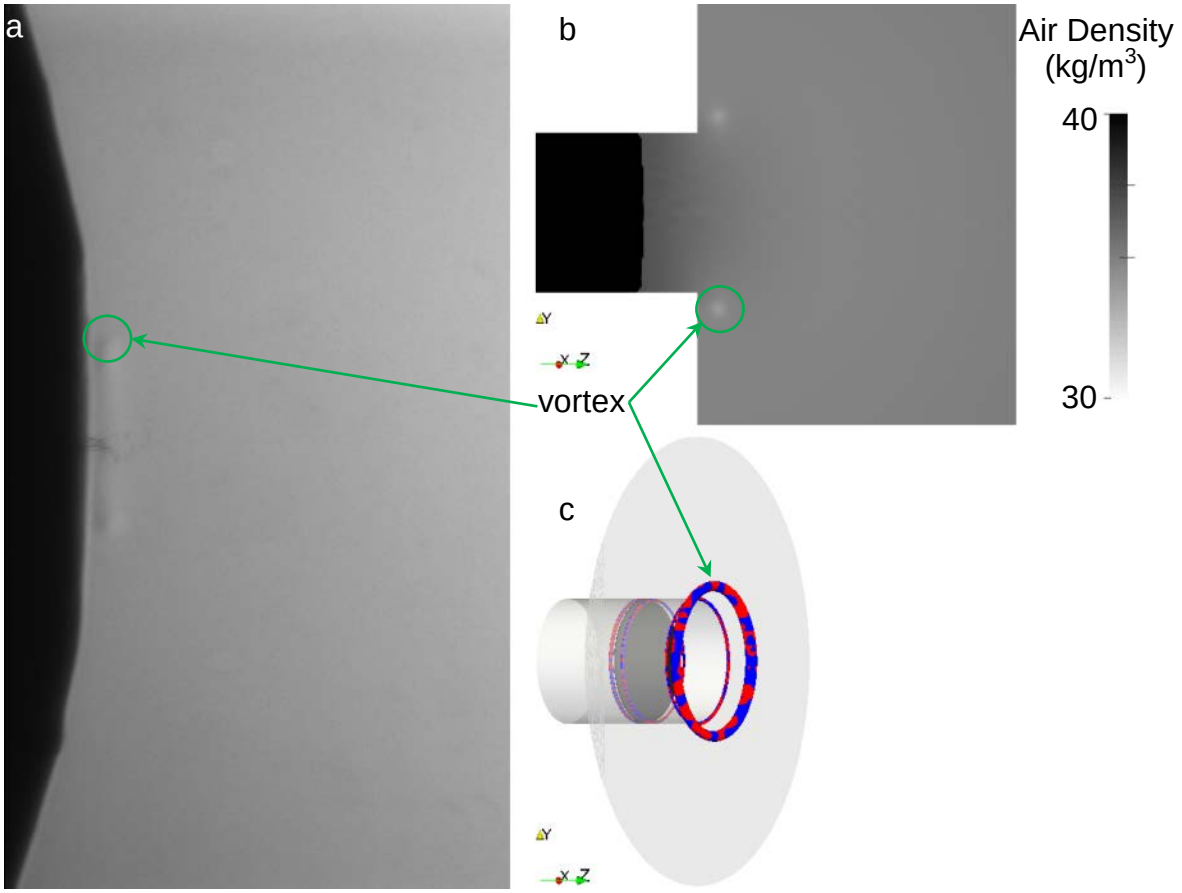

Figure 3-12. Starting vortex at or just before the start of penetration (BSOP); image a shows shadowgraphy result; image b and c depict the CFD results at 2 μs BSOP. Image b is shaded by air density on a centralised cut plane. Image c shows the Q-isosurface of 5×10^{12}, coloured by vorticity in the z-direction, where red indicates clockwise rotation and blue counter clockwise rotation. The body of the injector is shown in light grey and the dark grey disc shows the location of the leading edge of the liquid (filtered by a liquid fraction of 0.5) relative to the vortical structures.

Figure 3-13 illustrates the initial vortex formation in the gas phase experimentally (13-a) and numerically (13-b and c) after the liquid has begun to penetrate. The numerical result is shown at 2 μs ASOP. A positive *Q*-criterion showing the small-scale turbulent structures where mixing is important is shown in Figure 3-13-c. The isosurface volume fraction of liquid $\gamma = 0.5$ is also shown in black to represent the location of the leading edge of the liquid relative to the vortical structures.

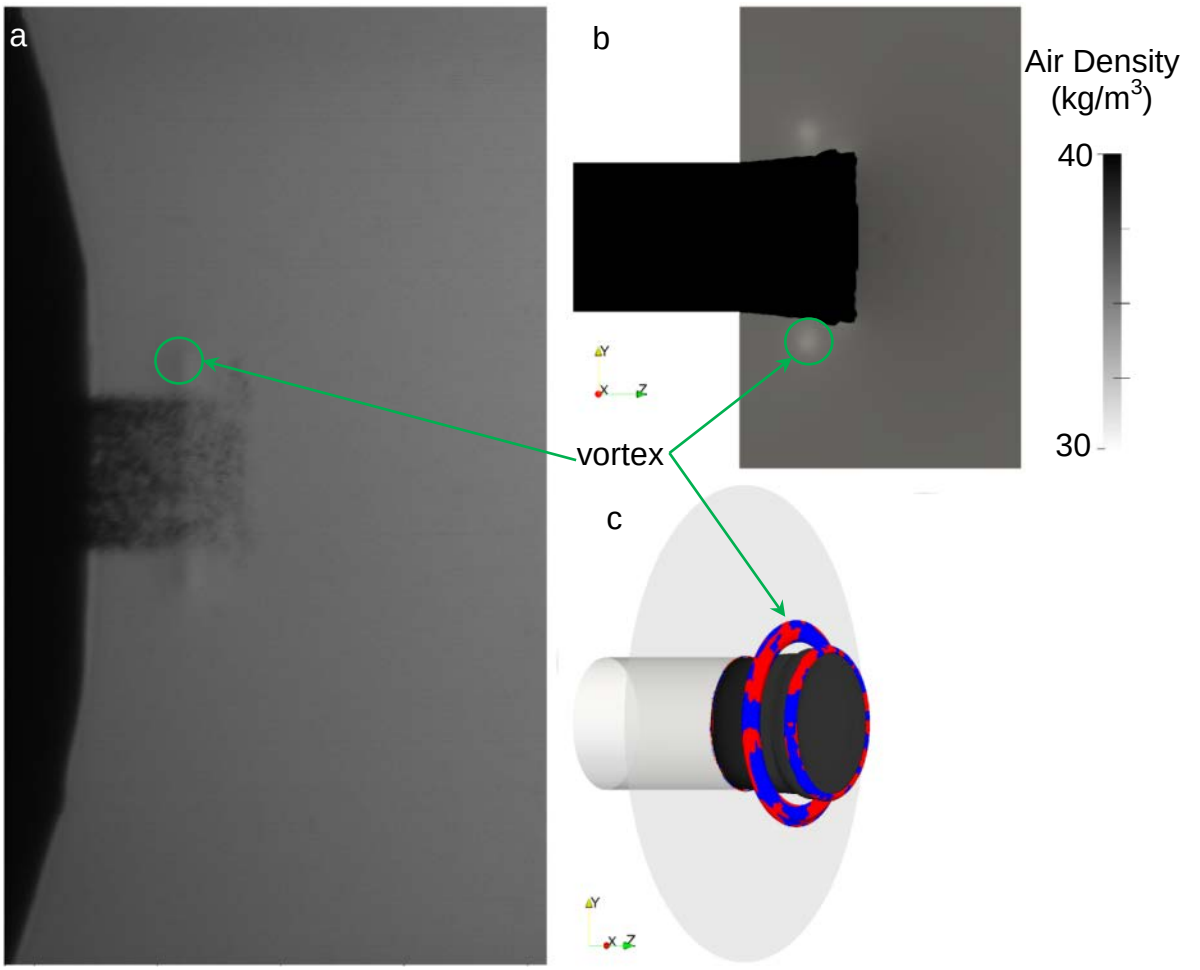

Figure 3-13. Starting vortex at the start of penetration; image a shows shadowgraphy result; images b and c depict the CFD results at 2 μs ASOP. Image b shows the starting vortex through the centralised cut plane, coloured by air density range. Image c shows the Q-isosurface of 5×10^{12}, coloured by vorticity in the z-direction, red indicates clockwise rotation and blue counter clockwise rotation. The body of the injector is shown in grey and the black colour shows the location of the leading edge of the liquid (filtered by a liquid fraction of 0.5) relative to the vortical structures.

The jet and vortex propagation velocities are compared in Figure 3-14. Experimental values are shown for 16 different double frame shots, with 1, 2 or 3 μs inter-frame time. The error bars are based on the accuracy of the detection of the leading edge of the jet and the centre of the vortex. Predicted liquid and vortex propagation rates are also plotted. The modelled vortex propagation rate is found by integrating velocity over the Q-criterion isosurface of 5×10^{12}. The dip in the modelled vortex penetration rate around $Z/D = 0.4$ corresponds to the time when the fuel leading edge reaches the vortex. It can be seen that the vortex propagation rate is approximately 40% of the jet leading edge propagation rate on average. The liquid propagation rate shows good agreement between experiment and model, while greater differences are seen

between the experimental and modelled vortex propagation rate. The source of the variation in the measured results and the differences between the measured and modelled results are most likely due to variability in the location of the air-fuel interface inside the orifice prior to injection.

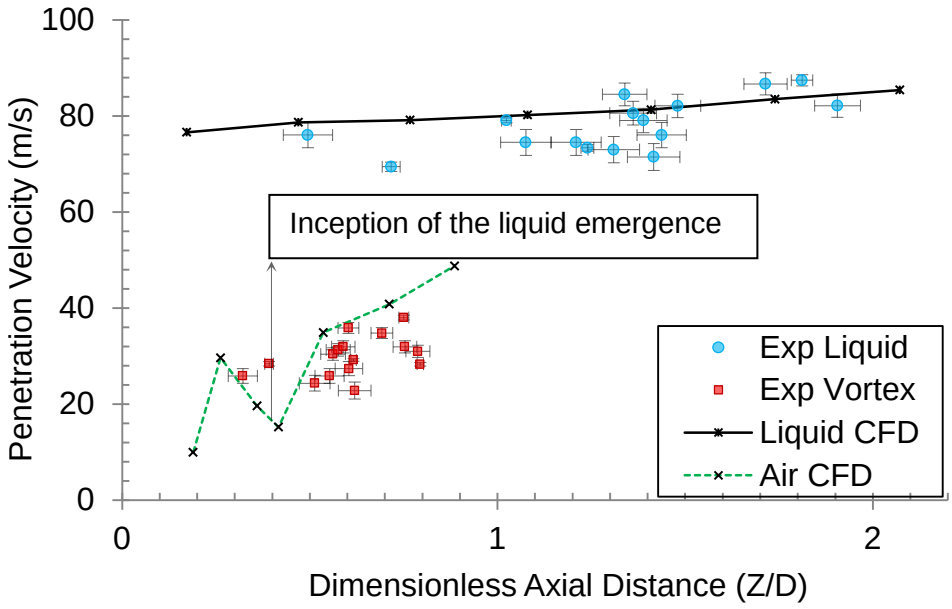

Figure 3-14. Experimental measurements of penetration velocity for the jet leading edge and the starting vortex at a different distance from nozzle hole exit.

3.3.4.2.2 Effects of cavitation and in-nozzle turbulence on spray development

The computed spray structure at various times ASOP is illustrated in Figure 3-15. In the left column (a-f), the fluid in the sac and nozzle is coloured by velocity magnitude and the 0.5 liquid volume fraction isosurface in the chamber is coloured by turbulent kinetic energy. In the right column (g-l), turbulent structures are depicted using the Q-criterion isosurface of 5×10^{12} coloured by vorticity magnitude (for a clearer presentation, high value 2×10^{8} of vorticity at the sharp edged nozzle hole inlet has been excluded).

At 12 μs ASOP, Figure 3-15-a, g, toroidal streamwise waves are apparent at the gas-liquid interface in the vicinity of the nozzle exit. These waves are also apparent as coherent toroidal structures in the Q-plot. The jet leading edge velocity is 105 m/s and the velocity at nozzle exit is 198 m/s corresponding to a Reynolds Number of 9930 and 18720, respectively. These streamwise waves could be potentially generated due to either Kelvin-Helmholtz instability or 2D Tollmien-Schlichting instability as recently reported by Shinjo et.al [64]. The turbulence generated primarily at the sharp nozzle inlet but also in the boundary layer develops with an increase in nozzle velocity. Cavitation onset occurred at 11 μs ASOP.

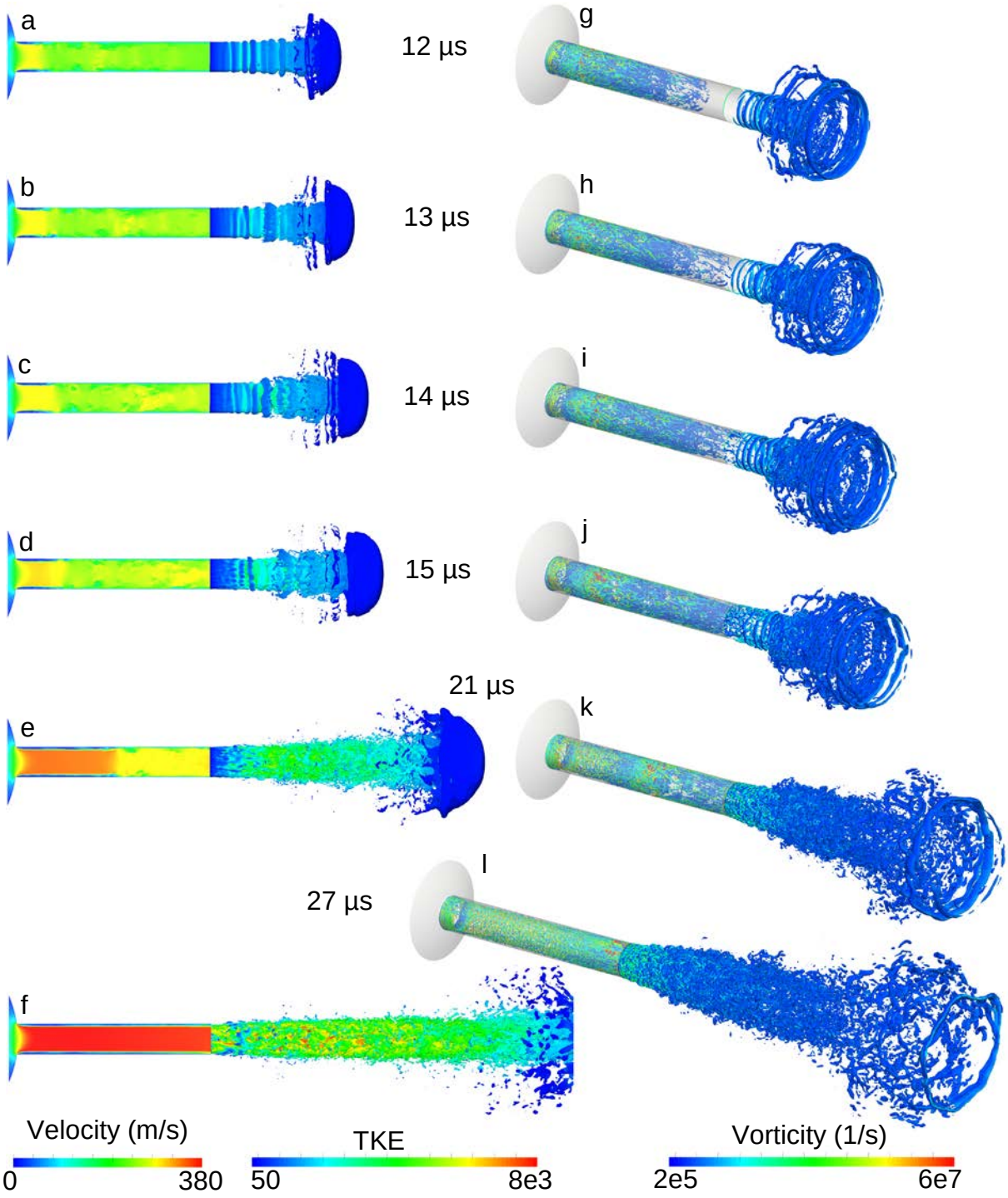

Figure 3-15. Evolution of in-nozzle and jet liquid-gas turbulent structures at different times ASOP. In the left column (image a-f), in-nozzle flow is coloured by velocity magnitude; liquid-gas isosurface of 0.5 at the spray chamber is coloured by Turbulent Kinetic Energy (TKE). In the right column at corresponding times (image g-l), the development of turbulence is illustrated using Q-isosurface of 5×10^{12}, coloured by vorticity magnitude (for a clearer presentation, the high value of vorticity of 2×10^{8} at the sharp edged nozzle hole inlet has been excluded).

Experimentally, the streamwise waves were difficult to capture in the image due to the obscuration of the jet surface by the cloud of fine droplets generated in the early stages of injection. In Figure 3-16, a streamwise surface waveform is just apparent on the top edge near the edge of the obscuring outer cloud of fine droplets.

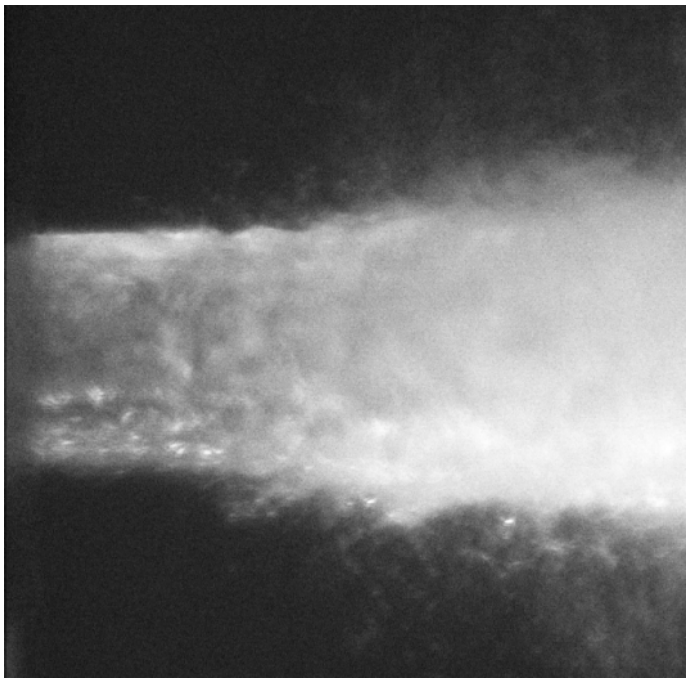

Figure 3-16. Experimental image of a spray near the nozzle using a diffuse sidelight imaging technique. A streamwise surface waveform is just apparent on the top edge near the edge of the obscuring outer cloud of fine droplets.

At 13 μs ASOP, Figure 3-15-b, h, the vapour cavities are developing and extending downstream inside the orifice, moderating the turbulence generated at the nozzle entrance and in the boundary layer. The influence of detachment can be seen in Figure 3-15-b. This is due to the increase in velocity at the nozzle entrance (extension of yellow colour further downstream of the nozzle) as a result of the reduction in cross-sectional area, similar results are reported by Dumont et al. [114], Desantes et al. [115], and Benajes et al. [116]. The developing in-nozzle turbulence is characterised by apparent streamwise, stretched vortices upstream of the nozzle exit. The toroidal streamwise waves on the jet are increasing in amplitude, possibly due to the increased upstream flow velocity. The disintegration of these waves tends to occur closer to the nozzle exit as the jet accelerates.

At 14 μs ASOP, Figure 3-15-c, i, the amplitude of the toroidal streamwise waves further increases. In-nozzle vortical structures have not yet reached the chamber. Onset, growth, and

disintegration of the streamwise toroidal waves continues to occur closer to the nozzle exit as the jet accelerates. Figure 3-17 shows the liquid volume fraction isosurface of 0.5, coloured by the velocity magnitude at 13.9 μs ASOP. Instabilities form on the emerging jet, and then develop into surface waves ultimately breaking up with downstream propagation. The zoomed views, 0.1 μs apart, show a typical ligament and its subsequent breakup into droplets, as part of the process of surface wave breakup. It can be seen that irregularities on the trailing edge of the umbrella play a significant role in the disintegration process. The separation of filaments from the trailing edge of the jet tip and their fragmentations lead to the generation of large droplets at the early stage of injection. An animation of the surface wave development between 12 ASOP and 15 ASOP is given in the supplementary material. It demonstrates the propagation of the toroidal streamwise waves in the downstream direction and the stretching of the leading edge umbrella prior to the shedding of droplets.

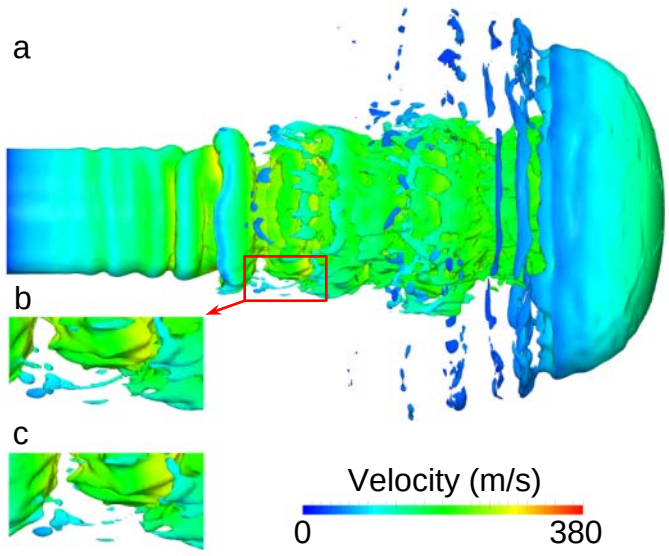

Figure 3-17. A view of surface instabilities forming surface waves that break up with their downstream propagation, filtered by the liquid volume fraction isosurface of 0.5, coloured by velocity magnitude at 13.9 μs ASOP. The separation of filaments from the trailing edge of the jet tip and their fragmentation are apparent. The zoomed-in views show the breakup of a filament between 13.9 μs (b), and 14 μs (c) ASOP.

At 15 μs ASOP, Figure 3-15-d, j, the impact of cavitation lowering the turbulence level at the nozzle entrance can be clearly seen in the Q criterion plot, about 2 nozzle diameters downstream of the nozzle entrance. Further downstream, longitudinal vortical structures formed earlier emerge from the nozzle exit coinciding with the appearance of spanwise longitudinal

waves on the jet surface near the nozzle exit. By 15 μs the coherent toroidal streamwise waves have disappeared, replaced by hairpin vortices at 16 μs.

At 21 μs ASOP, Figure 3-15-e, k, the vapour cavities have extended to the middle of the nozzle where a distinctive increment in the jet velocity is apparent. Much greater disintegration of the jet occurs at this stage corresponding to the influence of the in-nozzle turbulence creating surface disturbances that promote instability and breakup. The Q criterion visualization, Figure 3-15-k, shows the growth in the thickness of the shear layer (mixing zones) about the jet periphery and umbrella shaped leading edge.

At 27 μs ASOP, Figure 3-15-f, l, the nozzle cavity reaches the nozzle exit and hydraulic flip ensues. In-nozzle turbulence production is significantly reduced with jet detachment from the nozzle sharp entrance no longer being affected by the nozzle wall. Turbulence production, however, remains due to flow contraction at nozzle entrance as apparent from the Q criterion visualization. The jet flow contraction associated with flow detachment at the nozzle entrance creates a momentary velocity decrease as shown in Figure 3-15-l. Beyond this stage, the jet approaches the quasi-steady stage with surface breakup rapidly commencing within a diameter from the nozzle exit.

The spatial distribution of droplet size and Weber number of each droplet outside the nozzle at the quasi-steady stage for the fine mesh resolution is shown in Figure 3-18. The 3D surface is constructed based on the location and diameter of all droplets coloured by their Weber number. At the edge of the jet, the droplet sizes are small and Weber numbers are large due to the high velocity of droplets just separated from the liquid core. The droplet sizes increase with increasing streamwise and radial distances as the velocities and Weber numbers decrease. Each peak on the surface is an individual droplet (2700 in total) from which the volumetric concentration can be seen to decrease with increasing streamwise and radial distances.

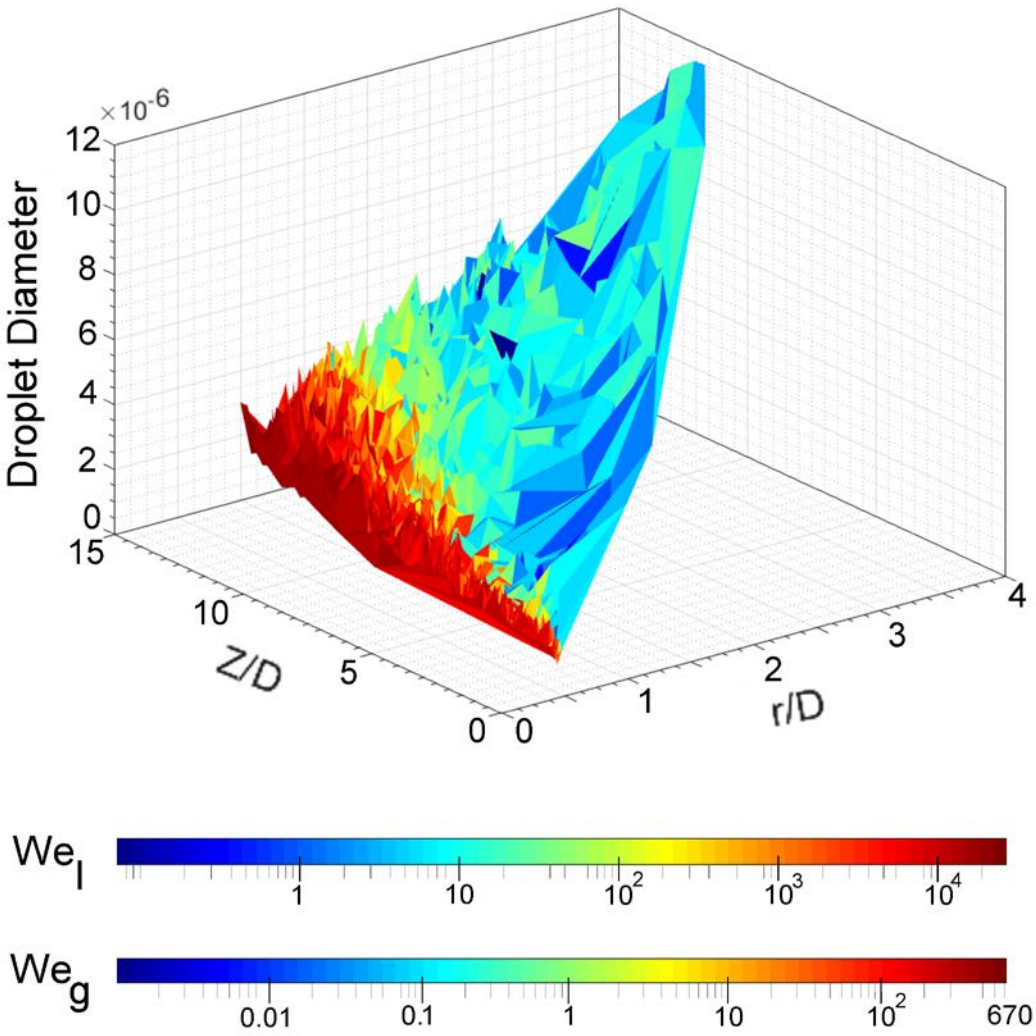

Figure 3-18. The spatial distribution of droplet size and Weber number of each droplet outside the nozzle at the quasi-steady stage for the fine mesh (20 million cells). The 3D surface is constructed based on the location and diameter of all 2700 droplets and coloured by their Weber number. The Weber number of each droplet is calculated based on the density of droplet (We_l) and the density of gas (We_g). It can be seen that the droplet sizes increase with increasing streamwise and radial distances as the velocities and Weber numbers decrease.

3.3.5 Shock Waves

By 27 μs ASOP, shock waves begin to appear in both the experimental and modelled results. The onset of shock waves also corresponds to the modelled onset of hydraulic flip, where vapour cavities initiated at the nozzle entrance extend to the full nozzle length and become ventilated with the chamber gas. This may be a coincidence but both are the result of increased nozzle exit velocity as the needle lift increases and the sac pressure builds towards its maximum value.

Figure 3-19 shows the experimental and computed images at the onset of shock waves and beyond. The first column (images a and b) shows the montaged images of shock waves edges, extracted using an edge detection algorithm in MATLAB, superimposed on the experimental results. The second column (images c and d) illustrates the numerical results. The white areas represent cells which have a liquid fraction greater than 0.1. Image (a) at 27 μs ± 2 μs ASOP shows the first signs of the onset of shock waves, while image (b) at 37 μs ± 2 μs, shows further development of shock waves than the image (a). Each of these images is obtained from separate shots. Numerous shots confirm the onset of shock waves at about 27 μs ASOP. The timing technique used here is explained in Section 3.2.1. The shock waves at the time of onset are seen to be most marked near the nozzle exit where the jet surface velocity is the highest. The numerical results presented in the image (c) show the onset of shock waves at essentially the same time ASOP and over a similar spatial extent to the measurements. An increase of about 15-25% of the air density at each shock wave front can be seen in images (c) and (d).

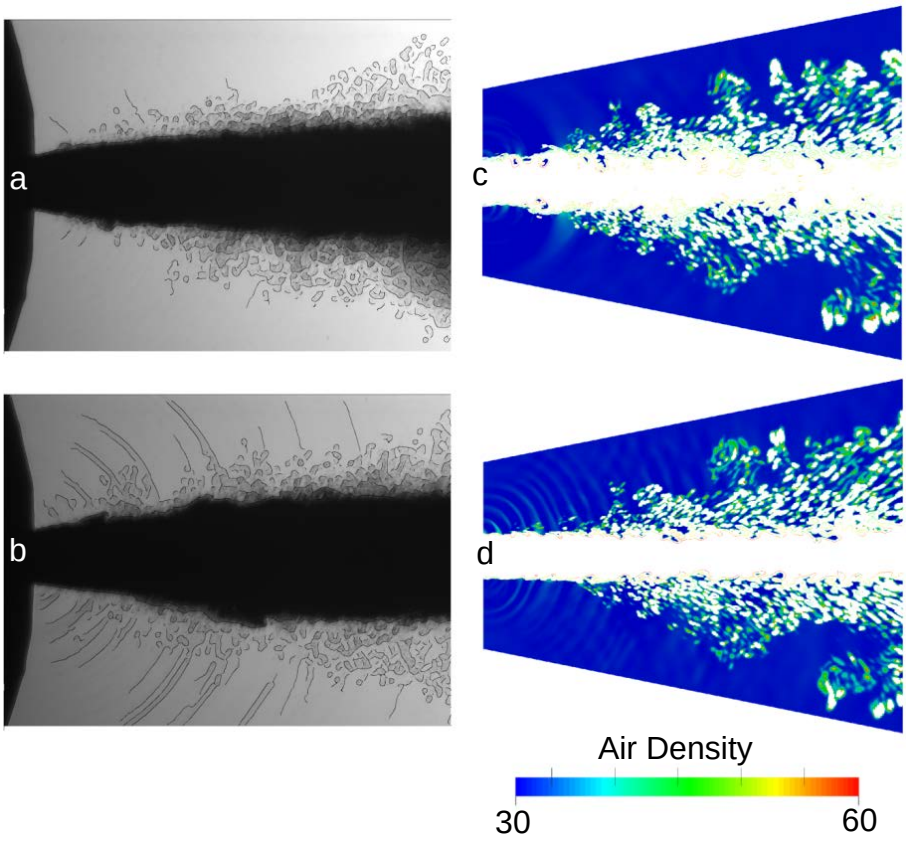

Figure 3-19. The onset of shock waves. The frames a and b (first column) are the montaged experimental images and an edge detection procedure applied to the experimental results. The frames c and d, second column, illustrate the numerical results at 27 μs, and 37 μs ASOP, respectively. The white areas represent cells which have a liquid fraction greater than 0.1. The density range is adjusted to highlight the shock waves.

The method used for measurement of the interfacial velocity is similar to that employed by Hillamo et al. [100]. It is assumed that the shock waves are initiated at disturbances on the interface between the liquid jet and the chamber gas where the interface velocity exceeds the local speed of sound. The Mach number, Ma of the jet interface may be derived from the angle of the shock wave relative to the interface, α, from the relation $Ma = 1/\sin \alpha$. Ma is defined as the ratio of the interface velocity to the local speed of sound in the gas phase [117]. The local speed of sound in the chamber gas at the test conditions of 298 K and 30 bar is about 348 m/s. The Ma applicable to each shock wave in the experimental images is calculated and the results are shown in Figure 3-20 and 3-21 against axial distance from the nozzle. Errors involved in the shock waves angle measurement basically originate from the method applied for drawing each line of the angle. One line of this angle indicates the interfacial surface of liquid-air and another line is the shock wave tangent. The main error in this measurement corresponds to the averaging approach used to draw the edge representing the interfacial surface. The value of this error decreases further downstream as the deviation of the averaged line from exact interfacial edge diminishes due to the lesser interface instabilities. Figure 3-20 shows data for various times ASOP during the spray transient, while Figure 3-21 shows data for a single shot during the quasi-steady stage ($P_{injection}$ = 1200 bar).

For comparison with the experimentally derived interface velocity, the computed interface velocity is extracted from the outer isosurface of the jet with 0.5 liquid fractions. This interface velocity is also plotted in Figure 3-20 and Figure 3-21. For the numerical results, the location of the shock waves imaged in Figure 3-19 correspond to peaks of computed interface velocity in excess of Ma = 1 shown in Figure 3-20. At 27 μs ASOP, the Ma of three experimentally imaged shock waves, shown in Figure 3-19a, are measured and plotted in Figure 3-20. At 32 μs ASOP, the number of shock waves captured increased which is evidence of an increase in the liquid jet velocity. The occurrence of shock waves is extended to 3.8 and 7.5 nozzle diameters downstream for experimental and numerical results respectively. At 37 μs ASOP, an increase in the number and extent of the shock waves is captured both in the experimental and numerical results.

The main source of deviation between experimental and numerical results could be related to not only the different calculation method but also the accuracy of the experimental shock wave capturing technique which employed backlit imaging. This technique suffers from obscuration by the cloud of fine droplets surrounding the spray.

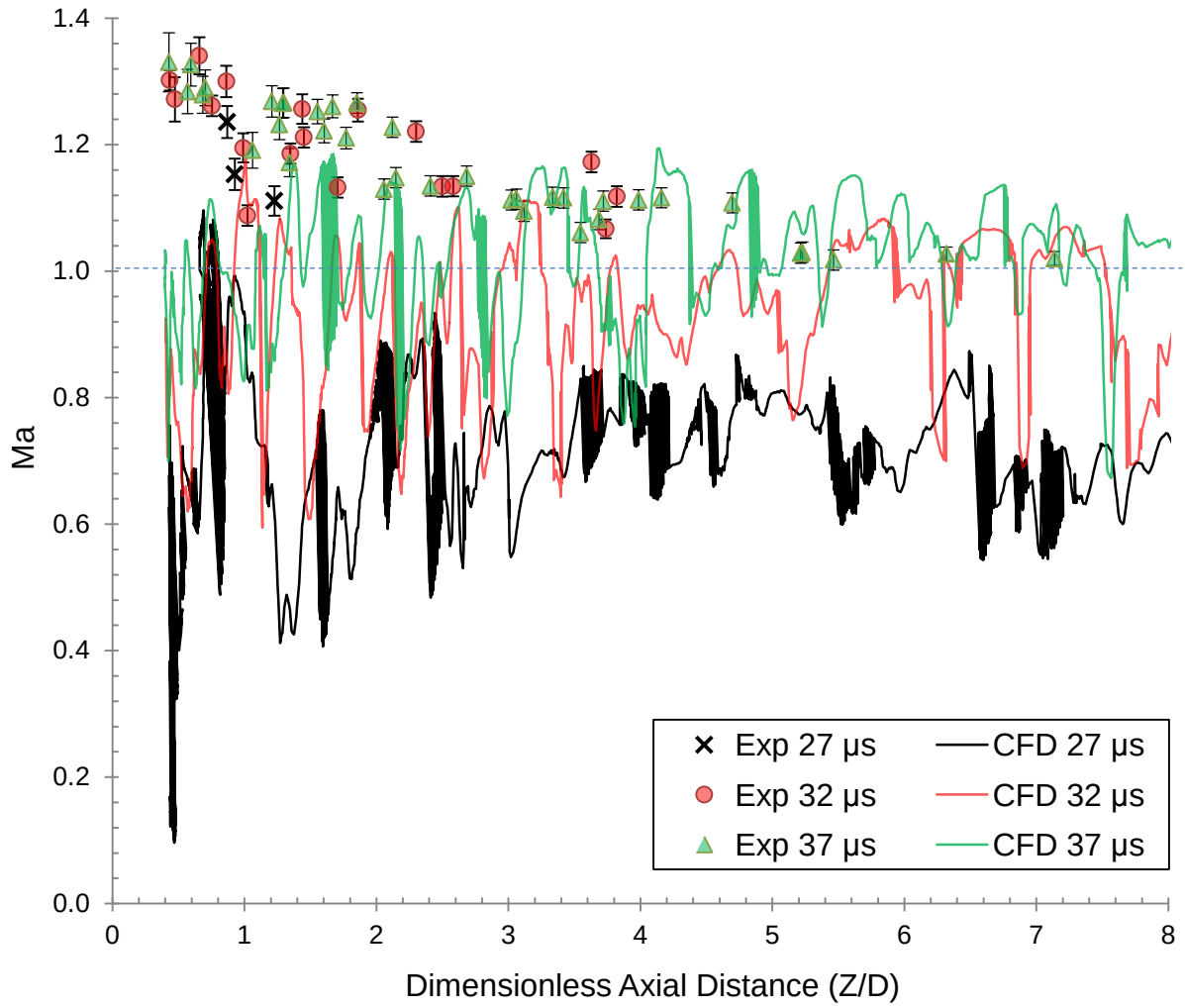

Figure 3-20. Experimental and numerical liquid-gas interface Mach number against axial distance from the nozzle exit, at various times ASOP. As the jet accelerates, the number of shock waves increases. The jet velocity has not yet reached steady stage.

As shown in Figure 3-7, sometime after the opening transient, at around 45 µs ASOP, the modelled nozzle exit velocity approaches the quasi-steady stage. At this stage, the shock waves are captured furthest downstream as demonstrated in Figure 3-21. The numerical jet interface velocity is high enough to generate the shock waves all the way downstream. Based on the jet diameter and liquid density, Weber number of the liquid-gas interface (We_l) is calculated, varying from 0.5×10^6 to 2×10^6. The fluctuation in the jet interface velocity both in experimental and numerical results thought to be due to surface instabilities on liquid-air interfaces.

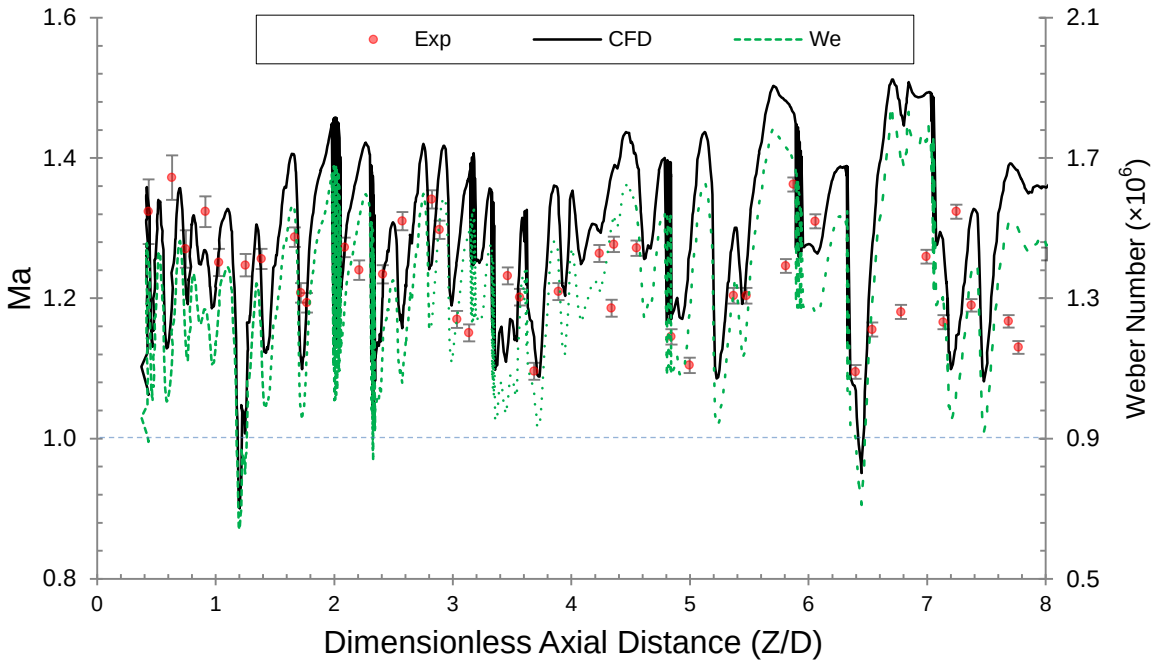

Figure 3-21. Experimental and numerical liquid-gas interface Mach and Weber number against axial distance from the nozzle exit after the jet has reached the quasi-steady stage ($P_{injection}$ = 1200 bar). Based on the jet diameter, Weber number is calculated which is in the range of $0.5\times10^6 \leq We_l \leq 2\times10^6$ ($12\times10^3 \leq We_g \leq 48\times10^3$).

3.4 Conclusions

The early stage of diesel spray dynamics is investigated experimentally and numerically employing microscopic backlit imaging and Eulerian/LES/VOF modelling respectively. Compressibility, temperature and cavitation effects for the liquid phase are included in the numerical model.

Mesh independency tests are conducted. Mean jet velocity, total pressure at nozzle exit and average radial profiles of velocity and mass fraction in the nozzle show tendency to convergence for the finest grid. At the quasi-steady stage, predicted mass flow rate matches experimental mass flow rate within experimental error. Comparison of measured penetration velocity of the jet between more than 100 consecutive shots and numerical results shows good correlation.

The effects of cavitation and in-nozzle turbulence on the growth and disintegration of surface structures on the emerging jet are characterised providing insight into the physics of primary atomisation. At the start of penetration, an umbrella-like leading edge is captured in both the numerical and experimental data however only the experimental images demonstrate a semi-transparent cloud of air-fuel mixture at the leading edge. Initially, toroidal streamwise waves

develop on the jet surface, travel downstream towards the leading edge umbrella and grow in magnitude until disintegrating in the wake. Subsequently, the emergence of longitudinal spanwise waves from the nozzle is accompanied by the disintegration of the toroidal streamwise waves, production of hairpin vortices and radial expansion of the jet mixing layer.

The first published experimental images of a starting vortex close to the nozzle exit at the start of injection, correlated with numerical results, are reported. The appearance of the starting vortex close to the nozzle exit before fuel penetration is taken as evidence of air inclusion in the nozzle. The location and velocity of the starting vortex are investigated experimentally and numerically. The vortex propagates downstream at about 40% of the jet penetration velocity

The onset and development of shock waves is presented experimentally and numerically and the jet interface velocity is inferred from the shock wave angle. This comparison shows good agreement between experimental and numerical results. The numerical results support the conclusion that shock waves occur where the jet velocity at the interface with the surrounding air exceeds the local speed of sound.

In order to cover the entire cycle of an injection, future studies could be directed to achieve a clearer insight into the physics involved during and after the end of injection process.

3.5 Acknowledgment

This work was supported by the Australian Maritime College and the Defence Science and Technology Group of Australia. We would like to acknowledge the use of the high performance computing facilities provided by the Tasmanian Partnership for Advanced Computing (TPAC) funded and hosted by the University of Tasmania. The authors express their gratitude to Luciano Mason, Mohammadmahdi Abaei, Hongjiang Yu, and Rouzbeh Abbassi for their support and suggestions.

Chapter 4 :
End of Injection Processes in a Single Hole Diesel Injector

This chapter has been submitted to the journal "Fuel" and at the time of writing is under review. This chapter has been modified to eliminate the repetition. The citation for the research article is:

M. Ghiji, L. Goldsworthy, P.A. Brandner, V. Garaniya, and P. Hield, 'End of Injection Processes in a Single Hole Diesel Injector', *Fuel*, [Under review, 2016].

Abstract

The end of injection processes in a single hole high-pressure diesel injector is investigated experimentally and numerically. Experimental measurements are performed using a laser-based backlit imaging technique. Numerical investigation of in- and near-nozzle fluid dynamics is conducted in an Eulerian framework using a Volume of Fluid interface capturing technique integrated with LES turbulence modelling. An incompressible non-cavitating and a compressible cavitating model are employed to gain a clearer understanding of the nozzle air ingestion mechanism at the end of injection. In the compressible model, a basic cavitation model is allowing liquid fuel to flash to gas at the fuel vapour pressure. The results show that upon needle valve closure the high energy core fluid maintains outward flow but the peripheral flow has reversed, as required by continuity, thus ingesting chamber air into the nozzle. The remaining unstable flow forms an asymmetry enhancing the air ingestion. Numerical results of the incompressible non-cavitating model show a single bubble of chamber gas remains embedded within the liquid in the nozzle hole only after velocities have largely dissipated. The results of the compressible cavitating model demonstrate how chamber gas is entrained into the sac volume through the air passage previously generated by hydraulic flip. These results provide an explanation of a mechanism for air ingestion at the end of injection recently described using X-ray imaging. This mechanism also provides a possible explanation for the presence of air within the emerging jet of subsequent injections.

4.1 Introduction

The fuel injection process in diesel engines governs the combustion process and emissions formation [24, 91]. The flow inside the nozzle and chamber experiences transient behaviours due to the intricate physics including: phase transition via cavitation [38, 70]; evaporation [118]; turbulence [119]; compressibility [70] and shock wave formation [11] and surface energy effects [25, 120]. Phenomena such as cavitation inside the injector have attracted scientific attention, including investigation of how different stages of cavitation (partial cavitation, super-cavitation, and hydraulic flip) can affect other conjunct mechanisms and consequently the spray dynamics [32, 39, 42]. Fundamentally, various stages of cavitation can be achieved by altering the injector design and operating conditions. For nozzles with small length-to-diameter ratios, super-cavitation and hydraulic flip can occur [38, 39]. In the latter case, the liquid fuel which has detached at the nozzle inlet is separated from the walls throughout the entire nozzle passage is subjected to liquid core contraction at the nozzle exit relative to the nozzle size [45, 70]. The penetration of high-pressure ambient gas into the passage (between liquid core and nozzle wall) induced by super-cavitation, diminishes the boundary layer disturbances and ultimately diversifies the overall spray dynamics [38, 40, 121].

An injection event consists of three stages: an opening transient associated with needle valve lift and concurrent emergence of the liquid jet from the nozzle; quasi-steady injection at maximum pressure during which the major fuel mass is delivered; closing transient or end of injection (EOI) flow processes associated with needle valve closure. The former two stages of an injection are well discussed in the authors' earlier studies [109, 122]. The focus of this article is devoted to understanding more challenging phenomena occurring at the EOI.

A pioneering study by Yu *et al* [123] revealed the significance of the nozzle design and EOI features on air-fuel mixture quality and consequently how the existence of a low-speed fuel jet at EOI led to the formation of unburnt hydrocarbons in diesel engines. Later on, the optical investigations of Bruneaux [17] demonstrated a considerable formation of unburnt hydrocarbons at poor fuel-air mixture regions after EOI. Detailed studies by Musculus demonstrated not only how the needle closure rate could influence the mixture quality [124], but also how associated physics in the EOI process could influence the soot production and combustion in diesel engines [23]. Moreover, recent measurements of the early stages of injection in a high-pressure spray chamber by the authors [109, 125] have suggested that the transparency of the emerging jet at Start Of Injection (SOI) is due the presence of air in the first injected fuel, which is likely to be

due to the air ingestion at the EOI of the previous shot. This air ingestion at EOI affects the fuel penetration and evaporation rate of the next injection event specifically during the first 100 μs after SOI [31] which subsequently leads to partial combustion and ultimately increase in the production of pollutants [12, 83, 126]. These drawbacks have motivated many researchers to investigate, comprehend and finally optimise the parameters and physics associated with EOI process. Details of these extremely transient phenomena and their corresponding effects are challenging subject and yet to be fully understood.

The x-ray radiography experiments of Kastengren *et al* [127] at the EOI event demonstrated an entrainment wave traveling with velocity magnitude of several hundred metres per second in the low-density regions of the chamber, in qualitative agreement with Musculus *et al* [23, 124]. This entrainment wave dilutes the spray and widens the spray angle in the region close to the nozzle exit at the EOI. Additionally, a decrease in fuel mass flow rate due to the needle valve closure enhances the dilution process. X-ray imaging of the closing transient in a diesel injector by Swantek *et al* [12] depicts some gas bubbles ingested in the nozzle hole and sac. They proposed that the bubbles are due to air ingestion rather than cavitation in the bulk fluid. Further studies [12, 22, 27, 28] provided a better understanding of the influence of factors such as nozzle hole size, rail injection and spray chamber pressure on the air ingestion mechanism during the EOI process.

With the aid of numerical analyses a clearer insight into the key parameters of each process at EOI can be achieved [27, 36, 70]. Turbulent flows induced inside and near a high-pressure injector can be represented by eddies with a wide range of length and timescales. These eddies could be resolved entirely using the Direct Numerical Simulation (DNS) approach, however, the high computation time required for the high Reynolds numbers occurring in diesel sprays make DNS unfeasible. In Large Eddy Simulation (LES) approach, large-scale eddies containing more universal energy are resolved while small-scale eddies are modelled by a turbulence model. Thus, LES is less computationally expensive compared to the DNS but more computationally expensive to the Reynolds Averaged Navier-Stokes (RANS) approach. This is due to the generally finer spatial resolution needed for LES models in comparison to the much finer grids for RANS models. RANS models is subjected to inaccuracy in capturing the transient behaviours due to the diminishment of some features of the transient spray structures and the sharp interfaces [2, 33]. In order to capture the transient features of interfacial surfaces, some numerical techniques reconstruct the liquid-gas interfaces by tracking them explicitly such as the Volume Of Fluid (VOF) [128] or Level-Set [129] approach while other techniques utilise a

diffuse-interface modeling approach where the interfaces are not explicitly trackable and only partially resolved by a high-resolution grid [25, 27]. The importance of explicit tracking of interfaces on the growth of interfacial instabilities [23, 124] has been neglected in the recent investigation of the EOI process by Battistoni *et al* [27]. Battistoni *et al* [27] shed light on the physics associated with the EOI by modelling Swantek *et al's* [12] non-cavitating nozzle in an Eulerian LES framework. They outlined that the upward moving pressure waves at the EOI lead to the air ingestion and ultimately liquid evacuation of the entire nozzle. Papadopoulos and Aleiferis [83] modelled a low pressure (400 bar) partially cavitating nozzle through one hole of a multi-hole injector and found that the air trapped inside the nozzle is due to the high inertia of the internal flow exiting the nozzle at EOI.

The present study focuses on the experimental and numerical investigation of the EOI processes in a single-hole sharp edged nozzle. Two numerical models, an incompressible non-cavitating and a more sophisticated compressible cavitating model are employed. A key aim of the present work is to achieve a better understanding of the gas ingestion mechanism during the EOI process. The effect of various spray chamber pressure (1, 10, 20, and 30 bar) and needle valve closure rate on the air ingestion mechanism are discussed.

4.2 Methodology

Experimental measurements are compared with the numerical results at EOI. The experiments utilise a microscopic laser-based backlit imaging (shadowgraphy) technique in a constant volume High-Pressure Spray Chamber (HPSC). Numerical investigations are conducted by applying the VOF phase-fraction interface capturing technique in a LES framework using an Eulerian multiphase model. In the incompressible model, the influences of compressibility and phase change have been neglected in order to conduct an evaluation on key driving parameter on air ingestion process. In the compressible model, the effects of temperature, compressibility of each phase, generation and development of cavitation have been included in the numerical model, enabling the investigation of more complex physics associated with the EOI process. Cavitation of the fuel is allowed at a predefined vapour pressure. Enhanced cavitation inception due to nuclei, re-condensation of fuel vapour and the presence of incondensable gases are not modelled.

4.2.1 Experimental Apparatus

The backlit imaging technique utilised here is shown schematically in Figure 2-1. This technique is less complicated and more accessible than the X-ray phase contrast technique but still gives valuable data on the spray morphology. The experimental measurements can be employed as a benchmark for evaluating and then validating the numerical results. The measurements by Swantek *et al* [12] and measurements in the present are for injection into a constant volume HPSC at ambient temperature, with chamber gas densities representative of those in an engine at injection. Detailed specifications and dimensions of the spray chamber are available in Goldsworthy *et al.* [84, 103]. Diesel fuel is injected from the top of the spray chamber axially through a single-hole solid cone fuel spray with an adjustable injection pressure up to 1200 bar.

The tip of the injector protrudes about 140 nozzle diameters (35 mm) from the ceiling of the chamber and the side walls are 240 nozzle diameters (60 mm) from the nozzle tip. Therefore, the effect of the surrounding chamber walls is not significant. A continuous flow of air evacuates droplets from previous injections. The mass flow rate of flushing air has been adjusted to minimise turbulence generation. This was achieved by closing off the flashing airflow and investigating the shot-to-shot variations on spray morphology. In addition, an interval of about 30 seconds between injections lets the gas in the chamber settle.

The injection pressure profile is highly repeatable from shot to shot. The injector needle valve snaps open when the injector pressure achieves a certain value, as determined by the adjustable tension on the needle valve spring. The needle lift is monitored using an eddy current proximity probe. The needle lift transducer indicates that it takes about 200 μs for the needle valve to achieve the total lift of 200 μm. A Kistler piezoelectric pressure transducer sampled at 10 MHz is used to monitor the pressure of the fuel supplied to the injector. The high-pressure fuel pulse is generated in a modified hydraulic electric unit injector. A 120 mJ dual-cavity Nd:YAG laser is used in combination with a solid state diffuser. Light pulses of duration around 10 ns are achieved. A Questar QM100 long distance microscope is attached to a LaVision Imager Intense dual-frame, 12 bit CCD camera with 1376 × 1040 pixel resolution with the capability of capturing image pairs with variable inter-frame times as low as 1 μs for each shot of the injector. The camera is focused, aligned, and calibrated on a graduated scale on the spray axis. Data acquisition is initiated at a pre-set threshold of fuel pressure, with an adjustable delay to the acquisition of the images.

4.2.2 Numerical Approach

4.2.2.1 Mathematical Method

To get a clearer understanding of mechanisms associated with the EOI process, Computational Fluid Dynamic (CFD) modelling was employed using the VOF phase-fraction based interface capturing technique in OpenFOAM v2.3 [130]. The CFD models are solved using the LES approach in an Eulerian framework. Full details of the mathematical method for the incompressible model are presented in the authors' earlier work [109]. The incompressible model uses the OpenFOAM solver *InterFoam*. The liquid-gas two-phase fields are modelled as a continuum with variable density and viscosity, which can be discontinuous across the phase interfaces. Surface tension forces are included to preserve local curvature of the interface. The compressible model, which uses *compressibleInterFoam*, is described in detail in Section 3.2.2.1.

4.2.2.2 Numerical Solution Method

Numerical solution method is descried in Section 3.2.2.2.

4.2.2.3 Boundary Conditions and Initial Set-up

Injector geometry plays an important role in diesel spray dynamics [25, 47, 75], hence X-ray Computer-Aided Tomography (CAT) was employed to extract the actual internal geometry of the injector. The computational domain based on CAT analysis was created as illustrated in Figure 3-1.

Due to limited computing resources, only the portion of the spray chamber where the primary atomisation occurs was modelled. The computational domain, shown in the middle of Figure 3-1, is discretised using a structured hexahedral mesh of 8×10^6 cells. The mesh dependency and numerical scheme sensitivity study have been demonstrated in Ghiji *et al* [109, 122]. The quality of LES model has been discussed and a deviation of 1.1% has been reported between the 8×10^6 and 20×10^6 cells cases [122]. All the experimental conditions described in [109] were replicated in numerical models including the sac volume inlet, spray chamber pressure, air and diesel fuel temperature and viscosity. These experimental conditions and fuel properties and are summarised in Table 3-1.

The sac, orifice, and primary atomisation area meshed with grid size down to 1.2 μm on average in the nozzle. The boundary layer is modelled using no-slip condition on the walls and high grid resolution in the boundary layer region. The finest cells on the nozzle wall are 0.1 um with an expansion rate of 1.05. The nozzle and sac walls are adiabatic. A constant pressure boundary was applied at the outlet of the meshed volume as well as the boundaries on the sides of the meshed volume beyond the nozzle tip. This boundary allows air entrainment into the spray chamber. The grid resolution at each region, time-step range, number of CPUs, and computational cost (wall clock time) for a total simulation time of 2 ms for both incompressible and compressible simulations are summarised in Table 4-1. It can be seen that the compressible model requires about 9 times the computational time of the incompressible model, so there is value in comparing the predictions of the two models.

Table 4-1. Summary of mesh and computation parameters for numerical models. Total simulation time is 2 ms.

Case	**Average Spatial Resolution (μm and cells/D)**			**Cell count**	**Time Step ($\times 10^{-9}$ S)**	**CPU (core count)**	**Wall clock time (hours)**
	Sac	Orifice	Chamber				
incompressible	7.5 (55/**D**)	1.2 (210/**D**)	5 (50/**D**)	8×10^6	$1 \leq \Delta T \leq 90$	480	78
compressible					$0.6 \leq \Delta T \leq 3$		711

To mimic the sudden closure of the needle valve, the EOI process is initially simply modelled by immediately changing the boundary condition at sac entrance from a pressure inlet boundary to a wall with no slip condition with no ramp. In Section 4.3.1.3 the effect of less severe closure is investigated by imposing a ramped pressure profile at the EOI.

In order to take into account the significance of in-nozzle generated turbulence on primary atomisation [48, 75], the size of the cells in the nozzle is of the order of the Kolmogorov length scale $\eta = (\upsilon^3/\varepsilon)^{1/4}$ where ε is the average rate of dissipation of turbulence kinetic energy per unit mass. The smallest length scales associated with the flow field for the fully developed spray are reported in Table 4-2. It can be seen in this table that η_l in the nozzle is similar to the mesh size. This mesh resolution enables reasonable prediction of small eddies of the liquid phase inside the nozzle. It was not possible to achieve mesh scales below the Kolmogorov length scale for the gas phase demonstrating the necessity for employing a sub-grid scale model to include turbulence effects in the gas phase.

Table 4-2. Kolmogorov length scales for the liquid and gas phases of the developed spray where the turbulence intensities used are 4.4 % and 10 %, respectively.

Parameter	Value (μm)
Liquid phase Kolmogorov length scale, η_l	0.7
Minimum mesh size in nozzle hole for fine case, Δx_{min}	0.1
Gas phase Kolmogorov length scale, η_g	0.1
Minimum mesh size in spray chamber for fine case, Δx_{min}	1.7

The ratio of resolved turbulent kinetic energy (k_{res}) to total turbulent kinetic energy (TKE = k_{sgs} + k_{res}) indicates the quality of the LES model and consequently the adequacy of the overall grid fineness [33, 110]. For satisfactory LES modelling this ratio should be more than 80% [110]. The resolved turbulent kinetic energy is calculated over 10 μs at a probe point located at 4D (1 mm) from the nozzle exit. The overall ratio of k_{sgs} to TKE predicted by the sub-grid scale turbulent model at the quasi-steady stage is equal to 6%. In addition, the numerical turbulent diffusion due to the discretization error is the same magnitude as the turbulent diffusion computed by the sub-grid scale model [33, 110]. Thus, at the quasi-steady stage, the resolved turbulent kinetic energy is calculated at 88% of total TKE indicating a satisfactory LES model.

4.3 Results and Discussions

The experimental images just before and after the start of penetration; image a and b in Figure 4-1, show a toroidal vortex in the chamber air around the tip of the emerging fluid (see also [122]). This structure is apparent due to the density gradients in the chamber air, inherent in the toroidal flow. Furthermore, numerous experimental images show the vortex very close to the nozzle exit, prior to the emergence of liquid. This is thought to be due to the presence of air in the nozzle, with the air being ejected before the fuel and thus creating the shear-induced vortex as seen in Figure 4-1a. This initial air slug seen experimentally is taken as further evidence of the existence of air in the nozzle prior to injection. In addition, the two successive frames with 1 μs inter-frame time, images c and d in Figure 4-1, illustrate how a dense liquid jet travels further downstream catching up with the transparent 'umbrella-like' leading edge. It is apparent that the leading edge of the spray contains gas, contrary to what would be expected if the nozzle was full of liquid fuel prior to injection. While it is possible that the mixing of gas into the leading edge is entirely due to the unsteady conditions at the Start of Penetration (SOP), the modelling

presented here suggests that physics associated with EOI process from the previous injection play a significant role in topology variation of the subsequent penetrating jet.

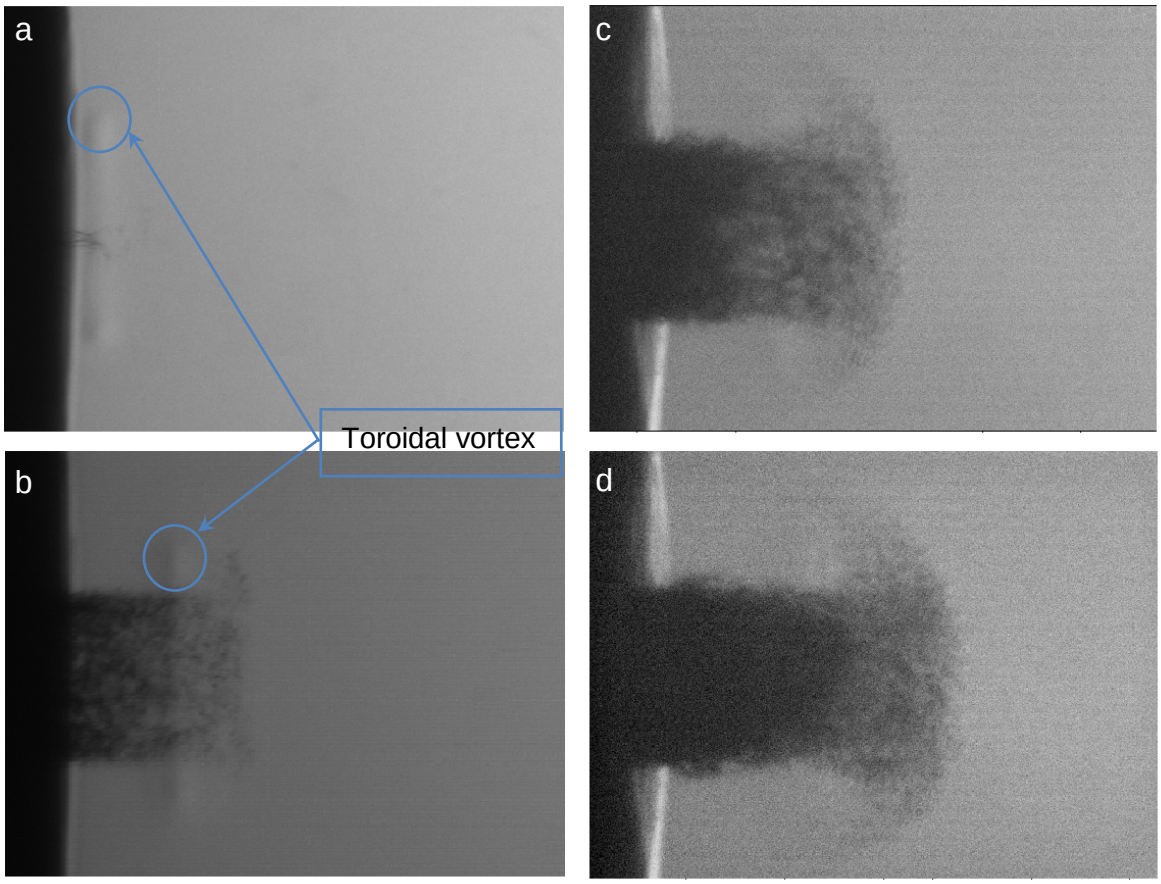

Figure 4-1. Magnified shadowgraphy images of the start of penetration at conditions described in Table **3-1**. Image a and b are captured from two different injection shots showing the occurrence of the toroidal vortex before and a few microseconds after the start of penetration (ASOP). The presence of the toroidal vortex proves the existence of air inside the nozzle-hole. Images c and d are paired taken from two consecutive frames with 1 μs inter-frame time (c: 4 μs and d: 5 μs ASOP). It is apparent that the leading edge of the spray contains gas, contrary to what would be expected if the nozzle was full of liquid fuel prior to the start of injection.

To get a clearer insight into the phenomena associated with the EOI process, an incompressible non-cavitating model and a compressible cavitating model were employed. Both the compressible and incompressible EOI simulations show the nozzle partially filled with gas sometime after the EOI, with an intricate interface between the liquid and gas, representing the existence of gas bubbles.

4.3.1 Incompressible Model

The experimental and numerical results are qualitatively compared in Figure 4-2. Just before EOI at the quasi-steady stage of injection, the chamber pressure is 30 bar and the sac pressure is 1200 bar (120 Mpa). The measured early spray angle, shown in Figure 4-2a, is in good agreement with the numerical results, given in Figure 4-2c, at the quasi-steady stage [109, 125] before the EOI. The timing of Figure 4-2b is not precisely determined but from the results of numerous shots at the EOI, it is apparent that it represents the early stages of spray breakdown after needle valve closure. Numerical results are shown in Figure 4-2c and 4d, for just before and 1 μs after needle valve closure respectively illustrating narrowing of the liquid jet near the nozzle exit associated with high negative axial velocity near the nozzle exit, the onset of the air entrainment process into the nozzle orifice and consequent liquid detachment from the nozzle walls near the exit. Figure 4b shows the jet narrowing near the nozzle exit. Further experimental images presented in Section 4.3.1.4. show the jet narrowing at the nozzle exit, widening further downstream and eventually extensive ligament formation. The simulation does not capture the spray widening to the extent seen in the experiments. Shock waves are not captured with the incompressible model. Shock waves analyses using the compressible model are quantitatively compared with experimental measurements in authors' earlier study [122].

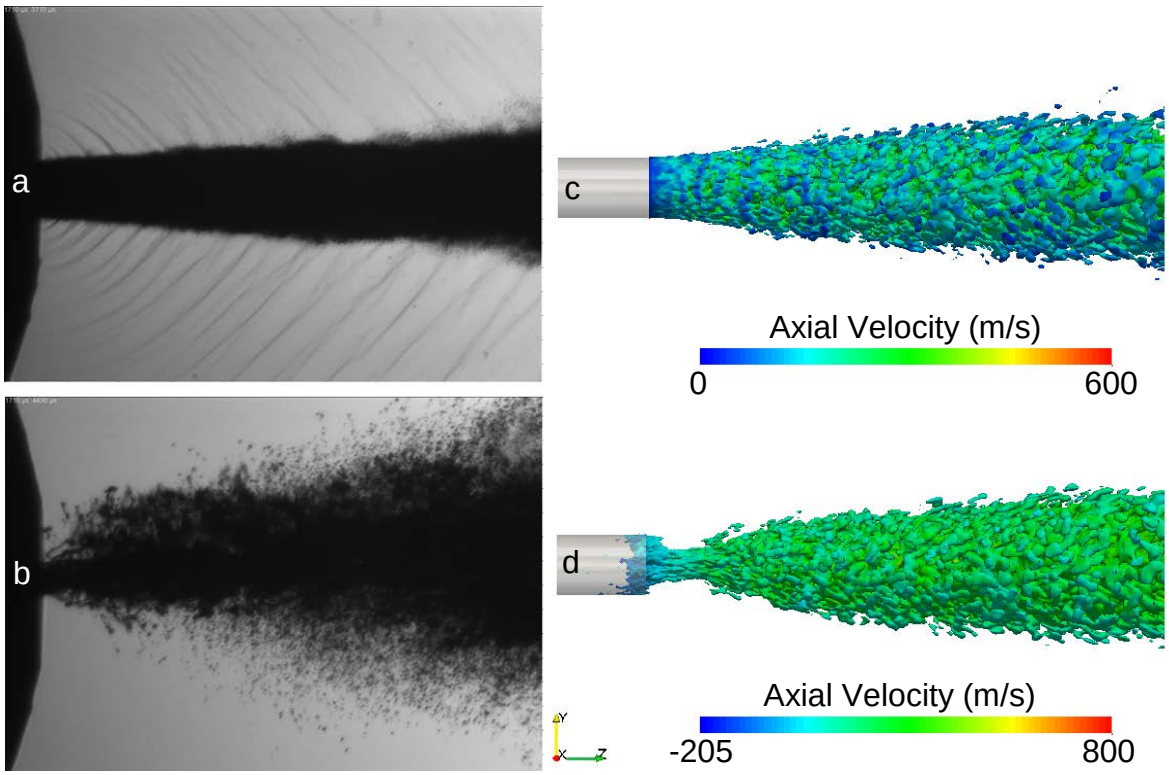

Figure 4-2. Comparison of experimental and numerical results for just before (images a and c) and after (images b and d) the needle valve closure. Numerical results show the structure of liquid jet coloured by axial velocity at before (c) and 1 μs after (d) needle valve closure, indicated by iso-surface of volume fraction $\gamma = 0.1$. Images (b) and (d) show narrower ligament exiting the nozzle orifice. High negative axial velocity captured, at (d), just after the EOI demonstrates the commencement of air ingestion process to the nozzle orifice.

Numerical results for the period from just before the EOI to near zero nozzle flow are summarised in Figure 4-3. Figure 4-3a, shows the development of a negative pressure at the nozzle inlet due to the convergence of the flow from the sac into the nozzle. The incompressible model does not include cavitation but cavitation would be expected in this negative pressure region [131]. This simulation gives results that would be similar to the case of a converging nozzle with rounded inlet edges to avoid cavitation [32].

The mean velocity at the end of nozzle exit is 395 m/s. It is apparent from the velocity plots that the boundary layer and fine turbulence scales in the nozzle are qualitatively resolved. The Liquid Volume Fraction (LVF) panel shows the onset of spray breakup in the chamber. Just 1 μs after needle closure (Figure 4-3b), the sac and nozzle pressures are mostly negative, due to the inertia of the fluid in the nozzle. This indicates the potential for transient cavitation in this phase of the EOI process. The high energy fluid on the nozzle axis retains outward velocity with significant reverse flow apparent along the nozzle walls, as required by continuity. The narrowing of emerging jet and air ingestion around the periphery of the nozzle exit are apparent. The onset of the air entrainment process into the nozzle orifice and consequent liquid detachment from the nozzle walls near the exit are followed by the onset of strong instabilities in the liquid/gas interface. By 5 μs after needle closure (Figure 4-3c), the main jet is dissipating and significant air ingestion has occurred. At this stage an asymmetry in the arrested flow at the liquid/air interface forms, enhancing the initial air ingestion. The asymmetry is apparent in the plots of void fraction, velocity, and pressure. By 50 μs after needle closure (Figure 4-3d), ingested air has moved into the nozzle, displacing fuel. This displacement of liquid appears similar to the well-known post injection dribble phenomenon. Negative velocities are still apparent in the nozzle. By 400 μs after needle closure (Figure 4-3e), where nozzle velocities are near zero, a distinct bubble has formed in the nozzle. The interface between the liquid in the nozzle and the chamber gas is within the nozzle rather than at the junction of the nozzle and chamber.

Beyond the ingestion of chamber gas into the nozzle, Swantek *et al's* experiments [12] show gas bubbles also forming in the sac volume. These are not captured with the present incompressible simulation, thought to be due to the lack of cavitation model. Battistoni et al [27] study showed very low pressures developing in the nozzle and near the needle seat after needle closure and the consequent onset of cavitation in these areas. However, these vapour cavities eventually disappear due to condensation as the pressure rises, and ultimately the presence of air in the nozzle is due to ingestion. Swantek *et al* [12] asserted that the presence of bubbles in the nozzle and sac is due to air ingestion rather than cavitation. Their measurements were for the same nozzle as modelled by Battistoni *et al* [27], i.e. convergent with rounded inlet edges so no cavitation was apparent prior to needle closure.

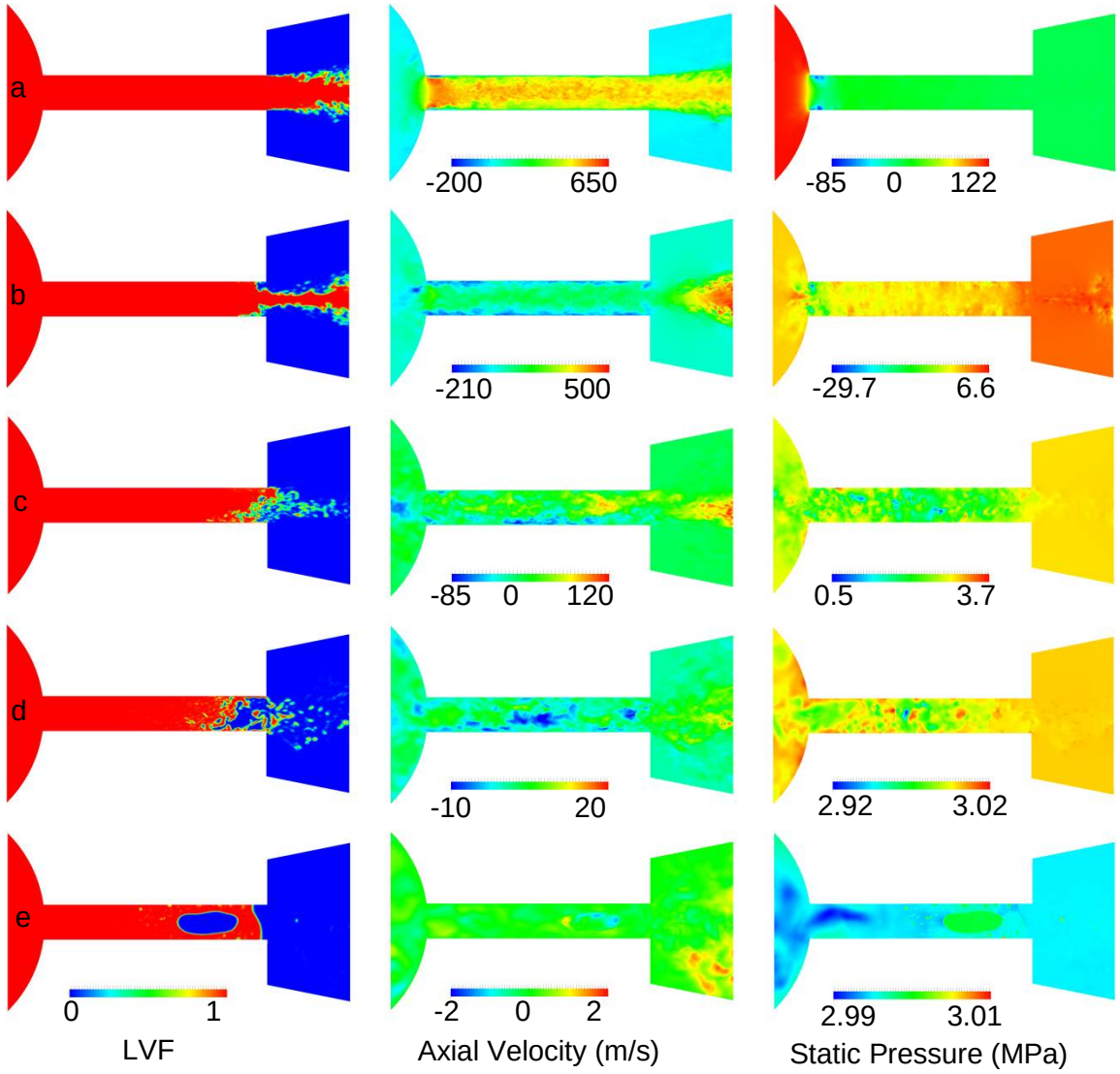

Figure 4-3. Zoomed cross-sectional view of Liquid Volume Fraction (LVF), axial velocity and static pressure at (a): before needle valve closure, (b): 1 μs, (c): 5 μs, (d): 50 μs and (e): 400 μs after needle valve closure. Just prior to closure salient features of the flow include the developed turbulent boundary layers

within the nozzle and the negative pressure at the entrance that would produce cavitation if modelled [131]. Just after closure the high energy core fluid maintains outward flow but the peripheral flow has reversed, as required by continuity, thus ingesting chamber air into the nozzle.

While this is an incompressible simulation and compressibility will play a significant role in this phenomenon, the present modelling illustrates a dominant mechanism of air ingestion. It is driven by the inertia of the high-velocity column of fluid in the orifice. At needle valve closure, the core of the column maintains outward velocity, while reverse flow occurs along the walls, as dictated by continuity. This asymmetric backward flowing liquid draws air into the nozzle exit region. Destabilization of the liquid surface and flow asymmetry formation lead to simultaneous regions of positive and negative axial velocity ultimately leading to air ingestion into the nozzle. These results demonstrate the importance of accurately capturing the air/fuel interface. The development of the surface instability and formation of a complex interface structure initiates the trapping of air within the liquid.

4.3.2 Effect of chamber pressure

The effect of chamber pressure on the incompressible simulations was tested by simulating 3 additional chamber pressures (1, 10, and 20 bars) as well as the previously discussed 30 bar. As shown in Figure 4-4 the chamber pressure has little or no effect on the final location of the gas bubble. The liquid inside the nozzle stabilises more quickly at higher chamber pressures due to less pressure imbalance. For all cases with various chamber pressures, equilibrium has been achieved at 2 ms after the needle valve closure. Similarly, Papadopoulos and Aleiferis [83] found that the time of stabilization reduces at higher chamber pressure. Contradictory Swantek *et al* [12] found that the chamber pressure does influence the amount and location of gas ingested significantly. Lower chamber pressure leads to greater jet velocity and thus higher inertia and consequently lower transient sac pressure. Without this jet inertia effect, the higher chamber pressure would sensibly lead to higher pressure gradients and thus more air inflow into the sac. The fact that the incompressible model does not show differences in ingested gas location and volume suggests that there are important dynamic effects associated with the compressibility and phase change of the liquid.

The incompressible model has some limitations. There is potential for other phenomena not modelled including cavitation at the nozzle entrance before needle valve closure leading to the incondensable gas formation (despite the short time scales) as an additional source of gas that may be ingested into the sac after closure. The low pressure that would form upon valve closure

may cause cavitation in the sac and around the needle seat and may be a further mechanism for the formation of incondensable gas in the sac. Pressure waves may also play a role in the overall dynamics of the fluid but have not been modelled in the incompressible model. Any incondensable gas that is present in the sac prior to the SOI may promote initial formation of standing cavities or super-cavities, depending on the cavitation number, leading to ongoing cyclic cavitation due to the inability of the system cycle to purge the incondensable gas.

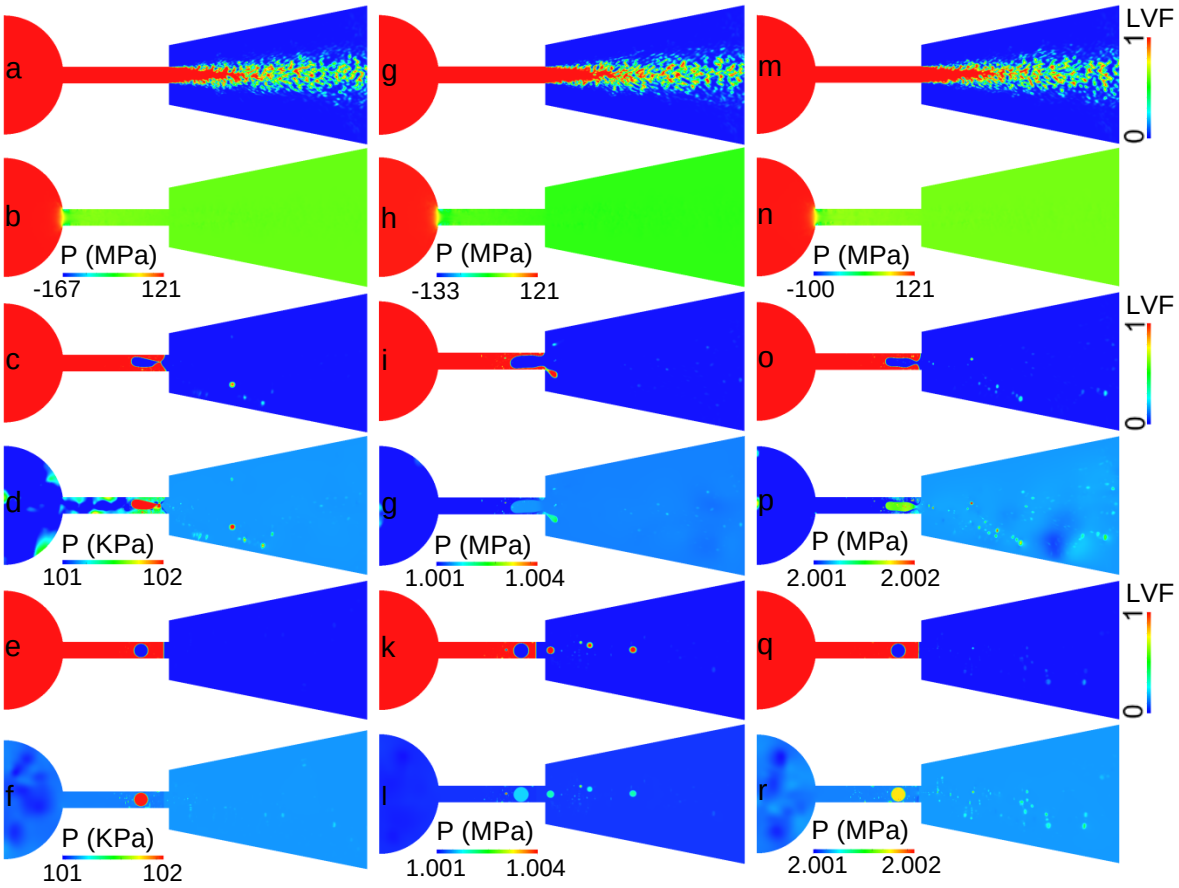

Figure 4-4. Cross sections of Liquid Volume Fraction (LVF) and static pressure at: just before (first and second row), 400 μs (third and fourth row), and 2 ms (fifth and sixth row) after needle valve closure. Equilibrium has been achieved at 2 ms after needle valve closure. The qualitative mechanism of air ingestion at various chamber pressures shows no significant differences in the location and volume of ingested gas.

4.3.3 Compressible Model

The numerical analysis of the EOI process is extended here by employing a more sophisticated model compared to the incompressible model where further physics such as phase change (cavitation), compressibility and shock wave effects are taken into account. Numerical

results from just before the needle valve closure up to 400 μs after EOI are summarised in Figure 4-5. Validation of the compressible simulation at the quasi-steady stage is shown in the authors' earlier study [122]. This compressible model considers the fluid density and temperature changes, liquid phase change through a simple cavitation model, and fluid compressibility effects.

The hydraulic flip (extension of cavities to the full length of the nozzle) that occurs at the quasi-steady stage of injection with sac inlet pressure of 1200 bar corresponding to the time just before the start of EOI process is shown in Figure 4-5a. The onset and development of shock waves initiated on air-fuel interfaces in the region very close to the nozzle exit can be seen in axial velocity panel of Figure 4-5a. This is in-depth described and discussed in Ghiji *et al* [122]. The numerical results do not demonstrate negative pressures (third column of Figure 4-5) because the density of the liquid can decrease to accommodate fluid extension, with the ultimate result of phase change in some regions. Further, with the occurrence of hydraulic flip, the pressure in the nozzle does not fall significantly below the chamber pressure because of the open passage into the cavity. At 20 μs after needle valve closure, Figure 4-5b, the shear layer between the liquid jet inside the nozzle and the chamber air moving at a significant velocity in the opposite direction appears to induce surface instabilities on the liquid surface which grow downstream and into the chamber. The axial velocity panel of Figure 4-5b shows very significant air inflow velocities (negative axial velocity of 128 m/s) at the nozzle exit. These instabilities appear to grow with time and with distance downstream, possibly leading to the eventual breakup of the jet into lower speed large ligaments in the chamber at 40 μs after EOI, shown in Figure 4-5c. By 60 μs after the EOI, Figure 4-5d, the liquid jet in the nozzle has dissipated completely and the dominant flow is the air from the chamber moving upstream. At this stage, the air/liquid interface becomes more chaotic. The static pressure plots show that at no stage after needle closure does the liquid pressure fall below the liquid vapour pressure (1 kPa). This is in contrast to the results of Battistoni *et al* [27] where large vapour cavities are seen to form. The main reason for the difference is the existence of hydraulic flip in the present situation, which helps to maintain the liquid pressure. In nozzles without a hydraulic flip, the transient occurrence of large vapour cavities in the body of the nozzle liquid has a significant influence overall, but ultimately it is inertia that dominates the air ingestion process. At 60 μs onwards, Figure 4-5d-g, the chamber air is seen to penetrate into the sac, unlike the incompressible model. This is primarily due to the enhanced upstream movement of chamber air beside the liquid core all the way to the nozzle entrance from prior to needle closure. Later on (Figure 4-5e-g), the ingested

gases recirculate inside the sac due to the pressure differences between in-nozzle flow and gas chamber. By 400 μs small gas bubbles in the nozzle have coalesced into large bubbles.

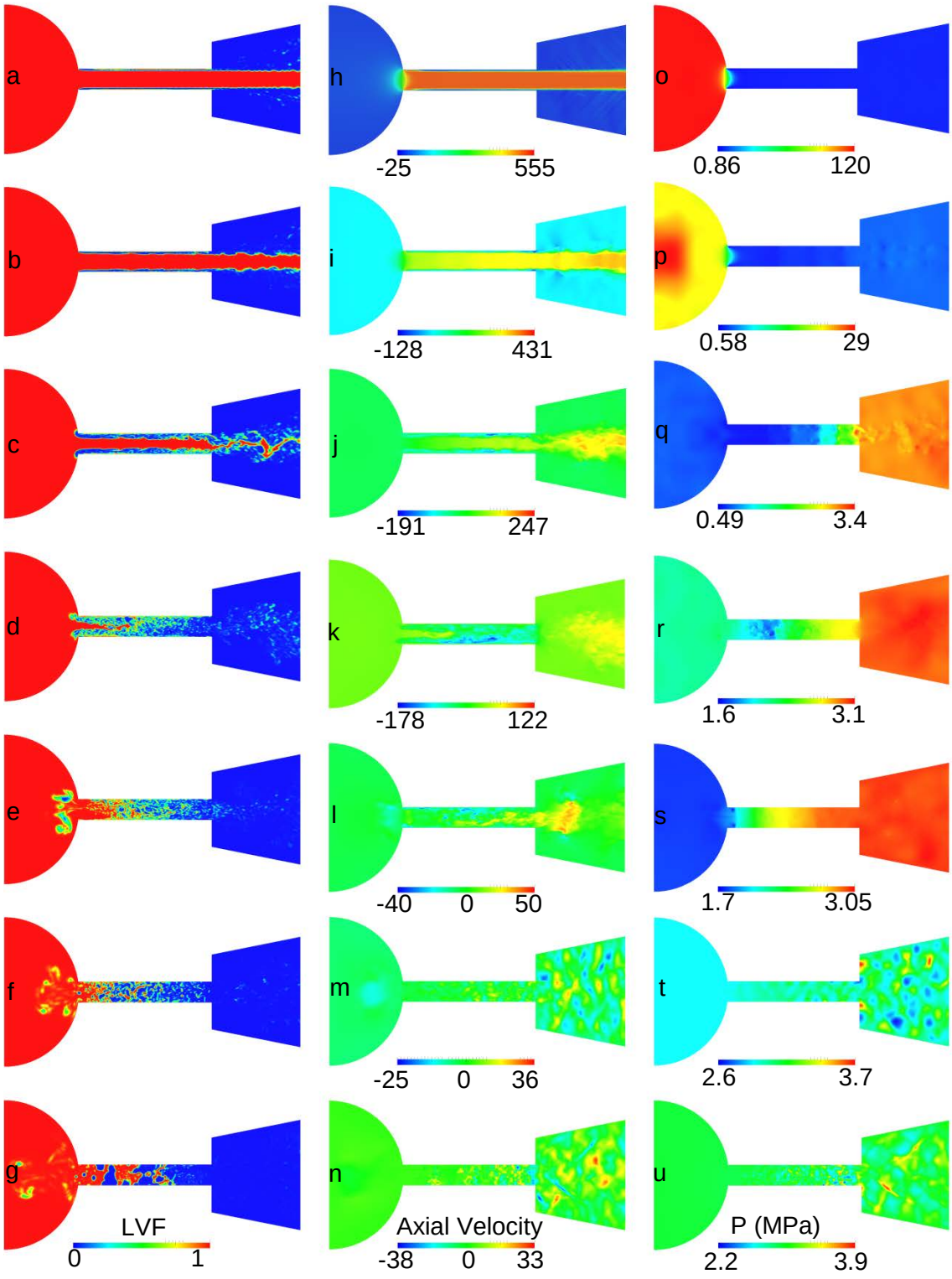

Figure 4-5. Zoomed cross-sectional view of Liquid Volume Fraction (LVF), axial velocity and static pressure at (a, h, o): before, (b, i, p): 20 μs, (c, j, q): 40 μs, (d, k, r): 60 μs, (e, l, s): 100 μs, (f, m,t): 200 μs, and (g, n, u): 400 μs after needle valve closure.

It can be concluded that, as with the incompressible model, it is the inertia of the liquid core and its arrest that is the driving mechanism of air ingestion with needle closure. In addition to the inertia effect, the presence of pressurised gas chamber in the nozzle wall cavity enhances the stretching process of the in-nozzle liquid. To satisfy continuity, chamber gas flows into the nozzle beside the liquid core through chaotic air/fuel interfaces, as also seen in the incompressible model.

4.3.4 Effect of needle valve closing severity

The influence of the needle valve closure severity on the EOI process is investigated for both incompressible and compressible models by implementing a closing ramp profile where the sac inlet pressure drops from 1200 bar to 30 bar in 10 μs. This ramp pressure profile is roughly defined by correlating the stabilization time reported by [27, 28, 83] where the needle valve movement has been modelled using a linear displacement profile. A more severe closure scenario is selected here to compensate for any possible dissipation of transient physics induced using diffusive numerical schemes [27]. The results show no significant differences compared to the immediate pressure drop, presented in previous sections.

In the absence of experimental data that correlates the rail pressure with sac pressure during needle valve closure and conclusively establishes the rate of arrest of the inflow into the sac, this field remains an ongoing challenge for researchers. Numerical investigation of needle bounce, wobble, and vibration during the EOI process can be another demanding subject which will provide useful information for injector designers.

4.3.5 Ligaments, dribble and large droplets at the EOI

Figure 4-6 depicts a sequence of experimental images, taken at various times just before and after the EOI process. The timing of the images in Figure 4-6 is not precisely determined but from the results of numerous shots at the EOI, it is apparent that the series shown represents the logical progression of spray development after needle closure. It can be clearly seen that just after EOI, the early spray angle is widening which is associated with the contraction of the emerging jet in the vicinity of the nozzle exit. Further reduction in the local spray density occurs due to a decrease in fuel mass flow rate, and enhancement of surface instabilities of the decelerating jet in advance of the air entrainment.

Figure 4-6a shows the Quasi-Steady spray before needle closure. In Figure 4-6 b, at an early stage after the needle valve closure, the emergence of ligaments very close to the nozzle exit is apparent. At this stage, the decelerating jet advances the air entrainment which subsequently widens the early spray angle. Sometimes later, Figure 4-6 c, a thinner liquid jet exiting the nozzle due to further reduction of the fuel mass flow rate, is in qualitative agreement with Swantek *et al* [12] measurements. Further progression of the EOI is shown in Figure 4-6d and e where the dissipation of ligaments corresponds with the appearance of large droplets. The enhancement of air entrainment in the spray chamber leads to much more dispersed region further downstream and more dilute area close to the nozzle exit. Lastly, Figure 4-6 f shows the disappearance of ligaments and various ranges of droplets sizes produced at the final stage of EOI process. The existence of large droplets at EOI is potentially a source of unburnt hydrocarbons and detrimental emissions in a real engine.

Finally, two double frame images, Figure 4-7, are presented to show the type of breakup regime, the fragmentation process of thick low-speed ligaments and the formation of large droplets. Figure 4-7 demonstrates the mechanism by which the large droplets form during the EOI process (sometime between Figure 4-6e and f). The long dominant ligaments in Figure 4-7 demonstrate the coalescence of local liquid swelling along the thread into more distinct beads which eventually disintegrate into large primary and small satellite droplets. Images a and b are captured from a single injection event with 25 μs inter-frame time. The emergence of more ligaments from the nozzle in image b is possibly due to needle bounce, wobble, and vibration after needle valve closure. The entrained background air stretches the filaments followed by the beads-on-a-string structure as a result of equilibrium of inertial, capillary, viscous, and elastic forces [132]. The size of these beads determines final diameters of the droplets [26]. The initial diameter of the string with bead in Figure 4-7a is approximately 30 μm. The approximate diameter of the beads is a key factor in the determination of the final droplets size, which vary from about 20 μm up to 65 μm. This string travels downstream with a velocity of around 5 m/s giving corresponding Reynolds, Weber and Ohnesorge number of 121, 44.3, and 0.055 respectively. In this low-viscosity regime, ligaments fragment via a Rayleigh-Plateau instability on the capillary timescale of $\tau_{PR} = \sqrt[2]{\rho h^3/\sigma}$, where h is the initial diameter of the ligament [26]. For frame a of Figure 4-7, the capillary timescale is about 27 μs corresponding to the duration of the ligament pinch-off process. Figure 4-7b shows the subsequent ligament fragmentation into droplets that occurred in the inter-frame of 25 μs corresponding to the above estimated time scale of 27 μs. The fragmentation process at this regime is triggered by the induction of

perturbations on liquid surface which have been originated from a two-stage instability mechanism: a shear instability of Kelvin-Helmholtz type forming axisymmetric waves; and the gas boundary layer at the interface producing interfacial undulations [26]. The combination of these mechanisms develops the irregularities on the liquid surface proceeding to apparent beads/swelling on the string/ligament.

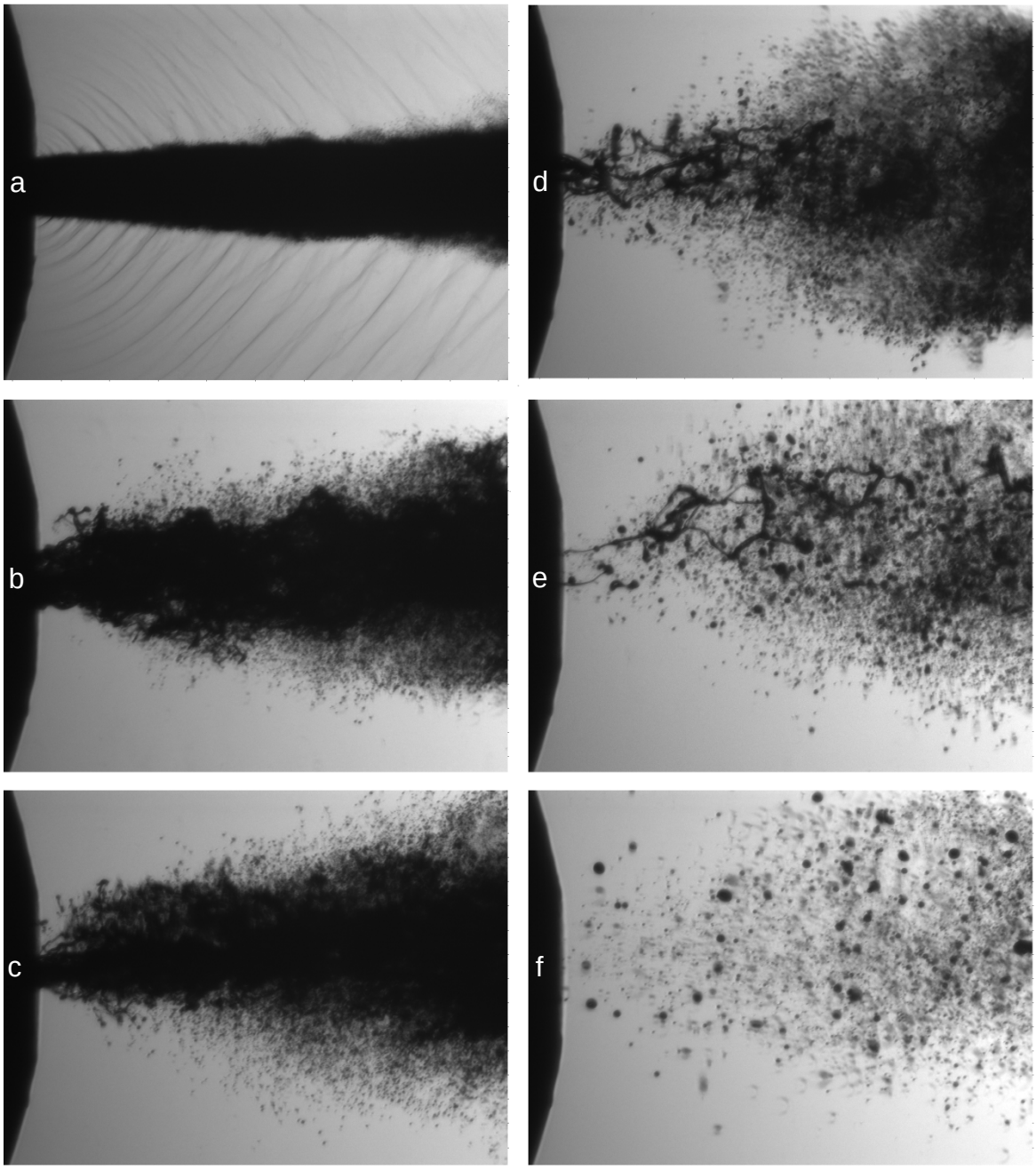

Figure 4-6. Experimental images of EOI process at various times. Frames a, b, c, d, e, and f are taken at progressive times after needle valve closure. The early spray angle undergoes widening associated with the contraction of the emerging jet in the region close to the nozzle exit followed by a reduction in the local spray density, emergence of thick low-speed ligaments and finally formation of large droplets.

A further example of ligament breakup is shown in paired frames c and d with 20 μs inter-frame time. It can be seen that the fragmentation process remains in progress for thicker ligaments compared to the thinner string at the region close to the nozzle exit.

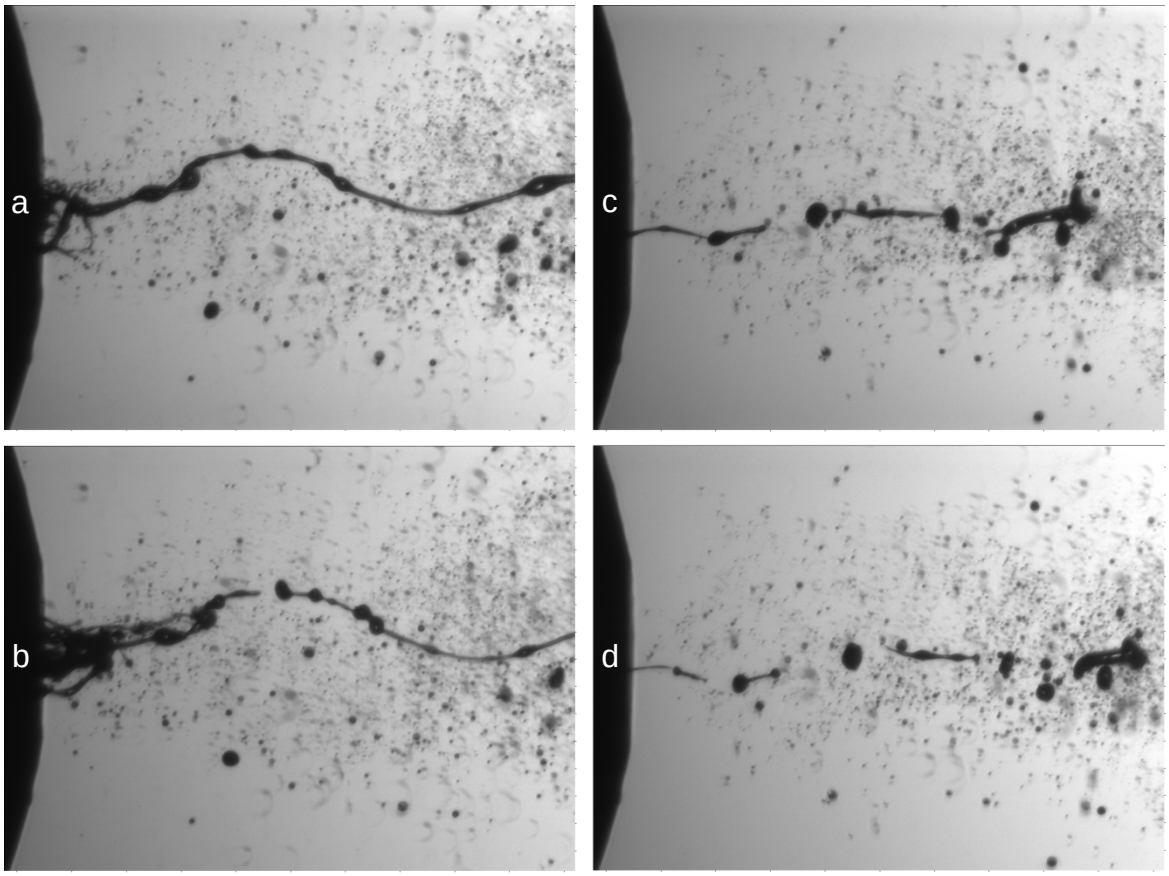

Figure 4-7. Consecutive experimental images of the EOI process at various timings. Images a, and b are paired with an inter-frame time of 25 μs. Successive images c and d are from another injection shot with an inter-frame time of 20 μs. At the EOI, the formation of big droplets from emerging low-speed ligaments is apparent.

Numerically, as described in Ghiji et al [109], the thickness of a ligament is limited to the cell size in that region. Any filament/ligament smaller than the cell size is subject to unphysical pinch-off phenomenon [25, 86, 87] due to the lack of resolution in accurate prediction and tracking of interfacial surfaces. Therefore, capturing low-speed thin ligaments induced at the EOI process requires higher mesh resolutions in the chamber domain which is not feasible with available computation resources.

4.4 Conclusions

The physical processes involved with the EOI of a single-hole sharp edged nozzle are presented. The mechanism of air ingestion into the nozzle hole and sac is demonstrated using non-cavitating incompressible and cavitating compressible models. This mechanism is associated with the development of asymmetry instabilities of a rapidly decelerated jet and simultaneous positive and negative flows (as required for continuity) causing the ambient gas to be ingested into the nozzle. This phenomenon has the potential to explain various phenomena including the presence of air in the spray at the start of injection affecting the morphology of the initial spray breakup that has been observed in our experiments. The compressible approach with a simple cavitation model shows air ingestion into the sac volume as well as the presence of bubbles in the nozzle while the incompressible approach with no cavitation model shows air ingestion into the nozzle only. However, the compressible model requires nine times the computational time of the incompressible model.

Using the non-cavitating incompressible model, for four different chamber pressures of 1, 10, 20, and 30 bar similar air ingestion mechanisms were found. For all operating conditions, the inertia factor dominates the situation leading to air being trapped inside the remaining liquid within the nozzle. The possible impact of the needle valve closure rate was investigated by implementing a ramped inlet pressure profile. No significance changes were observed in the effect of different needle valve closure rates on air ingestion for either the compressible cavitating model or the incompressible non-cavitating model.

The fragmentation process and breakup regime of low-speed ligaments presence at the EOI are discussed. The formation of numerous droplets with various diameter ranges due to ligament breakup after needle closure provides additional evidence on the formation of pollutants at the end of an injection event.

4.5 Acknowledgment

This work was supported by the Australian Maritime College and the Defence Science and Technology Group. The authors would like to acknowledge the use of the high performance computing facilities provided by the Tasmanian Partnership for Advanced Computing (TPAC) funded and hosted by the University of Tasmania.

Chapter 5 :

Summary, Conclusions and Further Work

In this chapter an overall summary of the thesis is provided bringing together the achievements of the individual chapters. Conclusions and implications of the results, limitations, and the recommendations for further research are discussed.

5.1 Summary

The focus of this thesis is investigation of multiphase flow dynamics inside a diesel injector nozzle and in a region close to the nozzle exit (primary atomisation) during the entire injection event which consists of start of injection (SOI), Quasi-Steady, and end of injection (EOI) phases. In this Chapter, an overall evaluation is made of the results and findings, and their contributions to the research field. Limitations of the study are also discussed and used to provide guidance for future research to increase the understanding of the significance of injector design on diesel spray dynamics.

The motivation for this research is to achieve a more accurate predictive tool in seeking to gain knowledge on the phenomena and their interactive mechanisms, associated with the injection of high-pressure diesel fuel. More challenging subjects in this field, such as in-nozzle fluid dynamics and primary atomisation of the jet occurring in the vicinity of the nozzle exit, are analysed.

A literature review is carried out on various numerical approaches to accurately predict the phenomena existing during a high-pressure fuel injection event. Moreover, this survey covers the whole range of an injection where the liquid jet experiences an advancement in the fuel mass flow rate during the SOI, a semi-steadiness in mass flow rate at the Quasi-Steady stage where the main portion of fuel is delivered at favourable injection pressures to the chamber and finally cessation in the fuel mass flow rate during the EOI.

Whilst numerical models have been well established, the application of these methods has always been associated with simplifications that affect the accuracy of the results obtained and consequently their interpretation. The main aim of this study is to promote a high-fidelity time-efficient model which could accurately and consistently capture the physics at the extreme environment which takes place at within and near the nozzle exit of a diesel injector. The precise prediction of in-nozzle flow dynamics and primary atomisation are critical factors in any injection modelling, governing the whole process of the jet breakup, secondary atomisation, and subsequently the air-fuel mixture quality and finally emission production. Thus, it is important to have a good understanding of these phenomena and their interactive effects on other physics in order to design injectors which can meet new strict emission standards.

This thesis focuses only on the flow dynamics inside the nozzle and in a region very close to the injector tip over the duration of an injection event. This has allowed the multiphase flow

characteristics to be the focal point of the study, thus enabling the investigation of the effects of numerical setup and method, to be investigated in parallel with physical modelling.

The present modelling method utilises an incompressible non-cavitating Eulerian/VOF/LES model (Chapter 2) and a compressible cavitating Eulerian/VOF/LES model (Chapter 3) both for the SOI and Quasi-Steady stages of injection. Finally incompressible non-cavitating and compressible cavitating Eulerian/VOF/LES models are applied to the EOI processes (Chapter 4). The experimental work carried out to validate and supplement the CFD results is discussed within the respective chapters.

5.2 Conclusions

List below explains how each corresponded objective has been met.

1. Incompressible (Chapter1) and compressible (Chapter 2) primary atomisation models for the in- and near-nozzle region have been successfully implemented in an Eulerian/VOF/LES framework. The compressible model requires nine times the computational time of the incompressible model.

2. The experimental and validated numerical results provide a clearer comprehension into the effect of phenomena such as cavitation, compressibility, air ingestion on the diesel spray dynamic at the SOI, Quasi-Steady, and EOI stages.

3. The effect of grid size on the associated physics such as the in-nozzle generated turbulence, interfacial surfaces instabilities, the fragmentation of liquid jet and subsequently droplet size distributions has been shown and discussed. A grid independence study shows the convergence of mean jet velocity and total pressure at the nozzle exit. In the spray chamber (atomisation zone), it has been revealed that: an increase in grid resolution leads to enhancement in liquid core length, number of droplets, and fragmentation processes occurring at regions close to nozzle exit; and the scale reduction of captured eddies, droplet sizes, and early spray angle. It is concluded that a better agreement between numerical and experimental results can be achieved by increasing grid density.

4. The analysis of various temporal and spatial numerical discretization schemes showed that the second-order time derivative scheme and NV Gamma convection-specific

interpolation scheme offered more promising results compared with the first-order integration scheme and TVD convection-specific interpolation schemes respectively.

5. The effect of cavitation on in-nozzle flow and spray dynamics at various stages of injection has been discussed. For detailed outcomes of this investigation please refer to section 5.2.2.2.

6. The compressibility of multiphase fluid flow is included in the model leading to the prediction of shock waves which are initiated at the interfacial surfaces with a velocity higher than the speed of sound (here 345 m/s for pressurised air of 30 bar). The effect of compressibility at each temporal stage of injection has been highlighted in section 5.2.2.3.

7. Conducting incompressible non-cavitating and compressible cavitating models provide a clearer insight into the air ingestion mechanism during the EOI process. The inertia of the exiting jet at the EOI has been determined as the driving force which is associated with the detachment of liquid jet core from nozzle walls and subsequently the entrainment of air into the nozzle liquid.

8. The back- and side-lighting imaging techniques have been used to extract the real physics associated with the injection of a high-pressure diesel fuel, aiming to evaluate and validate the accuracy of numerical results.

9. Experimental results have been employed to evaluate the credibility of the predicted numerical results. Good agreements between the experimental and numerical results at the SOI, quasi-steady, and the EOI have been reported.

As a result of the study described in this thesis, the following detailed conclusions can be drawn:

5.2.1 Temporal Analysis of Spray Dynamics

The diesel spray dynamics have been characterised at the needle valve opening transient (SOI), Quasi-Steady stage, and needle valve closing transient (EOI) both experimentally and numerically. The temporal variation of jet penetration velocity, Reynolds number, and mass flow rate show favourable agreement between numerical and experimental results.

5.2.1.1 SOI

At the start of penetration, an umbrella like leading edge is captured in both the numerical and experimental data however only the experimental images demonstrate a semi-transparent cloud of air-fuel mixture at the leading edge. It is postulated that the transparency arises from the presence of air in the nozzle which occurred during the EOI process of the previous injection shot. The appearance of the starting vortex close to the nozzle exit before fuel penetration is taken as evidence of air inclusion in the nozzle from the previous injection shot. The location and velocity of the starting vortex are investigated experimentally and numerically. The vortex propagates downstream at about 40% of the jet penetration velocity. Later on, this vortex is dissipated corresponding with commencement of jet necking just behind the umbrella-shaped leading edge which was captured in both experimental and numerical results. The experimental shadowgraphy images show a rougher surface, greater transparency, more oblique angle and earlier disintegration of the leading edge in comparison with the numerical predictions. In-nozzle air inclusions left from the previous injection event are presumed to be a major factor in the differences between experiment and prediction. Other factors could include limitations in the numerical models and solution schemes.

In the early stages of injection, little difference is found between the predictions of the compressible and incompressible models.

Numerical results are evaluated and validated by conducting qualitative (general morphology, interfacial surface instabilities) and quantitative (penetration velocity of 100 consecutive experimental shots) comparisons with the experimental results.

Experimental images show a cloud of fine droplets surrounding the spray early in the injection. These fine droplets obscure the surface of the spray making it difficult to image the surface morphology.

5.2.1.2 Quasi-Steady Stage

At the Quasi-Steady stage, the predicted early spray angle of the jet shows good agreement with the experimental measured angle while the numerical mass flow rate is around 21% under-predicted compared to the experimental data. This latter deviation is thought to be largely due to the finite radius of the nozzle entrance in the real nozzle compared with the numerical model where a sharp edged entrance is assumed.

The presence of shock waves in the high-pressure diesel spray is found in both the experimental and numerical results. Good agreement is reported between the experimental and numerical interfacial surface velocity, reinforcing the conclusion that the shockwaves are initiated on the spray surface where the interface velocity exceeds the speed of sound in air. The shockwaves are first seen in the region close to the nozzle exit then they also appear at further distances as the jet velocity increases.

5.2.1.3 EOI

Upon closure of the needle valve the flow rapidly decelerates. Numerical results of the incompressible non-cavitating model show a single bubble of chamber gas remains embedded within the liquid in the nozzle after velocities have largely dissipated. The results of the compressible cavitating model demonstrate how chamber gas is entrained into the sac volume through the air passage previously generated by hydraulic flip.

The possible impact of the needle valve closure rate is investigated by implementing a ramped inlet pressure profile. No significance changes due to the ramped profile are observed in the outcome of the air ingestion process for either the compressible cavitating or the incompressible non-cavitating model.

The fragmentation process and breakup regime of low-speed ligaments present at the EOI are discussed. Analysis of the ligament breakup mechanism shows agreement between the measured breakup time and theoretical breakup time based on Rayleigh Plateau instability. The formation of numerous droplets with various diameter ranges due to ligament breakup after needle closure potentially contribute to the formation of pollutants at the end of an injection event due to incomplete combustion of the larger droplets.

5.2.2 Physics of multiphase Flow

In this section the physical processes involved in the spray dynamics are described. Compressibility, temperature and cavitation effects for the liquid phase are included in the compressible numerical model. The effects of cavitation and in-nozzle turbulence on the growth and disintegration of surface structures of the emerging jet are characterised providing insight into the physics of primary atomisation.

5.2.2.1 In-nozzle turbulence

The non-cavitating incompressible model shows that where cavitation is not present, in-nozzle turbulence dominates the disintegration process of the liquid jet. As the jet velocity increases, disintegration commences closer to the nozzle exit.

Initially, toroidal streamwise waves develop on the jet surface, travel downstream towards the leading edge umbrella and grow in magnitude until disintegrating in the wake. Subsequently, the emergence of longitudinal spanwise waves from the nozzle is accompanied by disintegration of the toroidal streamwise waves, production of hairpin vortices and radial expansion of the jet mixing layer. Later still, the cavitation layer reaches the end of the nozzle resulting in hydraulic flip. Despite the potential for reduced production of turbulence in the nozzle due to separation of the liquid from the wall the turbulent intensity on the jet surface near the nozzle exit is seen to be higher than prior to hydraulic flip. This is thought to be due to increasing jet velocity as injection pressure increases.

5.2.2.2 Cavitation

Cavitation is initiated in the low pressure region downstream of the sharp edged nozzle entrance. The cavitation layer grows and finally reaches the end of the nozzle leading to the penetration of high pressure chamber air into the low pressure cavities, further narrowing the jet. At this stage (hydraulic flip) the mass flow rate decreases momentarily but then continues to increase due to increasing injection pressure. This mass flow rate trend shows good agreement with published data in predicting the different stages of cavitation.

At the EOI, the presence of cavitation alters the mechanism of air ingestion compared with the non-cavitating model. The cavity allows access of high pressure chamber air into the nozzle which would moderate the pressure drop caused by the jet inertia when the needle valve closes. The inclusion of compressibility in the cavitating model also limits the pressure drop by allowing the liquid to extend under the tensile forces arising from the jet inertia. These two factors together would suppress the production of cavitation bubbles within the nozzle fluid during the EOI.

5.2.2.3 Compressibility

The morphology of the penetrating jet prior to hydraulic flip is not significantly influenced by the compressibility of the fluids.

During the Quasi-Steady stage, the compressible model predicts shockwaves as evidenced by sharp density gradients in the gas phase. The onset and development of shock waves is also shown experimentally and the jet interface velocity is inferred from the shock wave angle, on the assumption that shockwaves are generated at the boundary between the jet and the surrounding air where the liquid velocity at the interface exceeds the local sonic velocity of the air. The interface velocity derived directly from the numerical predictions shows favourable agreement with the experimentally derived values, supporting the conclusion that shock waves occur where the jet velocity at the interface with the surrounding air exceeds the local speed of sound.

As mentioned in section 5.2.3.2, during the EOI, compressibility allows liquid extension and leads to finite rates of propagation of disturbances, moderating the pressure drop in the nozzle liquid caused by liquid inertia, compared with the incompressible model

5.2.2.4 Air ingestion

The mechanism of air ingestion is associated with the development of asymmetric instability of the rapidly decelerated jet and simultaneous positive and negative flows (as required for continuity) causing the ambient gas to be ingested into the nozzle. The compressible approach with a simple cavitation model shows air ingestion into the sac volume as well as the presence of bubbles in the nozzle while the incompressible approach with no cavitation model shows air ingestion into the nozzle only. The presence of the cavity over the whole length of the nozzle walls and connected to the chamber prior to the EOI, as predicted by the compressible cavitating model, facilitates the movement of air from the chamber into the sac. This air ingestion has the potential to explain various phenomena including the presence of air in the spray at the start of the next injection affecting the morphology of the initial spray breakup that has been observed in experiments.

Using the non-cavitating incompressible model, for four different chamber pressures, similar air ingestion mechanisms are found. For all chamber pressures, the inertia factor dominates the situation leading to air being trapped inside the liquid remaining within the nozzle.

5.3 Further Work

Future work could involve:

1. Development of a more complex cavitation model which allows for multiple phases, nucleation and condensation.

2. Numerical investigation of the effect of air inclusion on the morphology and behaviour of the penetrating jet.

3. Experimental investigation of the effect of nozzle geometry on cavitation and primary atomisation.

4. Modelling of the dynamics of needle valve motion and the flow of fuel past the needle seat. This could potentially include analysis of fluid-structure interaction between the fuel and the needle.

5. Development of optical techniques which allow clear imaging and analysis of the surface structure of the jet, beneath the cloud of fine droplets generated early in the injection.

6. Inclusion of the in-nozzle surface roughness in the numerical models.

7. Extension of the numerical and experimental domains.

[Page intentionally left blank]

Appendix I:

Nozzle Geometry Design

I.1 Manufacturer's drawing of injector

Figure I-1 reveals the geometry of AMC's injector provided by a Japanese manufacturer. The extraction of exact design of sac and orifice of the injector is impossible due to their small size relative to the other parts of the injector.

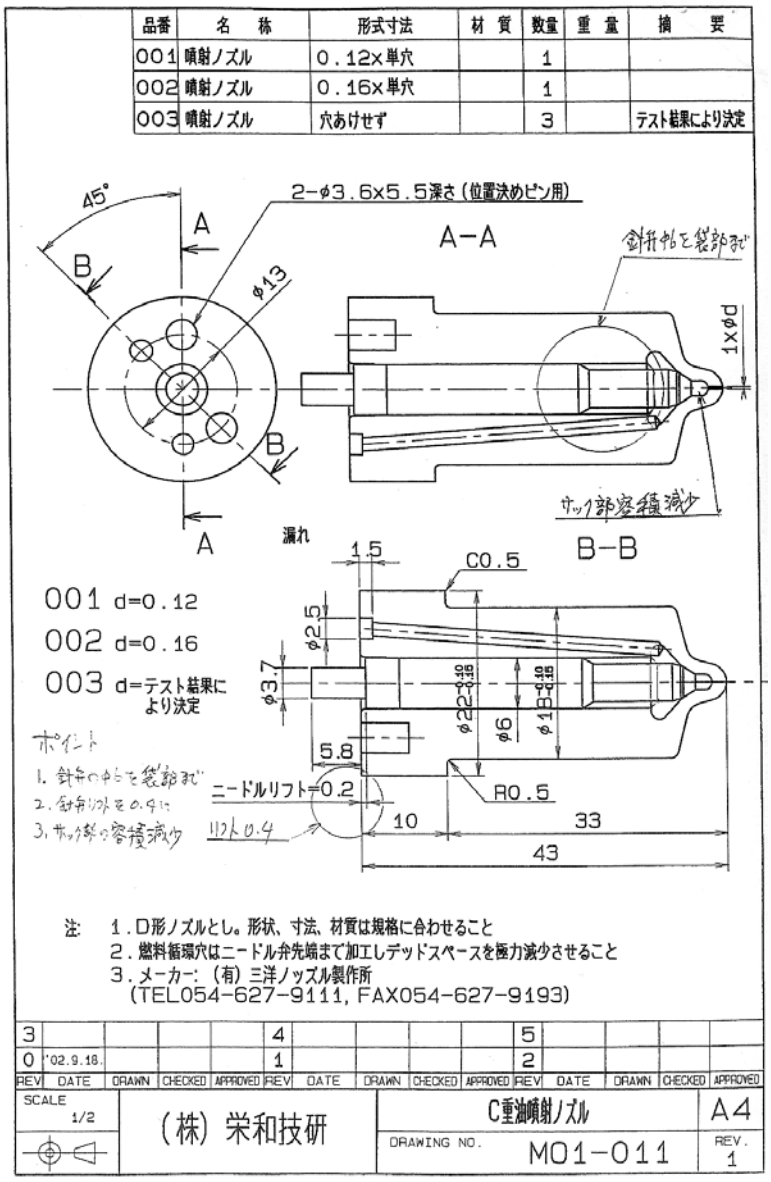

Figure I-1. Manufacturer's drawing of the injector design

I.2 X-ray micro computed Tomography of injector nozzle tip

In a typical tomography experiment, a sample is placed in the X-ray beam and rotated through an angular range between -90° and +90°. The experimental setup is shown in Figure 1-3. The Centre for Materials and Surface Science and the Centre of Excellence for Coherent X-ray Science at La Trobe University employ an *Xradia MicroXCT* instrument with experimental conditions described in Table I-1.

Table I-1. Operating condition of X-ray Tomography measurements

X-ray energy	150 kV,10 W
Exposure time for each projection	60 sec
Total number of projections	721
Objective magnification	10x
Source to sample distance	100 mm
Detector to sample distance	15 mm
Pixel numbers	1016 x 1024 x 1024
Effective voxel size	2.318μm

A set of absorption images is taken sampling this range of rotation angles. Using reconstruction algorithms, a 3D view of the sample can be computed, allowing the interior and exterior of the material to be investigated non-destructively as can be seen in Figure I-2.

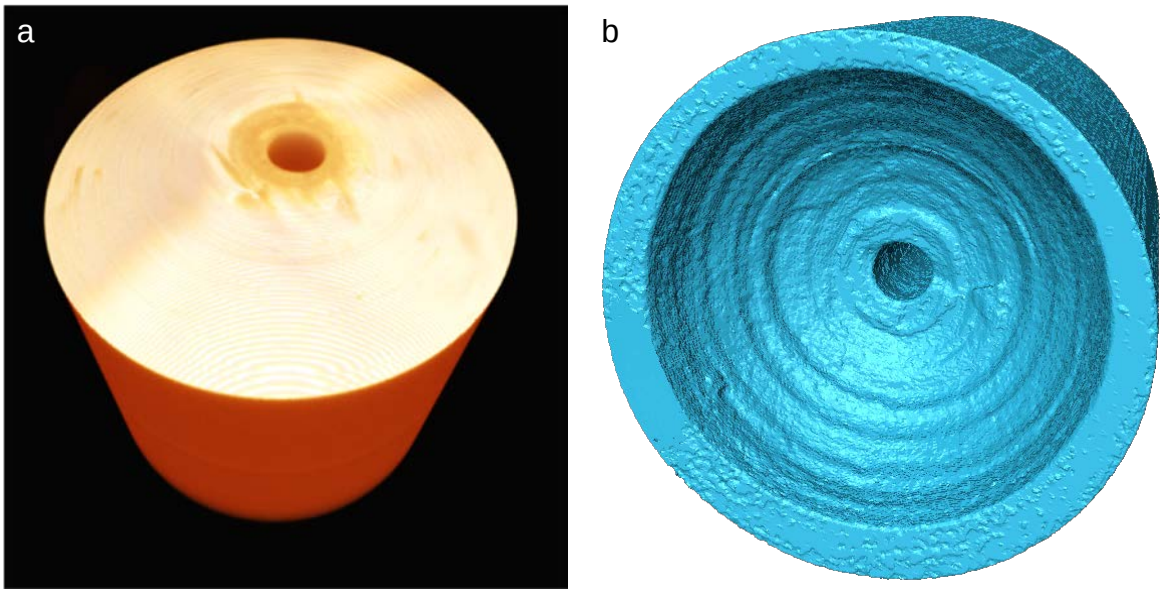

Figure I-2. 3D reconstructed views of the injector demonstrate the external (a) and internal (b) design. The 3D images reveal the rough surface of the sac and a worn at the tip of the nozzle hole.

Various cross-sectional views of the injector achieved by the X-Ray Tomography measurement manifest the geometry and dimensions of sac and nozzle hole, are shown in Figure I-3, I-4, and I-5.

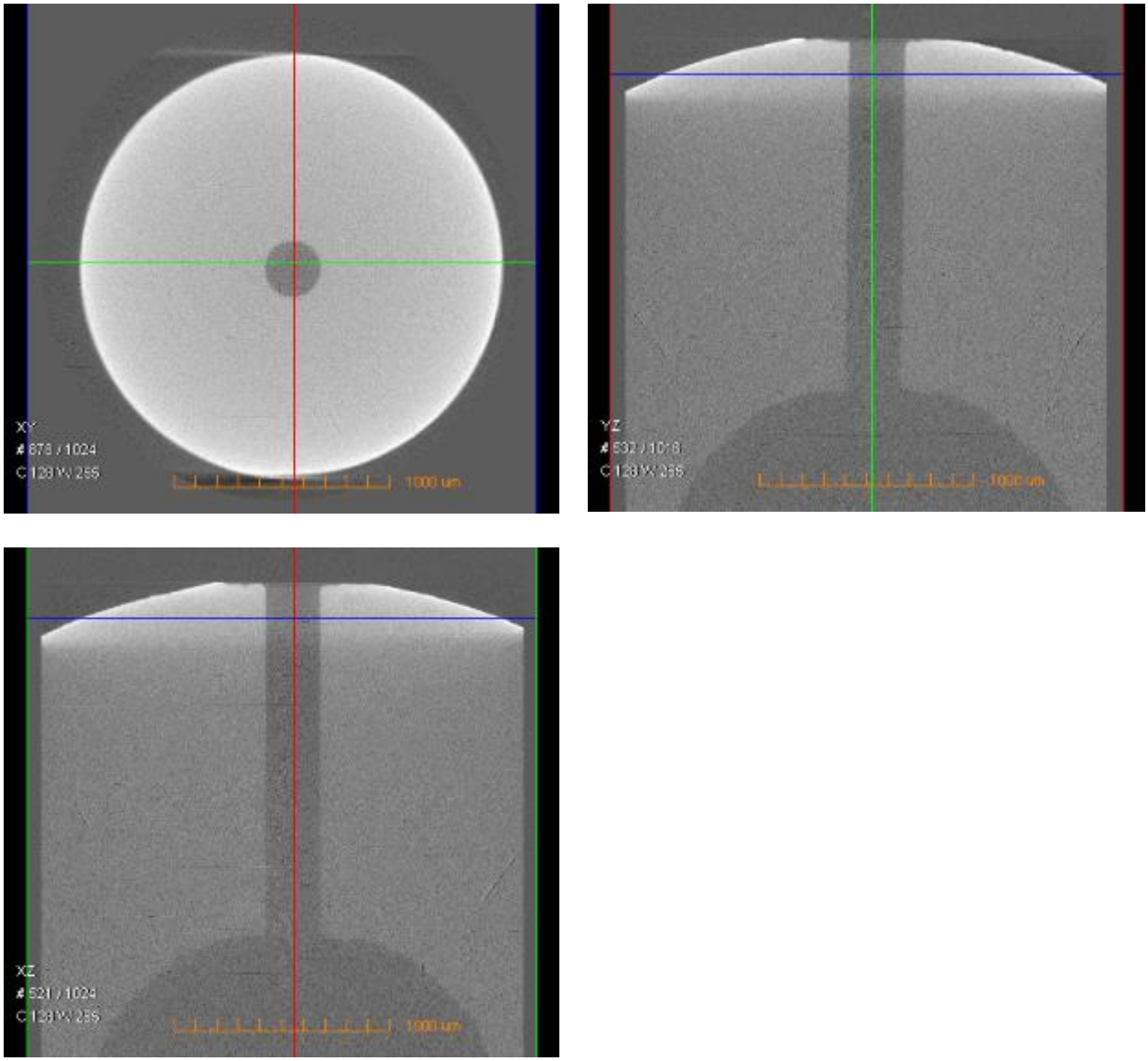

Figure I-3. X-Ray Tomography measurement of sac and nozzle geometry from different cross-sectional views. The images illustrate a hemispherical and a cylindrical sac and nozzle hole respectively.

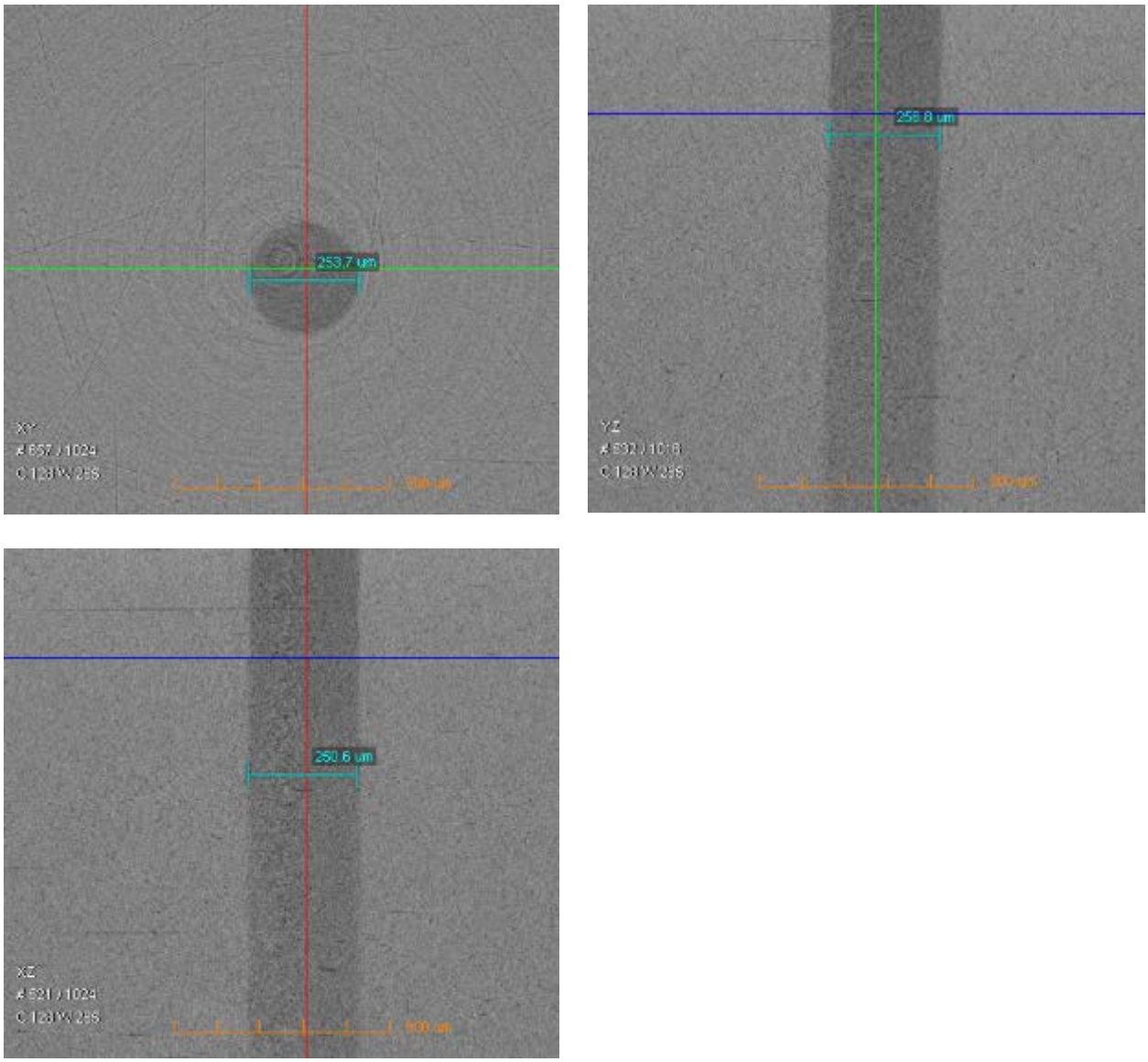

Figure I-4. X-ray tomography test shows the diameter of the nozzle hole which is about 250 μm.

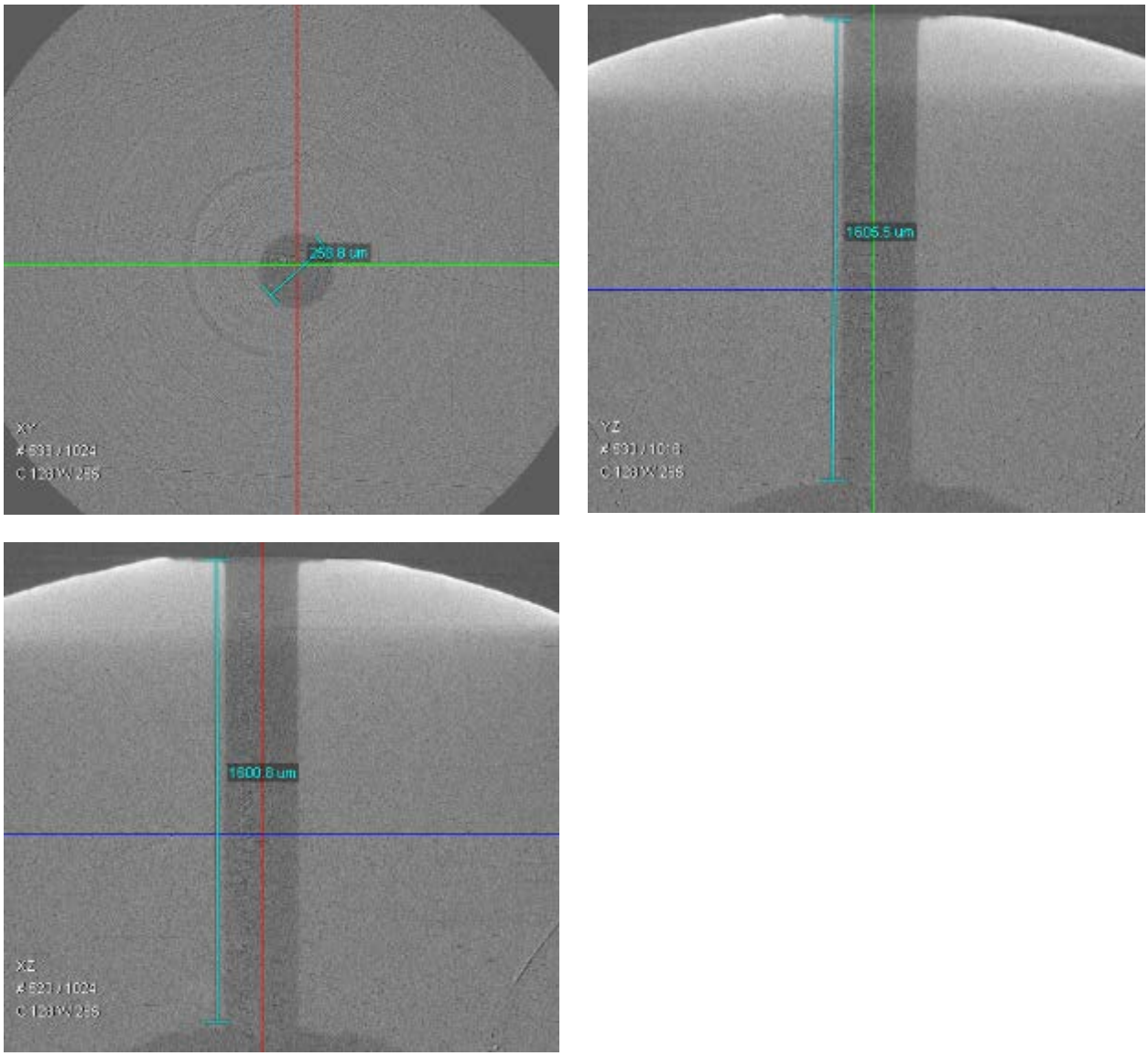

Figure I-5. X-ray tomography test shows the length of the nozzle hole which is about 1600 µm.

[Page intentionally left blank]

Appendix II:
CFD Modelling of Primary Atomisation of Diesel Spray

This appendix has been published in the Proceedings of the 19th Australasian Fluid Mechanics Conference. The citation for the research article is:

Ghiji, M., Goldsworthy, L., Garaniya, V., Brandner, P. A., & Hield, P.,'CFD Modelling of Primary Atomisation of Diesel Spray', *Proceedings of the 19th Australasian Fluid Mechanics Conference*, 8-11 December 2014, Melbourne, Australia, pp. 1-4.

For the avoidance of repetition, the original proceeding has been modified for this thesis.

Abstract

Primary atomisation in a high-pressure diesel jet is modelled using Large Eddy Simulation. The Volume Of Fluid phase-fraction based interface capturing technique was applied in the Eulerian framework using the open source CFD code OpenFOAM. Conditions modelled replicate those of a parallel experimental program including nozzle inlet pressure change, spray chamber pressure (ambient zone) and temperature and viscosity of both phases. The nozzle geometry was obtained using X-ray Computed Aided Tomography. Diesel fuel pressure at sac inlet was defined based on injection pressure profile (ranging from 30 to 1200 bar) captured during experimental tests. The effect of different grid sizes with mesh resolutions of 2.5, 8, and 18 million cells on primary breakup was investigated. The results assist with understanding the flow behaviour during primary breakup, including commencement of fragmentation and the early spray cone angle. The results also showed that the jet break-up increased in meshes with higher resolutions. Furthermore, investigation of in-nozzle flow indicated a non-axisymmetric behaviour. The early spray angle of the numerical results was less than the experimental data, probably due to cavitation and compressibility not being modelled. These effects will be studied in forthcoming works.

II.1 Introduction

In diesel engines, combustion chambers are fed by high-pressure fuel injected as a cone spray. This spray undergoes a series of instabilities (longitudinal and transverse) which lead to the fragmentation of the liquid bulk into liquid structures that further disintegrate into droplets. This initial process of atomisation is called the primary breakup and occurs in the vicinity of the injection point. The mechanisms of the primary breakup which initiate the atomisation process control the extent of the liquid core and provide initial conditions for secondary breakup in the dispersed flow region [2, 25, 84]. So far, many theories are proposed to describe the primary atomisation mechanisms, including:

- Aerodynamic shear forces which act through striping and Kelvin-Helmholtz instabilities [8, 25]
- Turbulence-induced disintegration which has significant effect in lower velocity jet breakup [72]

- Relaxation of the velocity profile, creating a "bursting" effect specially in non-cavitating jet and large velocity differentials [8]

- Cavitation-induced disintegration of the jet due to the reduction of cross-section area and collapse of cavitation bubbles at the nozzle inlet [8, 38]

- Liquid bulk oscillation provoking the toroidal surface perturbation [72].

It is difficult to separate and investigate these different effects experimentally [2, 8, 72]. To develop diesel engines with both optimal fuel economy and reduced pollutant emissions, it is necessary to thoroughly understand the spray processes and then characterise the effects of different parameters and engine operating conditions on fuel flow structures. This is a challenging subject to study both experimentally and numerically.

There are two main physical phenomena involved inside the nozzle, cavitation, and in-nozzle turbulence. This paper concentrates on the effect of in-nozzle turbulence. The effects of cavitation will be studied in future work. Turbulent flows are represented by eddies with ranges of length and time scales. LES directly resolves large scales and models small scales. Modelling only small scales and solving the large scales, allows the use of a much coarser mesh and larger time steps in LES compared with DNS. Despite this, LES still needs a finer mesh compared with the ones used for RANS computations. Since RANS models cannot capture the transient spray structure [2, 25], including droplet clustering and shot to shot variability, LES is applied to overcome these limitations.

Reviews of the existing atomisation models demonstrated that all these models (blob, Huh/Gosman, MPI, Arcoumanis, Nishimura, V.Berg, Baumgarten, ReitzWave model, Taylor Analogy Breakup model) simplify the droplet generation in the dense region (primary atomisation) resulting in inaccurate and unrealistic simulations [2, 33]. For example, the blob atomisation model which is the most employed model not only simply generates parcels with the size of the nozzle diameter but also does not take into account the physics of in-nozzle turbulence and in-nozzle cavitation. In addition, these conventional atomisation models with LPT limit the grid fineness near the nozzle and do not allow LES to capture the features of the spray and background fluid flow near the nozzle. Refining the grid creates problems in the LPT approach due to the high liquid fraction in each cell [33]. These limitations motivate the development of a new method to model the primary atomisation using the Eulerian/VOF/LES approach, instead of using the conventional atomisation model. In this study, the flow inside the

nozzle and the liquid bulk near the nozzle exit and its fragmentation (primary atomisation) in a non-evaporating spray in a chamber are analysed.

II.2 Methodology

II.2.1 Mathematical Method

In this study, the VOF phase-fraction based interface capturing technique is used in an open source CFD code OpenFOAM v2.1. The full details of the mathematical model are described in section 2.2.2.1.

II.2.2 Numerical Solution Method

The mathematical model for the atomisation simulation is solved using an implicit finite-volume method and employs second-order spatial and temporal discretisation schemes. The solution procedure employed uses the Pressure Implicit with Split Operator (PISO) algorithm, in conjunction with conjugate gradient methods.

II.2.3 Boundary Conditions and Initial Setup

Atomisation is affected by the shape of the sac and the design of inlet nozzle hole [25]. The computational domain has therefore been modelled using the geometry of the experimental nozzle determined using X-ray Computed Aided Tomography (CAT) analysis as shown in Figure 2-2.

All experimental conditions replicated in numerical models were based on the previous study by Bong et al. [2] including diesel fuel pressure at the sac volume inlet, spray chamber pressure and air and diesel fuel temperature and viscosity . This study was performed using a single solid cone diesel injector in the constant volume High-Pressure Spray Chamber (HPSC), at Australian Maritime College (AMC). Micro spray structure and physics of the spray were studied by shadowgraphy employing a long range microscope along the atomisation zone. Fuel properties and setup conditions used in the simulations are described in Table 2-1.

To initialise the simulation, the sac volume and three-quarters of the orifice were filled with diesel fuel with a pressure of 30 bar, matching the experimentally measured injector pressure profile. A hexahedral structured mesh was generated as shown in Figure II-1, with mesh refinement in the boundary layers (sac and orifice walls) and the atomisation zone. It has been

shown that the spray structure is not axisymmetric [2, 84], so the full 360° of the atomisation zone has meshed. In order to perform a mesh dependency study, different mesh resolutions were produced with coarse (2.5×10^6 cells), medium (8×10^6 cells) and fine (18×10^6 cells) resolutions. The cell size was refined to 1 μm in the primary atomisation zone and near nozzle wall in the finest resolution case (18×10^6 cells) as shown in Figure II-1.

This cell size can capture droplets down to 2 μm range based on the optimistic premise that 2-3 cells can give a reasonable representation of a single droplet. The resolutions of these three cases are summarised in Table II-1.

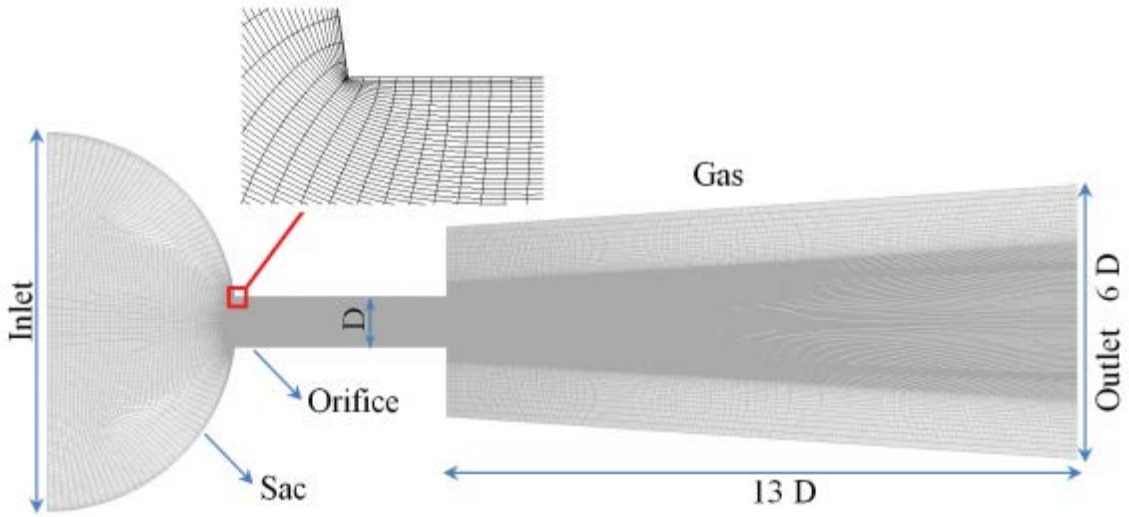

Figure II-1. Calculation domain and boundary conditions (refined mesh in atomisation region and nozzle hole).

Table II-1. Resolution and cell count of three cases for mesh study.

Case	Resolution	Cell count
Coarse	5 μm	2.5×10^6
Medium	3 μm	8×10^6
Fine	1 μm	18×10^6

II-3 Results

The turbulent eddies produced within boundary layers inside the orifice lead to small/large-scale irregularities, which are considered to be the origin of initial jet surface instabilities. Figure II-2 illustrates the enlarged view of velocity profile inside the nozzle hole for three cases which depict smaller-scale irregularities in cases with higher mesh resolution.

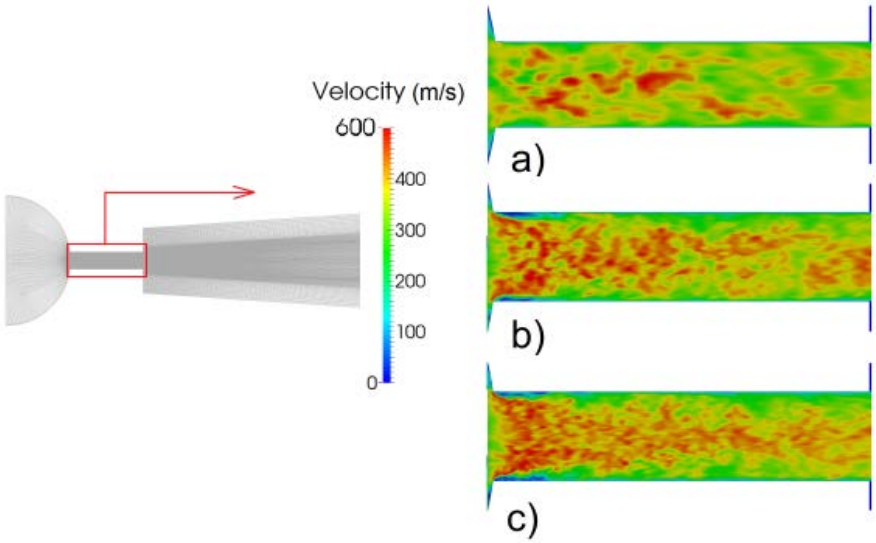

Figure II-2. The velocity magnitude of jet inside the nozzle hole at t = 1 ms and P = 1200 bar for (a) Coarse, (b) Medium and (c) Fine mesh

The general spray structure is illustrated in Figure II-3 by γ=0.1 isosurface, showing the velocity magnitude plotted in the axial plane at 1 ms after the Start Of Injection (SOI) where the diesel fuel pressure at the sac inlet is 1200 bar for the three different cases. The onset of primary atomisation can be seen to occur close to the nozzle exit for the three different mesh resolutions. Progressively finer droplets are captured near the nozzle exit with increasing mesh density most noticeably for the finest case (18 M cell). In-nozzle-generated turbulence in combination with the relaxation of the velocity profile at nozzle exit initiates the perturbations leading to amplification of surface waves. The number of droplets considerably increases while the droplet diameter decreases with increasing mesh resolution. This is due to the better prediction of the small-scale turbulent structures within the nozzle hole as presented in Figure II-3, resulting in smaller-scale structures on the jet surface. These instabilities develop into finer clusters and intensify the breakup process. Consequently, the rate of breakup increases in cases with higher mesh resolution.

The growth of non-axisymmetric disintegration at different cross-sections from the nozzle orifice exit is presented in Figure II-4. As seen, the formation of small waves is obvious even 1 nozzle diameter downstream of the nozzle exit. Primary break up triggers and intensifies after x/d =1. This can question the ability of any conventional atomisation models [33] which don't predict small droplet generation close to the nozzle exit. Up to 5 diameters (x/d =5) downstream of the nozzle exit the breakup process is fully developed since the liquid core is narrowing to tapered ligaments. This liquid core is totally disintegrated at 8 diameters (x/d=8) downstream, resulting in a high number of droplets.

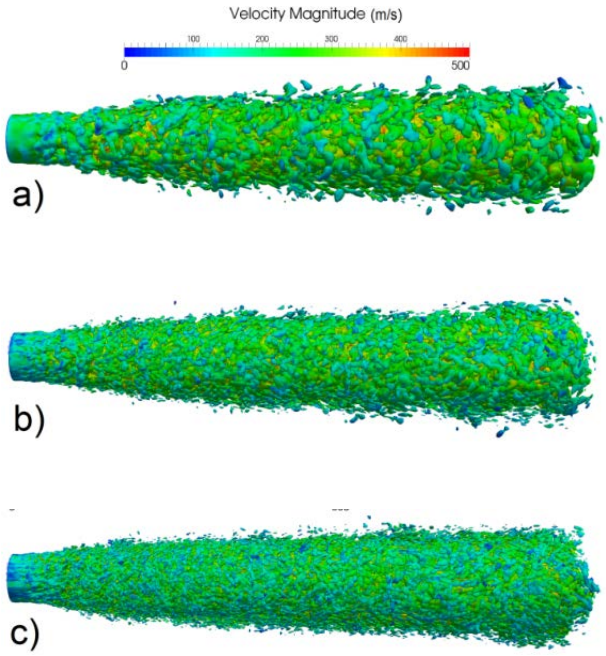

Figure II-3. Morphology of the spray coloured by velocity magnitude at t = 1 ms and P = 1200 bar in sac volume inlet, indicated by isosurface of volume fraction γ = 0.1, (a) Coarse, (b) Medium and (c) Fine cases.

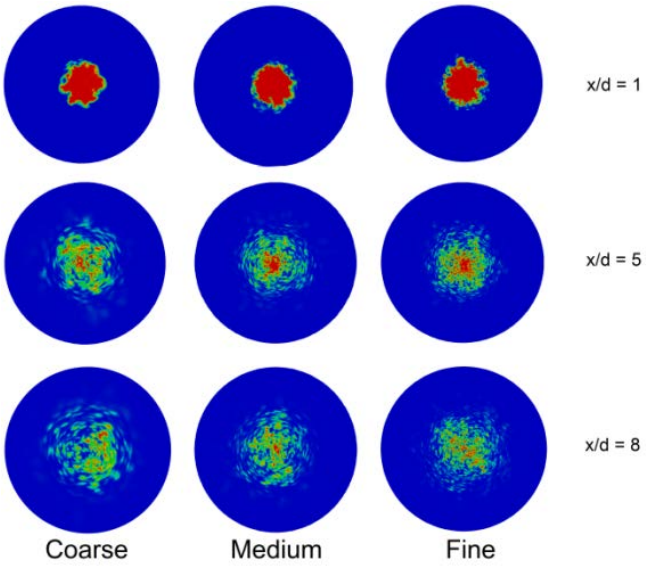

Figure II-4. In-nozzle liquid distribution in cross-sectional planes at different axial positions for Coarse (Right column), Medium (Middle column) and Fine (Left column) cases at t = 1 ms and P = 1200 bar in sac inlet

Figure 2-17 shows the measured early spray angle at t=1 ms after the SOI where the formation and development of shear layer instabilities can be clearly seen. The end of the nozzle is apparent in the left side of the picture.

To compare the early spray angle of the numerical simulation with the experimental results, Leboissetier and Zaleski [133] core analysis was conducted. Based on this method, three different zones were distinguished at every time step during the fully developed state. The result of this analysis for three different cases is depicted in Figure II-5, showing the time-averaged structure of the atomisation region. The red zone contains only liquid (never contains gas), so that represents the liquid core; blue region experiences just gas while the green region contains sporadically liquid or gas and therefore depicts the atomisation zone. The early spray angle was extracted using an outer boundary of the two-phase mixture (green) zone.

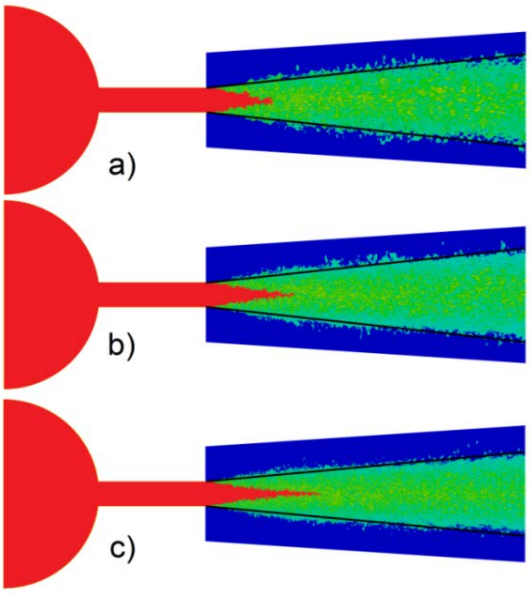

Figure II-5. Spray angle and core analysis, (a) Coarse (b) Medium (c) Fine. The red zone represents the liquid core; blue region experienced just gas and green region depicts the atomisation zone.

The summary of this work is listed in Table II-2, which shows a reduction in spray angle and an increase in liquid core length for the higher resolution cases. The spray angle is over predicted in comparison with experimental data. These variations could be due to cavitation and compressibility effects which were not included in this study. KS Im et al. [131] demonstrated that cavitation plays a significant role in determining the spray angle by reducing the jet diameter.

Preliminary results of diesel spray simulations including the effects of compressibility show an influence on the spray angle. It has also been shown that cavitation occurs along the entire nozzle length which will have a significant impact on the spray. Simulations including both compressibility and cavitation will be published in forthcoming journal papers.

Table II-2. Comparison of spray angle and liquid core length

Case	Early Spray Angle (ϕ)	Core Length (mm)
Experiment [84]	8.7 ± 0.4°	-
Coarse	12.21 ± 1°	0.73
Medium	11.58 ± 0.8°	0.93
Fine	10.16 ± 0.5°	1.18
Arai [134]	-	1.21

II.4 Conclusions

The general structure of primary atomisation of diesel sprays was successfully characterised using CFD methodology which employed the Eulerian/LES/VOF approach to capture the free surface. A mesh resolution study revealed that:

- Mesh independence has not been demonstrated
- Fragmentation of the jet commenced close to the nozzle exit (about 1 diameter from exit)
- The primary breakup process enhances for cases with higher resolution
- The size of droplets decreases for the higher cell resolution.
- Smaller eddies were captured by decreasing size of cells inside the nozzle
- Increasing mesh resolution leads to decrease in the early spray angle and increase in the liquid core length

The over-prediction of early spray angle and under-prediction of liquid core length might be due to not including cavitation and compressibility which will be examined in future studies.

II.5 Acknowledgments

The authors wish to acknowledge the support of the Australian Maritime College and the Defence Science and Technology Organisation (DSTO). The authors express their gratitude to other partners in the project for their support and suggestions.

[Page intentionally left blank]

Appendix III:
Effect of Air Ingestion at the Start of Injection Process in a Diesel Injector

This appendix has been accepted to be published in the Proceedings of the 20th Australasian Fluid Mechanics Conference. The citation for the research article is:

Ghiji, M., Goldsworthy, L., Garaniya, V., Brandner, P. A., & Hield, P.,' Effect of Air Ingestion at the Start of Injection Process in a Diesel Injector', *Proceedings of the 20th Australasian Fluid Mechanics Conference*, 4-8 December 2016, Perth, Australia.

For the avoidance of repetition, the original proceeding has been modified for this thesis.

Abstract

The effect of the presence of air in the injector nozzle at the Start of Injection (SOI) in a single-hole high-pressure diesel injector is investigated experimentally and numerically. Experimental measurements are performed using a laser-based backlit imaging technique through a long distance microscope. Numerical investigation of, in- and, near-nozzle fluid dynamics is conducted in an Eulerian framework using a Volume of Fluid interface capturing technique integrated with Large Eddy Simulation (LES) turbulence modelling. Experimental images show transparency in the emerging jet suggesting the presence of air trapped inside the nozzle liquid from the previous injection event. The numerical model provided a clearer insight into the influence of air on the structure and dynamics of an emerging jet at the SOI. A mathematical code is developed to replicate the backlit imaging approach with the numerical results. The virtual images demonstrate a transparent liquid jet emerging into the pressurised spray chamber gas, in improved agreement with the experimental images. The inclusion of air in the nozzle prior to injection in the numerical model also yields improved agreement in the penetration velocity profile of the jet. These results explain how air inclusion inside the nozzle liquid affects the physics of the penetrating jet at the SOI. The air inclusion also provides an explanation for not only the transparency of the emerging jet but also rough interfacial surfaces captured at the very early stages of injection.

III.1 Introduction

Diesel engines are fed by injectors which supply fuel to chambers where its internal energy is converted to heat through a combustion process driving the pistons and finally delivering the torque to the propulsion system. The quality of air-fuel mixture is mainly controlled by the injector performance, governing the combustion process, engine power and ultimately emissions formation [36]. The atomisation of liquid jet can be improved by increasing the injection pressure, currently up to 3000 bar in compression ignition (diesel) engines. At such a high injection pressures fuels experience temporal, spatial, and physical transient behaviours such as cavitation; evaporation, turbulence, and surface energy effects due to intricate physics involved in and outside of the injector [36]. Based on the Reynolds and Weber/Ohnesorge numbers of the injected fuel in diesel engines the breakup of liquid jets falls well within the atomisation regime. In such a regime, average droplet diameters and scale of flow instabilities are much smaller than the jet diameter. With the aid of recent developments in experimental measurements such as X-ray technologies and high-speed cameras, researchers can conduct detailed analyses to gain clearer insights into the simultaneous and interactive complex physics associated with liquid fuel atomisation.

Application of the Large Eddy Simulation (LES) allows large-scale eddies which contain a more universal energy, to be resolved while small scale eddies are filtered and then modelled by a turbulence model. For Reynolds Averaged Navier-Stokes (RANS) models, less computation time is required because of their averaging approach, diminishing some features of the transient spray structure and the sharp interfaces [2, 36]. Moreover, it is vital to accurately capture the transient behaviour of interfaces as it plays a determining role in the separation and breakup process of a liquid jet. Some numerical techniques reconstruct the liquid-gas interfaces by tracking them explicitly such as the Volume of Fluid (VOF) or Level-Set approach while other techniques utilize a diffuse-interface modelling approach where the interfaces are not explicitly trackable and only partially resolved by a high-resolution grid [36]. Conventional atomisation models predict the breakup process through a Lagrangian framework neglecting background fluid flow effects on droplets and the limitation of grid refinement [2]. An overview of numerical methods suggests the use of the Eulerian/LES/VOF approach in the characterization of, in- and, near-nozzle flow structures.

X-ray imaging of the closing transient in a diesel injector by Swantek *et al.* [12] depicts some gas bubbles ingested in the nozzle and sac. They proposed that the bubbles are due to air

ingestion rather than cavitation in the bulk fluid. Further studies [12, 27, 28] provide a better understanding of the influence of factors such as nozzle hole size, rail injection and spray chamber pressure on the air ingestion mechanism during the End of Injection (EOI) process. They found that the air trapped inside the nozzle is due to the high inertia of the internal flow exiting the nozzle at EOI. Moreover, recent measurements of the early stages of injection in a high-pressure spray chamber by the authors [109, 122] suggest that the transparency of the emerging jet at the SOI is due the presence of air in the first injected fuel, which is likely to be due to air ingestion at the EOI of the previous shot. The ingested air at the EOI affects the fuel penetration and evaporation rate of the next injection event specifically during the first 100 μs after the SOI which subsequently leads to partial combustion and ultimately increase in the production of pollutants [12, 31]. These drawbacks have motivated many researchers to investigate, comprehend and finally optimize the parameters and physics associated with EOI process. Details of these extremely transient phenomena and their corresponding effects are a challenging subject and yet to be fully understood.

The present study focuses on experimental and numerical investigations of the effect of air ingestion processes occurring at the EOI on the general structure of an emerging jet in a single-hole sharp edged nozzle at the SOI. A key aim of the present work is to investigate the source of qualitative deviation between previous experimental and numerical images by including more realistic initial conditions in numerical models. A further aim is to enhance understanding of, in- and, near-nozzle processes.

III.2 Methodology

III.2.1 Experimental apparatus

Experimental tests are conducted by spraying a high-pressure diesel fuel axially through a single solid cone injector from the top of a constant volume High-Pressure Spray Chamber (HPSC). The structure of emerging jet at the early stage of injection has been capturing using a microscopic laser-based backlight imaging (shadowgraphy) technique. The injection pressure profile is highly repeatable from shot to shot, and is increased to 1200 bar at the quasi-steady stage of injection. Detailed specifications and settings of utilized instruments are provided in Ghiji *et al.* [109, 122]. Captured experimental images are used to evaluate and then validate the numerical results.

III.2.1 Mathematical Method

In this study, the VOF phase-fraction based interface capturing technique is employed in the open source numerical code OpenFOAM v2.3. The full details of the mathematical model are described in section 3.3.2.2.

III.2.3 Boundary Conditions and Initial Setup

The 3D computational domain has been generated based on the geometry of the experimental nozzle, as shown in Figure 3-1, revealed by X-ray Computer-Aided Tomography analysis by the Centre for Materials and Surface Science and the Centre of Excellence for Coherent X-ray Science at La Trobe University. Special considerations take into account in the generation of structured hexahedral mesh at atomisation region and no-slip walls. With the aim of previous mesh sensitivity studies [109, 122, 125], results of only a fine mesh with 20 million cells are presented. The cell size is down to 0.1 μm in the nozzle (in the order of the Kolmogorov length scale for the liquid phase) and 1.7 μm in the primary atomisation zone, enables capturing droplets as small as 3 μm diameter.

Fuel properties and test setup conditions are listed in Table 3-1. All experimental and numerical settings, operating and boundary conditions, and injection pressure profiles are replicated based on M.Ghiji *et al.* [109]. The position of the liquid-gas interface and ingested air trapped inside the nozzle liquid from previous injection events determined by the EOI simulation. Final results of the EOI model are used to initialize the present simulation in order to provide clearer insights into the influence of air ingestion mechanisms on the spray structure at the early stage of injection.

III-3 Results and Discussions

The experimental images, Figure III-1a and b, illustrate a starting vortex in the chamber near the nozzle exit before the emergence of the fuel [122], suggesting a partially filled nozzle. Moreover, transparency in the emerging jet can be seen in Figure III-1c and d due to the emergence of trapped air inside the nozzle liquid from the previous injection event [109]. Numerical results without the air inclusion, Figure III-1e and f, show no sign of the transparency while Figure III-1g and h show the transparency inside the emerging jet where trapped air is pushing away and expanding the leading edge of the jet. Numerical images with the air inclusion are montaged based on a developed mathematical code which replicates the shadowgraphy

approach. This code first evaluates the value of each pixel of a virtual backlit greyscale image over 20 stream-wise cut-planes of the jet and then averages these pixel intensities in a single image.

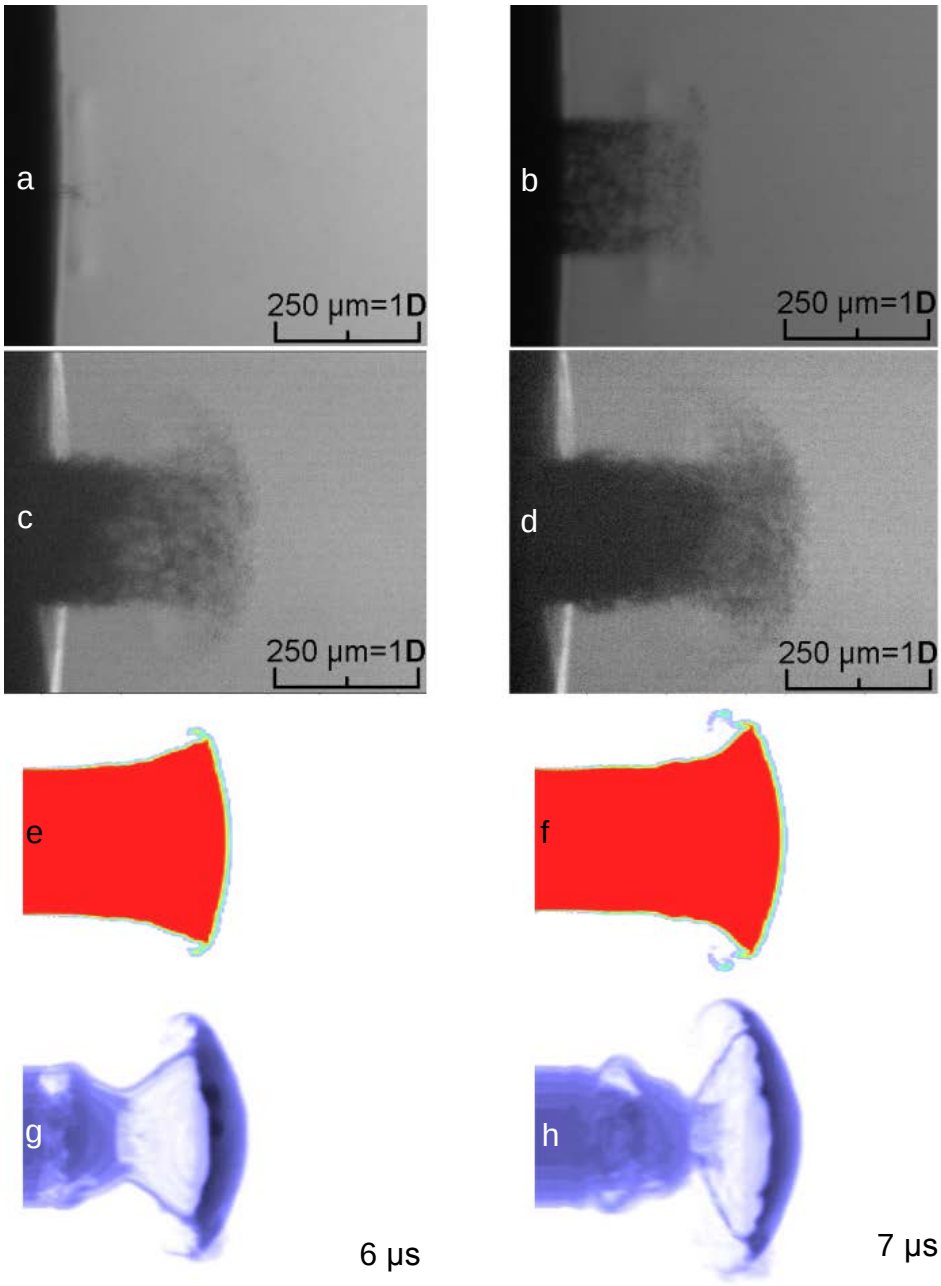

Figure III-1. Experimental results of the starting vortex just before (image a) and just After the Start of Penetration (image b); image c and d are from a single shot with 1 µs inter-frame time show some transparency at the leading edge; image e, f and g, h depict the CFD results without and with air inclusion respectively at 6 and 7 µs ASOP. CFD results in image g and h are averaged over 20 centred cross-sectional planes.

The numerical and experimental results show the early development of the umbrella-shaped leading edge structure and the early stages of shedding of droplets from the rim of the leading edge. Shadowgraphy images are compared with numerical results in Figure III-2, presenting the general structure of the diesel spray. In this Figure, images (a) and (b), (d) and (e), (g) and (h), (i) and (j) are paired, each pair captured from a single injection event with 1 μs delay between two consecutive frames.

The emergence of trapped air from previous injection events significantly alters the morphology of the spray. A ragged interfacial surface can be seen even at the very early stage of jet appearance. The tip of the jet leading edge is more oblique and the necking of the jet behind the umbrella in Figure III-2 is, in better agreement with experimental results in comparison with earlier numerical images [122]. The partial transparency of the experimental and numerical images can be seen leading to a more rapid disintegration. Despite the previous studies by the authors [109, 122, 125] where the influence of trapped air had been neglected, the production of small droplets commence at very early stages of the jet penetration.

Experimental and numerical penetration velocity of the jet at different axial distances from the nozzle exit and the corresponding Reynolds numbers are shown in Figure III-3. Experimental values are calculated by considering the displacement of the leading edge and the time-interval between two successive shots. The increase in the injection pressure in the sac, determined by the injection pressure ramp at the sac inlet, results in an overall rise in the penetration velocity and Reynolds number. The more realistic initial conditions at the start of simulation (inclusion of ingested air inside the nozzle liquid) leads to better agreement with the experimental data.

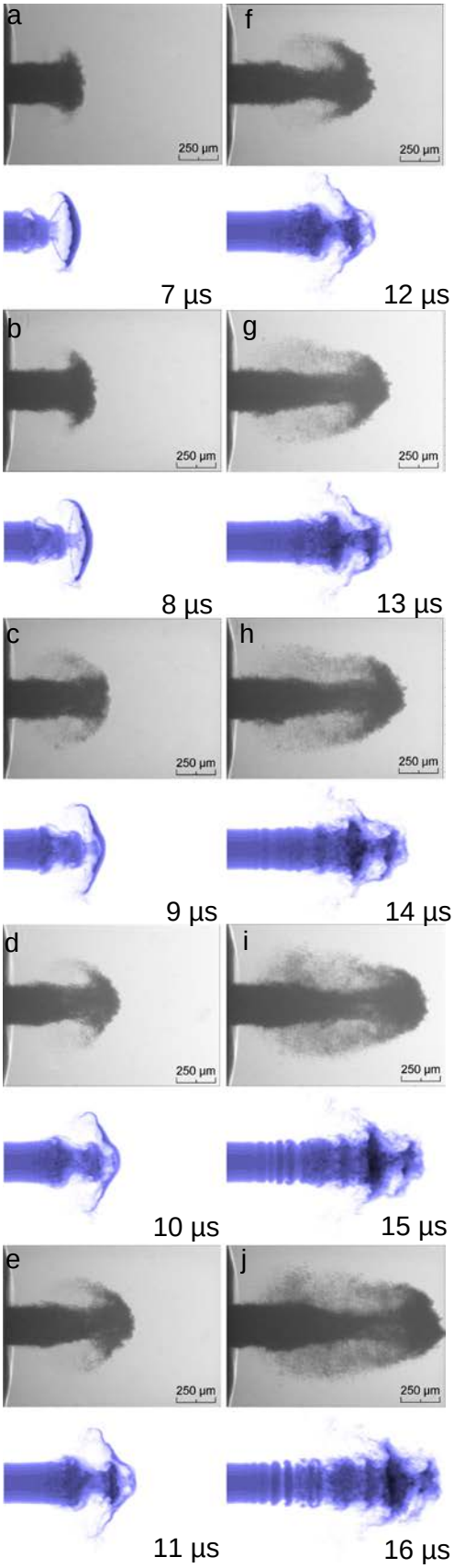

Figure III-2. Comparison of experimental images with CFD results. Images a and b, d and e, g and h, i and j are paired, each pair captured from the same injection event with 1 µs inter-frame time. Numerical results show the structure of the liquid at corresponding times ASOP.

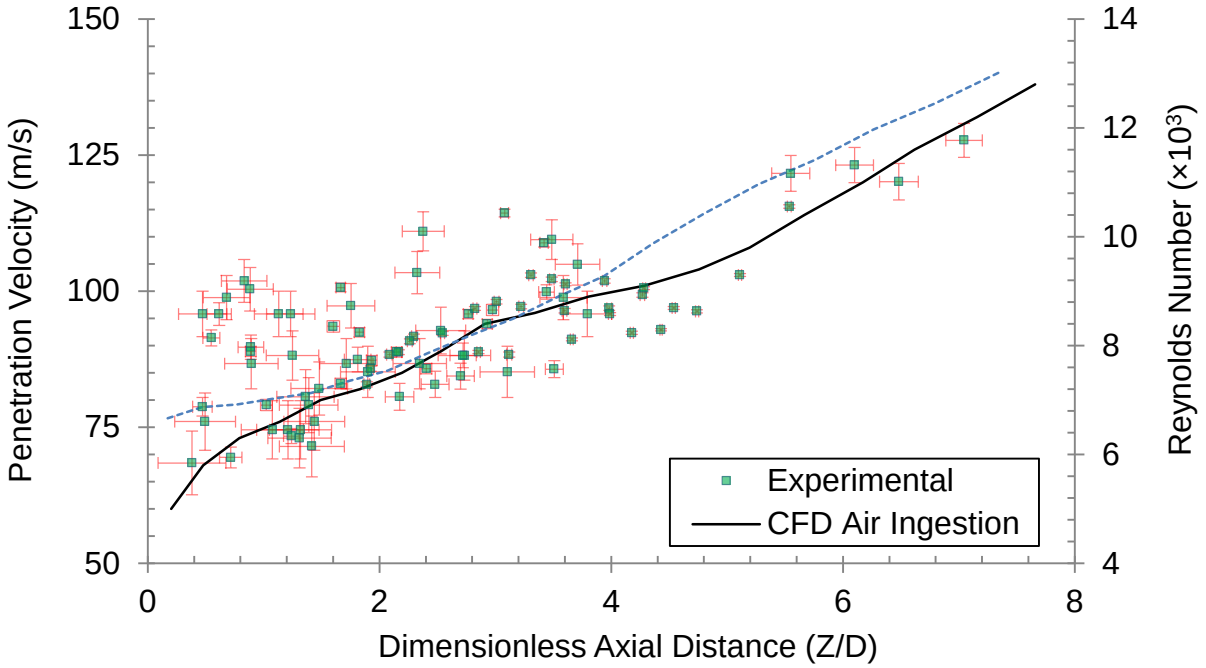

Figure III-3. Experimental and numerical values of penetration velocity of the leading edge at various axial distances from the nozzle exit. Inclusion of air in the initial conditions of simulation shows a better agreement compared with the just partially filled nozzle [122]. Reynolds number values are correlated using the computed penetration velocity of the leading edge.

III.4 Conclusions

The effect of ingested air, trapped from previous injection shots, on early stage of diesel spray dynamics is investigated experimentally and numerically employing microscopic backlit imaging and Eulerian/LES/VOF modelling respectively. The effects of trapped air on the growth and disintegration of surface structures on the emerging jet are characterized providing insight into the physics of primary atomisation. At the start of penetration, an umbrella-like leading edge and a semi-transparent cloud of air-fuel mixture at the leading edge are captured in both the numerical and experimental data. Comparison of measured penetration velocity of the jet between more than 100 consecutive shots and numerical results shows better correlation between experimental results and previous numerical results. The numerical results support the conclusion that air ingestion phenomena at the EOI significantly affect the spray structures and dynamics.

III.5 Acknowledgments

The authors acknowledge the support of the Australian Maritime College and the Defence Science and Technology Group.

[Page intentionally left blank]

Appendix IV:

CFD Results Using LimitedLinear Scheme

This appendix describes the morphology of penetrating jet using LimitedLinear convection scheme.

The effect of the Total Variation Diminishing (TVD) convection-specific interpolation scheme, LimitedLinear, on capturing the liquid-gas interface is illustrated qualitatively in Figure IV-1 and IV-2 for the fine grid resolution (20 million cells) using compressible-cavitating simulation. The TVD LimitedLinear scheme showed a ragged leading edge surface compared to the Normalised Variable (NV) Gamma scheme (Figure 3-9 and 3-10). Moreover, the LimitedLinear scheme does yield slightly more perturbed periphery of the liquid jet interfacial surfaces than the Gamma scheme. The ragged surface captured in experimental images is thought to be largely due to the air inclusion inside the nozzle. The rough interfacial surfaces have been captured in the simulation where air bubbles, trapped inside the nozzle liquid at the EOI process, were included. A detailed analysis of influence of the air inclusion on the morphology of jet at the SOI is provided in Appendix III.

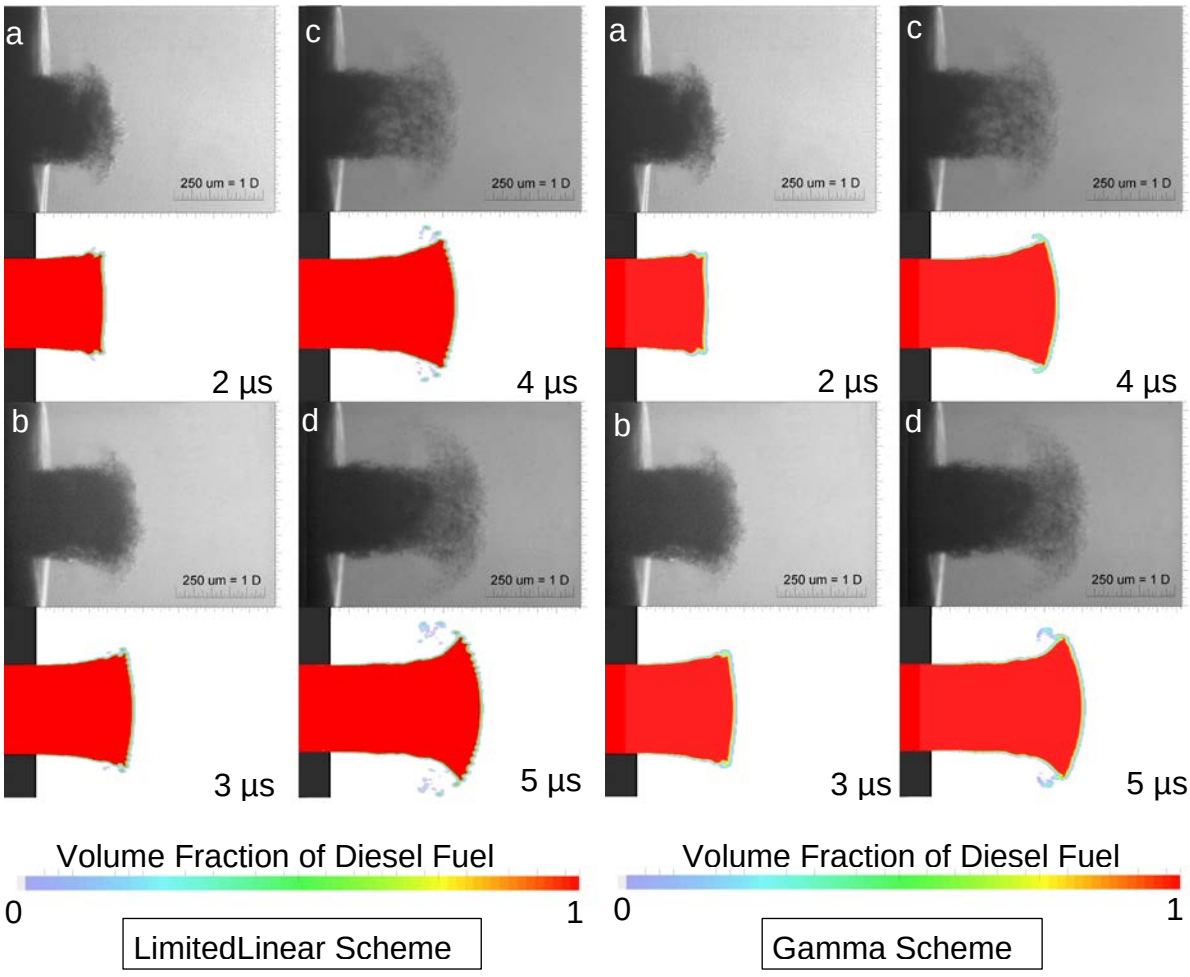

Figure IV-1. Comparison of experimental images with numerical results using LimitedLinear scheme for the fine mesh case with the highest magnification. Each column of the experimental image is from a different injection event captured from two consecutive frames with 1 µs inter-frame time.

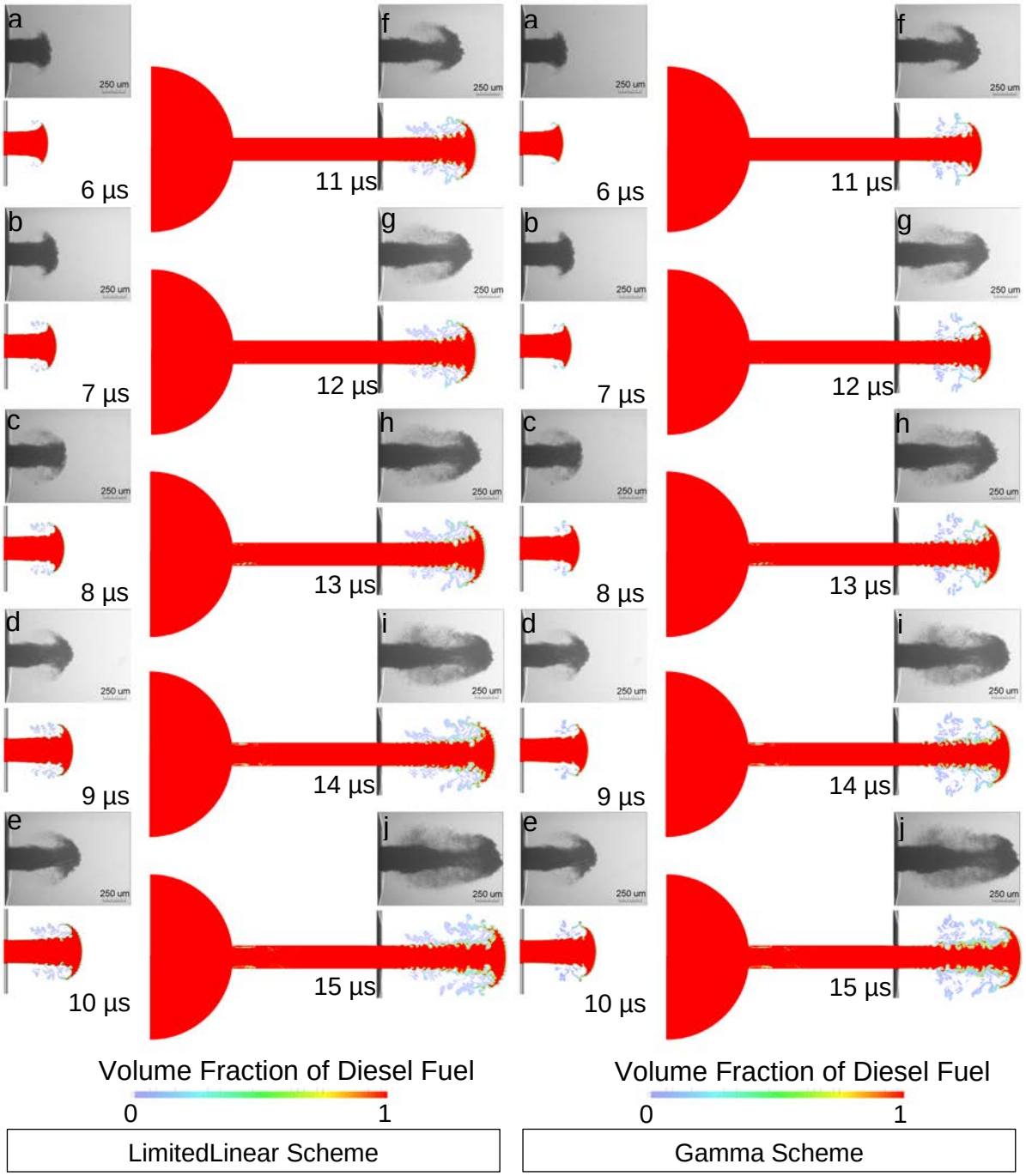

Figure IV-2. Comparison of experimental images with numerical results of LimitedLinear scheme extracted from the fine case for the SOP process. Images a and b, d and e, g and h, i and j are paired, each pair captured from the same injection event with 1 µs inter-frame time. Numerical results show the structure of the liquid jet coloured by γ at corresponding times ASOP.

References

[1] H. Großhans, Large Eddy Simulation of Atomizing Sprays, in, Lund University, 2013, pp. 115.

[2] C.H. Bong, Numerical and experimental analysis of diesel spray dynamics including the effects of fuel viscosity, in: Australian Maritime College, University of Tasmania, 2010.

[3] E. De Villiers, The potential of large eddy simulation for the modelling of wall bounded flows, 2006.

[4] V. Vuorinen, J. Yu, S. Tirunagari, O. Kaario, M. Larmi, C. Duwig, B.J. Boersma, Large-eddy simulation of highly underexpanded transient gas jets, Physics of Fluids (1994-present), 25 (2013) 016101.

[5] V. Vuorinen, M. Larmi, P. Schlatter, L. Fuchs, B.J. Boersma, A low-dissipative, scale-selective discretization scheme for the Navier–Stokes equations, Computers & Fluids, 70 (2012) 195-205.

[6] V. Vuorinen, H. Hillamo, O. Kaario, M. Larmi, L. Fuchs, Large Eddy Simulation of droplet stokes number effects on turbulent spray shape, Atomisation and Sprays, 20 (2010).

[7] R. Gjesing, J.H. Hattel, U. Fritsching, Coupled atomisation and spray modelling in the spray forming process using openfoam, Engineering Applications of Computational Fluid Mechanics, 3 (2009) 471-486.

[8] C. Baumgarten, Mixture formation in internal combustion engines, Springer, Germany, 2006.

[9] Z. Wang, H. Ding, X. Ma, H. Xu, M.L. Wyszynski, Ultra-high speed imaging study of the diesel spray close to the injector tip at the initial opening stage with split injection, Applied Energy, 163 (2016) 105-117.

[10] S. Moon, Y. Gao, S. Park, J. Wang, N. Kurimoto, Y. Nishijima, Effect of the number and position of nozzle holes on in-and near-nozzle dynamic characteristics of diesel injection, Fuel, 150 (2015) 112-122.

[11] W. Huang, Z. Wu, Y. Gao, L. Zhang, Effect of shock waves on the evolution of high-pressure fuel jets, Applied Energy, 159 (2015) 442-448.

[12] A.B. Swantek, D. Duke, F.Z. Tilocco, N. Sovis, C.F. Powell, A.L. Kastengren, End of Injection, Mass Expulsion Behaviours in Single Hole Diesel Fuel Injectors, in: ILASS Americas 26th Annual Conference on Liquid Atomisation and Spray Systems, Portland, OR, USA, 2014.

[13] S. Moon, Y. Gao, J. Wang, K. Fezzaa, T. Tsujimura, Near-field dynamics of high-speed diesel sprays: Effects of orifice inlet geometry and injection pressure, Fuel, 133 (2014) 299-309.

[14] Y. Wang, X. Liu, K.-S. Im, W.-K. Lee, J. Wang, K. Fezzaa, D.L. Hung, J.R. Winkelman, Ultrafast X-ray study of dense-liquid-jet flow dynamics using structure-tracking velocimetry, Nature Physics, 4 (2008) 305-309.

[15] M. Linne, M. Paciaroni, T. Hall, T. Parker, Ballistic imaging of the near field in a diesel spray, Experiments in fluids, 40 (2006) 836-846.

[16] E. Delacourt, B. Desmet, B. Besson, Characterisation of very high pressure diesel sprays using digital imaging techniques, Fuel, 84 (2005) 859-867.

[17] G. Bruneaux, Mixing process in high pressure diesel jets by normalized laser induced exciplex fluorescence Part I Free jet, SAE transactions, 114 (2005) 1444-1461.

[18] A.G. MacPhee, M.W. Tate, C.F. Powell, Y. Yue, M.J. Renzi, A. Ercan, S. Narayanan, E. Fontes, J. Walther, J. Schaller, S.M. Gruner, J. Wang, X-ray Imaging of Shock Waves Generated by High-Pressure Fuel Sprays, Science, 295 (2002) 1261-1263.

[19] G.M. Faeth, L.P. Hsiang, P.K. Wu, Structure and breakup properties of sprays, International Journal of Multiphase Flow, 21 (1995) 99-127.

[20] Z. Wu, Z. Zhu, Z. Huang, An experimental study on the spray structure of oxygenated fuel using laser-based visualization and particle image velocimetry, Fuel, 85 (2006) 1458-1464.

[21] M. Linne, Imaging in the optically dense regions of a spray: A review of developing techniques, Progress in Energy and Combustion Science, 39 (2013) 403-440.

[22] W. Eagle, M. Musculus, Cinema-stereo imaging of fuel dribble after the end of injection in an optical heavy-duty Diesel engine, in: Thiesel Conference Proceedings, 2014.

[23] M.P. Musculus, P.C. Miles, L.M. Pickett, Conceptual models for partially premixed low-temperature diesel combustion, Progress in Energy and Combustion Science, 39 (2013) 246-283.

[24] S. Som, A.I. Ramirez, D.E. Longman, S.K. Aggarwal, Effect of nozzle orifice geometry on spray, combustion, and emission characteristics under diesel engine conditions, Fuel, 90 (2011) 1267-1276.

[25] M. Gorokhovski, M. Herrmann, Modeling primary atomisation, Annu. Rev. Fluid Mech., 40 (2008) 343-366.

[26] J. Eggers, E. Villermaux, Physics of liquid jets, Reports on progress in physics, 71 (2008) 036601.

[27] M. Battistoni, Q. Xue, S. Som, Large-Eddy Simulation (LES) of Spray Transients: Start and End of Injection Phenomena, Oil & Gas Science and Technology–Revue d'IFP Energies nouvelles, 71 (2016) 4.

[28] M. Battistoni, C. Poggiani, S. Som, Prediction of the Nozzle Flow and Jet Characteristics at Start and End of Injection: Transient Behaviours, SAE International Journal of Engines, 9 (2015).

[29] M. Battistoni, Q. Xue, S. Som, E. Pomraning, Effect of Off-Axis Needle Motion on Internal Nozzle and Near Exit Flow in a Multi-Hole Diesel Injector, SAE International Journal of Fuels and Lubricants, 7 (2014) 167-182.

[30] M. Battistoni, A. Kastengren, C. Powell, S. Som, Fluid Dynamics Modeling of End-of-Injection Process, Proceedings of ILASS Americas, (2014).

[31] L.M. Pickett, J. Manin, R. Payri, M. Bardi, J. Gimeno, Transient rate of injection effects on spray development, in, SAE Technical Paper, 2013.

[32] K.-S. Im, S.-K. Cheong, C.F. Powell, M.-c.D. Lai, J. Wang, Unraveling the Geometry Dependence of In-Nozzle Cavitation in High-Pressure Injectors, Scientific Reports, 3 (2013) 2067.

[33] O. Kaario, V. Vuorinen, T. Hulkkonen, K. Keskinen, M. Nuutinen, M. Larmi, F.X. Tanner, Large Eddy Simulation of High Gas Density Effects in Fuel Sprays, Atomisation and Sprays, 23 (2013).

[34] T.R.C.M. Pringuey, Large eddy simulation of primary liquid-sheet breakup, in, University of Cambridge, 2012.

[35] G. Tomar, D. Fuster, S. Zaleski, S. Popinet, Multiscale simulations of primary atomisation, Computers & Fluids, 39 (2010) 1864-1874.

[36] X. Jiang, G.A. Siamas, K. Jagus, T.G. Karayiannis, Physical modelling and advanced simulations of gas–liquid two-phase jet flows in atomisation and sprays, Progress in Energy and Combustion Science, 36 (2010) 131-167.

[37] F. Salvador, J. Martínez-López, M. Caballer, C. De Alfonso, Study of the influence of the needle lift on the internal flow and cavitation phenomenon in diesel injector nozzles by CFD using RANS methods, Energy conversion and management, 66 (2013) 246-256.

[38] E. Giannadakis, M. Gavaises, C. Arcoumanis, Modelling of cavitation in diesel injector nozzles, Journal of Fluid Mechanics, 616 (2008) 153-193.

[39] A. Sou, S. Hosokawa, A. Tomiyama, Effects of cavitation in a nozzle on liquid jet atomisation, International Journal of Heat and Mass Transfer, 50 (2007) 3575-3582.

[40] M. Stahl, N. Damaschke, C. Tropea, Experimental investigation of turbulence and cavitation inside a pressure atomizer and optical characterization of the generated spray, in: Proceedings of international conference on liquid atomisation and spray systems, 10th ICLASS, Kyoto, Japan, Paper, 2006.

[41] C. Arcoumanis, H. Flora, M. Gavaises, M. Badami, Cavitation in real-size multi-hole diesel injector nozzles, SAE Trans., J. Engines, 109 (2000) 3.

[42] C. Badock, R. Wirth, A. Fath, A. Leipertz, Investigation of cavitation in real size diesel injection nozzles, International Journal of Heat and Fluid Flow, 20 (1999) 538-544.

[43] L. He, F. Ruiz, Effect of cavitation on flow and turbulence in plain orifices for high-speed atomisation, Atomisation and Sprays, 5 (1995).

[44] H. Chaves, M. Knapp, A. Kubitzek, F. Obermeier, T. Schneider, Experimental study of cavitation in the nozzle hole of diesel injectors using transparent nozzles, in, SAE technical paper, 1995.

[45] W. Nurick, Orifice cavitation and its effect on spray mixing, Journal of fluids engineering, 98 (1976) 681-687.

[46] H. Chaves, C.H. Ludwig, Characterization of cavitation in transparent nozzles depending on the nozzle geometry, in: Proc. Annu. Conf. Inst. Liq. Atom. Spray Syst., 18th (ILASS-2005), Orleans, France, 2005, pp. 259-264.

[47] J. Shinjo, A. Umemura, Detailed simulation of primary atomisation mechanisms in Diesel jet sprays (isolated identification of liquid jet tip effects), Proceedings of the Combustion Institute, 33 (2011) 2089-2097.

[48] M. Herrmann, On simulating primary atomisation using the refined level set grid method, Atomisation and Sprays, 21 (2011) 283-301.

[49] M. Stahl, M. Gnirß, N. Damaschke, C. Tropea, Laser Doppler measurements of nozzle flow and optical characterisation of the generated spray, in: ILASS, Orleans, France, 2005.

[50] P.K. Wu, G.M. Faeth, Aerodynamic effects on primary breakup of turbulent liquids, Atomisation and Sprays, 3 (1993).

[51] P.K. Wu, L.K. Tseng, G.M. Faeth, Primary breakup in gas/liquid mixing layers for turbulent liquids, Atomisation and Sprays, 2 (1992).

[52] R. Domann, Y. Hardalupas, Breakup model for accelerating liquid jets, in: Proceedings of 42nd AIAA Aerospace Science Meeting and Exhibition, 2004.

[53] K.A. Sallam, Z. Dai, G.M. Faeth, Liquid breakup at the surface of turbulent round liquid jets in still gases, International Journal of Multiphase Flow, 28 (2002) 427-449.

[54] C.M. Varga, J.C. Lasheras, E.J. Hopfinger, Initial breakup of a small-diameter liquid jet by a high-speed gas stream, Journal of Fluid Mechanics, 497 (2003) 405-434.

[55] R.D. Reitz, R. Diwakar, Structure of high-pressure fuel sprays, in, Fluid Mechanics Dept., GM Research Labs., Warren, MI, 1987.

[56] K. Huh, A. Gosman, A phenomenological model of diesel spray atomisation, in: Proceedings of the international conference on multiphase flows, 1991, pp. 515-518.

[57] F. Obermeier, H. Chaves, Study of pressure fluctuations flows, separation and cavitation in the nozzle and their influence on spray formation, in: Proc. of the 6th Workshop of the IDEA Project, 1992.

[58] C. Arcoumanis, M. Gavaises, B. French, Effect of fuel injection processes on the structure of diesel sprays, in, SAE Technical Paper, 1997.

[59] A. Nishimura, D. Assanis, A model for primary diesel fuel atomisation based on cavitation bubble collapse energy, in: Eight International Conference on Liquid Atomisation and Spray Systems, 2000.

[60] E.v. Berg, A. Alajbegovic, D. Greif, A. Poredos, R. Tatschl, E. Winklhofer, L. Ganippa, Primary break-up model for diesel jets based on locally resolved flow field in the injection hole, Zaragoza, 9 (2002) 11.

[61] C. Baumgarten, J. Stegemann, G. Merker, A new model for cavitation induced primary break-up of Diesel sprays, Zaragoza, 9 (2002) 11.

[62] T.B. Anderson, R. Jackson, Fluid mechanical description of fluidized beds. Equations of motion, Industrial & Engineering Chemistry Fundamentals, 6 (1967) 527-539.

[63] M. Ishii, Thermo-fluid dynamic theory of two-phase flow, NASA STI/Recon Technical Report A, 75 (1975) 29657.

[64] J. Shinjo, A. Umemura, Surface instability and primary atomisation characteristics of straight liquid jet sprays, International Journal of Multiphase Flow, 37 (2011) 1294-1304.

[65] S. Som, S. Aggarwal, Effects of primary breakup modeling on spray and combustion characteristics of compression ignition engines, Combustion and Flame, 157 (2010) 1179-1193.

[66] A. Burluka, R. Borghi, Development of a Eulerian model for the "atomisation" of a liquid jet, Atomisation and sprays, 11 (2001).

[67] T. Jin, K. Luo, Q. Dai, J. Fan, Direct numerical simulation on supersonic turbulent reacting and non-reacting spray jet in heated coflow, Fuel, 164 (2016) 267-276.

[68] J. Shinjo, A. Umemura, Simulation of liquid jet primary breakup: Dynamics of ligament and droplet formation, International Journal of Multiphase Flow, 36 (2010) 513-532.

[69] R.I. Issa, Solution of the implicitly discretised fluid flow equations by operator-splitting, Journal of Computational Physics, 62 (1986) 40-65.

[70] Y. Wang, L. Qiu, R.D. Reitz, R. Diwakar, Simulating cavitating liquid jets using a compressible and equilibrium two-phase flow solver, International Journal of Multiphase Flow, 63 (2014) 52-67.

[71] F. Coletti, M.J. Benson, A.L. Sagues, B.H. Miller, R. Fahrig, J.K. Eaton, Three-Dimensional Mass Fraction Distribution of a Spray Measured by X-Ray Computed Tomography, Journal of Engineering for Gas Turbines and Power, 136 (2014) 051508.

[72] E. De Villiers, A.D. Gosman, H.G. Weller, Large eddy simulation of primary diesel spray atomisation, SAE transactions, 113 (2004) 193-206.

[73] Y.J. Wang, K.S. Im, K. Fezzaa, W.K. Lee, J. Wang, P. Micheli, C. Laub, Quantitative x-ray phase-contrast imaging of air-assisted water sprays with high Weber numbers, Applied physics letters, 89 (2006) 151913.

[74] H. Hiroyasu, M. Arai, Structures of fuel sprays in diesel engines, in, SAE Technical Paper, 1990.

[75] L. Bravo, C. Ivey, D. Kim, S. Bose, High-fidelity simulation of atomisation in diesel engine sprays, in: Proceedings of the Summer Program, 2014, pp. 89.

[76] V. Vuorinen, H. Hillamo, O. Kaario, M. Nuutinen, M. Larmi, L. Fuchs, Effect of droplet size and atomisation on spray formation: A priori study using large-eddy simulation, Flow, turbulence and combustion, 86 (2011) 533-561.

[77] O. Desjardins, V. Moureau, H. Pitsch, An accurate conservative level set/ghost fluid method for simulating turbulent atomisation, Journal of Computational Physics, 227 (2008) 8395-8416.

[78] O. Desjardins, H. Pitsch, Detailed numerical investigation of turbulent atomisation of liquid jets, Atomisation and Sprays, 20 (2010).

[79] A. Yoshizawa, K. Horiuti, A statistically-derived subgrid-scale kinetic energy model for the large-eddy simulation of turbulent flows, Journal of the Physical Society of Japan, 54 (1985) 2834-2839.

[80] H.G. Weller, A new approach to VOF-based interface capturing methods for incompressible and compressible flow, OpenCFD Ltd., Report TR/HGW/04, (2008).

[81] B. Befrui, A. Aye, P. Spiekermann, D.L. Varble, M.A. Shost, M.C. Lai, J. Wang, GDi Skew-Angled Nozzle Flow and Near-Field Spray Analysis using Optical and X-Ray Imaging and VOF-LES Computational Fluid Dynamics, in, SAE Technical Paper, 2013.

[82] H. Jasak, Error analysis and estimation for the finite volume method with applications to fluid flows, (1996).

[83] N. Papadopoulos, P. Aleiferis, Numerical Modelling of the In-Nozzle Flow of a Diesel Injector with Moving Needle during and after the End of a Full Injection Event, SAE International Journal of Engines, 8 (2015) 2285-2302.

[84] L. Goldsworthy, C.H. Bong, P.A. Brandner, Measurements of diesel spray dynamics and the influence of fuel viscosity using PIV and shadowgraphy, Atomisation and Sprays, 21 (2011).

[85] H. Jasak, H.G. Weller, A.D. Gosman, High resolution NVD differencing scheme for arbitrarily unstructured meshes, International journal for numerical methods in fluids, 31 (1999) 431-449.

[86] D. Kim, O. Desjardins, M. Herrmann, P. Moin, Toward two-phase simulation of the primary breakup of a round liquid jet by a coaxial flow of gas, Centre for Turbulence Research Annual Research Briefs, 185 (2006).

[87] D. Kim, O. Desjardins, M. Herrmann, P. Moin, The primary breakup of a round liquid jet by a coaxial flow of gas, in: ILASS Americas 20th Annual Conference on Liquid Atomisation and Spray Systems, 2007.

[88] R. Payri, J.M. Garcia, F.J. Salvador, J. Gimeno, Using spray momentum flux measurements to understand the influence of diesel nozzle geometry on spray characteristics, Fuel, 84 (2005) 551-561.

[89] A. Fath, C. Fettes, A. Leipertz, Investigation of the Diesel Spray Break-Up Close to the nozzle at different Injection conditions, in: Fourth International Symposium on Diagnostics and Modeling of Combustion in Internal Combustion Engines, Kyoto, Japan, JSME, 1998, pp. 429-434.

[90] A. Leboissetier, S. Zaleski, Direct numerical simulation of the atomisation of a liquid jet, in: Proceeding of the ILASS-Europe, 2001, pp. 2-6.

[91] S.N. Soid, Z.A. Zainal, Spray and combustion characterization for internal combustion engines using optical measuring techniques – A review, Energy, 36 (2011) 724-741.

[92] B. Mohan, W. Yang, W. Yu, Effect of internal nozzle flow and thermo-physical properties on spray characteristics of methyl esters, Applied Energy, 129 (2014) 123-134.

[93] X. Wang, Z. Huang, W. Zhang, O.A. Kuti, K. Nishida, Effects of ultra-high injection pressure and micro-hole nozzle on flame structure and soot formation of impinging diesel spray, Applied Energy, 88 (2011) 1620-1628.

[94] A. Lefebvre, Atomisation and sprays, CRC press, 1988.

[95] R. Payri, J.P. Viera, V. Gopalakrishnan, P.G. Szymkowicz, The effect of nozzle geometry over internal flow and spray formation for three different fuels, Fuel, 183 (2016) 20-33.

[96] R. Payri, F. Salvador, J. Gimeno, O. Venegas, Study of cavitation phenomenon using different fuels in a transparent nozzle by hydraulic characterization and visualization, Experimental Thermal and Fluid Science, 44 (2013) 235-244.

[97] J.M. Desantes, R. Payri, A. Garcı́a, J. Manin, Experimental study of biodiesel blends' effects on diesel injection processes, Energy & Fuels, 23 (2009) 3227-3235.

[98] M. Battistoni, C. Grimaldi, F. Mariani, Coupled simulation of nozzle flow and spray formation using diesel and biodiesel for ci engine applications, in, SAE Technical Paper, 2012.

[99] T. Nakahira, M. Komori, M. Nishida, K. Tsujimura, The shock wave generation around the diesel fuel spray with high pressure injection, in, SAE Technical Paper, 1992.

[100] H. Hillamo, T. Sarjovaara, O. Kaario, V. Vuorinen, M. Larmi, Diesel spray visualization and shockwaves, Atomisation and Sprays, 20 (2010).

[101] M. Battistoni, C.N. Grimaldi, Numerical analysis of injector flow and spray characteristics from diesel injectors using fossil and biodiesel fuels, Applied Energy, 97 (2012) 656-666.

[102] J. Portillo, S. Collicott, G. Blaisdell, Measurements of axial instability waves in the near exit region of a high speed liquid jet, Physics of Fluids (1994-present), 23 (2011) 124105.

[103] L. Goldsworthy, N. Ashraf, P. Brandner, Development of a high pressure chamber for research into diesel spray dynamics, Australian Journal of Mechanical Engineering, 7 (2009) 15-34.

[104] J.U. Brackbill, D.B. Kothe, C. Zemach, A continuum method for modeling surface tension, Journal of Computational Physics, 100 (1992) 335-354.

[105] O. Ubbink, Numerical prediction of two fluid systems with sharp interfaces, in, University of London PhD Thesis, 1997.

[106] A. Schmid, B. Von Rotz, R. Schulz, K. Herrmann, G. Weisser, R. Bombach, Influence of nozzle hole eccentricity on spray morphology, in: ILASS 2013, 2013.

[107] F. Salvador, J. Martínez-López, J.-V. Romero, M.-D. Roselló, Study of the influence of the needle eccentricity on the internal flow in diesel injector nozzles by computational fluid dynamics calculations, International Journal of Computer Mathematics, 91 (2014) 24-31.

[108] R. Marcer, C. Audiffren, B. Yerly, Influence of the needle lift motion on cavitating flow inside Diesel injector, in: 12th Triennial International Conference on Liquid Atomisation and Spray Systems, ILASS Heidelberg, Germany, 2012, pp. 2-6.

[109] M. Ghiji, L. Goldsworthy, P.A. Brandner, V. Garaniya, P. Hield, Numerical and experimental investigation of early stage diesel sprays, Fuel, 175 (2016) 274–286.

[110] S. B. Pope, Turbulent Flows, Measurement Science and Technology, 12 (2001).

[111] R. Payri, F. Salvador, J. Gimeno, J. De la Morena, Macroscopic behaviour of diesel sprays in the near-nozzle field, in, SAE Technical Paper, 2008.

[112] J.V. Pastor, J.J. López, J.M. García, J.M. Pastor, A 1D model for the description of mixing-controlled inert diesel sprays, Fuel, 87 (2008) 2871-2885.

[113] R. Klein-Douwel, P. Frijters, L. Somers, W. De Boer, R. Baert, Macroscopic diesel fuel spray shadowgraphy using high speed digital imaging in a high pressure cell, Fuel, 86 (2007) 1994-2007.

[114] N. Dumont, O. Simonin, C. Habchi, Cavitating flow in diesel injectors and atomisation: a bibliographical review, in: 8th International Conference on Liquid Atomisation and Spray Systems, Pasedena, CA, 2000.

[115] J.M. Desantes, J. Pastor, A. Doudou, Study of the steady flow produced by direct injection diesel engine intake ports, Proceedings of the Institution of Mechanical Engineers, Part D: Journal of Automobile Engineering, 215 (2001) 285-298.

[116] J. Benajes, J. Pastor, R. Payri, A. Plazas, Analysis of the influence of diesel nozzle geometry in the injection rate characteristic, Journal of fluids engineering, 126 (2004) 63-71.

[117] H.W. Liepmann, A. Roshko, Elements of gasdynamics, Courier Corporation, 1957.

[118] J. Naber, D.L. Siebers, Effects of gas density and vapourization on penetration and dispersion of diesel sprays, in, SAE technical paper, 1996.

[119] J. Kim, H. Choi, Large eddy simulation of a circular jet: effect of inflow conditions on the near field, Journal of Fluid Mechanics, 620 (2009) 383-411.

[120] S.P. Lin, R.D. Reitz, Drop and Spray Formation from a Liquid Jet, Annual Review of Fluid Mechanics, 30 (1998) 85-105.

[121] C. Stanley, Experimental Investigation of Cavitation in a Cylindrical Orifice, in: School of Mechanical and Manufacturing Engineering, University of New South Wales, University of New South Wales, 2012.

[122] M. Ghiji, L. Goldsworthy, P.A. Brandner, V. Garaniya, P. Hield, Analysis of Diesel Spray Dynamics using a Compressible Eulerian/VOF/LES Model and Microscopic Shadowgraphy, Fuel, 188 (2017) 352-366.

[123] R. Yu, T.-W. Kuo, S. Shahed, T. Chang, The effect of mixing rate, end of injection, and sac volume on hydrocarbon emissions from a DI diesel engine, SAE transactions, 92 (1983) 3.843-843.857.

[124] M.P. Musculus, Entrainment waves in decelerating transient turbulent jets, Journal of Fluid Mechanics, 638 (2009) 117-140.

[125] M. Ghiji, L. Goldsworthy, V. Garaniya, P.A. Brandner, P. Hield, CFD Modelling of Primary Atomisation of Diesel Spray, in: 19th Australasian Fluid Mechanics Conference, 2014, pp. 1-4.

[126] T. Hayashi, M. Suzuki, M. Ikemoto, Effects of internal flow in a diesel nozzle on spray combustion, International Journal of Engine Research, (2013) 1468087413494910.

[127] A. Kastengren, C.F. Powell, F.Z. Tilocco, Z. Liu, S. Moon, X. Zhang, J. Gao, End-of-injection behaviour of diesel sprays measured with x-ray radiography, Journal of Engineering for Gas Turbines and Power, 134 (2012) 094501.

[128] D. Gueyffier, J. Li, A. Nadim, R. Scardovelli, S. Zaleski, Volume-of-fluid interface tracking with smoothed surface stress methods for three-dimensional flows, Journal of Computational physics, 152 (1999) 423-456.

[129] S. Osher, J.A. Sethian, Fronts propagating with curvature-dependent speed: algorithms based on Hamilton-Jacobi formulations, Journal of computational physics, 79 (1988) 12-49.

[130] H.G. Weller, G. Tabor, H. Jasak, C. Fureby, A tensorial approach to computational continuum mechanics using object-oriented techniques, Computers in physics, 12 (1998) 620-631.

[131] K.-S. Im, S.-K. Cheong, C.F. Powell, D.L. Ming-chia, J. Wang, Unraveling the Geometry Dependence of In-Nozzle Cavitation in High-Pressure Injectors, Scientific reports, 3 (2013).

[132] P.P. Bhat, S. Appathurai, M.T. Harris, M. Pasquali, G.H. McKinley, O.A. Basaran, Formation of beads-on-a-string structures during break-up of viscoelastic filaments, Nature Physics, 6 (2010) 625-631.

[133] R. Scardovelli, S. Zaleski, Direct numerical simulation of free-surface and interfacial flow, Annual Review of Fluid Mechanics, 31 (1999) 567-603.

[134] M. Arai, M. Tabata, H. Hiroyasu, M. Shimizu, Disintegrating process and spray characterization of fuel jet injected by a diesel nozzle, SAE Technical Paper, 840275, (1984) 12-05.